Physical Modeling of Abutment Scour for Overtopping, Submerged Orifice, and Free Surface Flows

Seung Ho Hong[1] and T. W. Sturm[2], M. ASCE

[1]Grad. Research Asst., School of Civil and Environmental Engineering, Georgia Institute of Technology, 790 Atlantic Dr, Atlanta, Georgia 30332; email: gtg002q@mail.gatech.edu
[2]Professor, School of Civil and Environmental Engineering, Georgia Institute of Technology, 790 Atlantic Dr, Atlanta, Georgia 30332; PH (404) 894-2218; email: tsturm@ce.gatech.edu

ABSTRACT

Recent flooding in the Atlanta metro area in Georgia, USA in September 2009 resulted in extensive damage to numerous bridges due to overtopping which caused abutment scour and failure of the approach embankment in some instances. At several locations, the 500–year flood level was exceeded. A laboratory study was conducted to compare characteristics of abutment scour for free–surface flow, submerged orifice flow and overtopping flow cases. Detailed bed scour contours under and downstream of the bridge as well as velocity distributions were measured for a model bridge with a set-back abutment in the floodplain of a compound channel. The channel bathymetry and bridge geometry were based on a typical bridge in the Piedmont region of Georgia. The embankment was constructed of an erodible core covered with rock riprap protection. Results showed that maximum abutment scour is a combination of local turbulence and flow contraction effects and has different magnitudes depending on the flow types (free–surface, submerged orifice, and overtopping) that produce unique flow fields through the bridge in the vicinity of the abutment.

INTRODUCTION

Failure of bridges due to bridge foundation scour during floods has been well documented (Parola et al. 1998, Richardson and Davis 2001, Morris and Pagan-Ortiz 1999). In many cases, the cause of failure has been classified as abutment scour although there is no clear agreement on its definition. In current scour prediction methodology as recommended by the report HEC-18 (Richardson and Davis 2001), abutment scour is treated as local scour near the abutment while contraction scour is considered to be scour that occurs across the entire cross-section, and the two estimates of maximum scour depth are added to obtain an estimate of total scour at the abutment. In contrast, laboratory studies by Sturm (1999, 2006), Ettema et al. (2006), and Ettema et al. (2008) on long abutments terminating on the floodplain of compound channels, for example, have predicted abutment scour depth as a multiplying factor times the idealized contraction scour depth as suggested by Laursen (1963), but all of these studies have focused on the case of free-surface flow. The latter studies by Ettema et al. are unique in that they include an erodible embankment instead of a fixed embankment that is more representative of a sheet–pile or riprap–protected abutment. Further confusing the issue of the definition of abutment scour is that extreme hydrologic events of the order of the 500–year or larger event can often result in submerged orifice flow, or embankment and bridge overtopping flow in combination with submerged orifice flow. Submergence of the upstream face of the bridge produces vertical flow contraction in addition to existing lateral flow contraction caused by the embankment on the floodplain. The result is a complex flow field in the vicinity of the abutment that results in a scour bathymetry having characteristics of vertical and lateral flow contraction in combination with local turbulence effects associated with the horseshoe vortex and a separated shear zone near the face of the abutment.

Occurrences of floods of extreme magnitude may seem to be so rare as to obviate the necessity of analysis but in 1994 (Tropical Storm Alberto) and again in 2009, such extreme floods occurred in Georgia resulting in widespread damage and closure of bridges as well as loss of life. A typical embankment failure due to bridge overtopping during flooding in September of 2009 is shown in Figure 1. This flood event resulted from precipitation in the Atlanta metro area that exceeded the 500–year recurrence interval (personal communication, Mark Landers, USGS). Flow coming from the left floodplain as well as overtopping of the bridge severely eroded the left embankment, exposed the abutment and resulted in the approach span to the bridge deck falling into the stream.

Figure 1. Example of abutment failure due to bridge overtopping

Given that embankment overtopping can and does occur, and may even be allowed to occur if the abutment structure itself is designed to withstand failure, this study is a preliminary consideration of the types of scour that are present in such instances. For this purpose, a model of a typical bridge in the Georgia Piedmont with an embankment terminating on the floodplain is used to investigate different modes of scour in free–surface, submerged orifice, and overtopping flows. Previously, this model was used to develop a laboratory modeling strategy for scour verified by comparisons with field measurements of scour during an historic flood associated with Tropical Storm Alberto (Hong and Sturm 2009).

EXPERIMENTAL INVESTIGATION

The bridge chosen to be modeled in this study is located near Macon, Georgia on the Towaliga River, which is a tributary of the Ocmulgee River. The bridge crosses between two bluffs with a solid rock outcropping forming the steep right bank just downstream of the bridge while a floodplain exists on the left side of the river. The drainage area of the river at the bridge is 816 km^2. Discharge was estimated as 1700 m^3/s by the U. S. Geological Survey for Tropical Storm Alberto (Stamey 1996). A model of the SR 42 bridge and the Towaliga River bathymetry was built in the Georgia Tech Hydraulics Laboratory at a scale of 1:60 as shown in Figure 2. Velocities and scour depths were measured in order to compare three types of flow: free–surface flow, submerged orifice flow and overtopping flow.

Figure 2. Laboratory model of Towaliga River bridge

The physical model of the Towaliga River Bridge was built inside a 4.2 m wide by 24.2 m long horizontal flume. The approach channel upstream of the bridge was 7.3 m long followed by a working mobile-bed section with a length of approximately 6.1 m in which the bridge model was placed. Templates were utilized to reproduce the channel bathymetry. The embankment model was constructed as an erodible fill with rock riprap protection in order to reproduce the influence of erosion of the end roll on the abutment and pier scour in the region of the toe of the embankment (Ettema et al. 2006). The erodible embankment was carefully compacted by hand and covered with riprap before putting the removable model roadway and bridge deck in place. This approach was successful in maintaining the general integrity of the embankment during overtopping as was observed in the prototype.

The water supply to the flume was provided from a large constant-head tank through a 30.5 cm diameter pipe that can deliver a maximum discharge of 0.3 m^3/s to the head box of the flume. In the supply pipe, discharge was measured by a magnetic flow meter with an uncertainty of ± 0.001 m^3/s. A flow diffuser, overflow weir, and baffles in the flume head box produced stilling of the inflow and a uniform flume inlet velocity distribution. A flap tailgate controlled the tailwater elevation.

Approach velocities were measured with a SonTek 16 MHz acoustic Doppler velocimeter (ADV) that was attached to an instrument carriage. A 3D down-looking probe was used to measure velocity profiles across the deeper portions of the cross section while a 2D side-looking probe was selected to measure velocity profiles in the shallow floodplain areas. The water depth and bed elevations before and after scouring were measured by a point gauge and the ADV with an uncertainty of ±1 mm. The sampling frequency of the ADV was chosen to be 25 Hz with a sampling duration of 2 minutes at each measuring location.

Each of the pier bents consists of two in-line rectangular columns having a width, *b*, of 0.91 m. Abutment or end bents were also modeled and buried in the erodible embankment which was protected by rock riprap. The bridge deck was made removable for scour measurements. The mobile bed sediment was a uniform sand with d_{50} = 0.53 mm. Further details on the experimental setup and the modeling methodology can be found in Lee et al. 2004, Hong et al. 2009, Lee and Sturm 2009.

EXPERIMENTAL PROGRAM

Experimental conditions for Runs 10–14 are summarized in Table 1. Preliminary HEC-RAS modeling indicated that the maximum velocity under the bridge in the left floodplain would occur at Q = 1275 m^3/s with subsequent increases in discharge contributing primarily to overtopping relief. On the other hand, submerged orifice flow was observed to occur first at Q = 1048 m^3/s as Q increased. Experimental Runs 10 and 14 were conducted at Q = 1048 m^3/s with the same tailwater elevation but with and without the bridge deck in place in order to compare submerged orifice flow and free surface flow. The discharge was increased to 1275 m^3/s in Run 11 to consider the case of initial overtopping with a shallow flow depth on the deck. In Run 14, discharge was increased to 1472 m^3/s for deeper overtopping and then compared with free surface flow at the same discharge in Run 13 by removing the deck. In each case, the tailwater appropriate to the given discharge was set to coincide with the field tailwater rating curve.

Table 1. Experimental conditions

(Q=discharge, V_{1m}= mean approach flow velocity in main channel, V_{cm}=critical velocity in main channel, V_{1f}= mean approach flow velocity in floodplain, V_{cf}=critical velocity in floodplain, $W.S._d$= water surface elevation downstream of bridge)

Run	Q (m^3/s)	V_{1m} (m/s)	V_{cm} (m/s)	$\frac{V_{1m}}{V_{cm}}$	V_{1f} (m/s)	V_{cf} (m/s)	$\frac{V_{1f}}{V_{cf}}$	$W.S._d$ (m)	Condition
10	1,048	0.98	2.44	0.402	0.75	2.26	0.333	134.29	Submerged orifice flow
14	1,048	0.98	2.44	0.402	0.75	2.26	0.333	134.29	Free flow
11	1,275	1.00	2.49	0.402	0.83	2.31	0.359	134.47	Overtopping flow
12	1,472	1.05	2.48	0.425	0.90	2.31	0.390	135.93	Overtopping flow
13	1,472	1.05	2.48	0.425	0.90	2.31	0.390	135.93	Free flow

EXPERIMENTAL RESULTS

The velocity distribution at the approach flow section is shown in Figure 3 for Run 10 in submerged orifice flow. The velocities are higher in the main channel than the floodplain as expected for an overbank flow, but the relative difference decreases as the discharge increases as observed in Table 1 by comparing V_{1m} and V_{1f}.

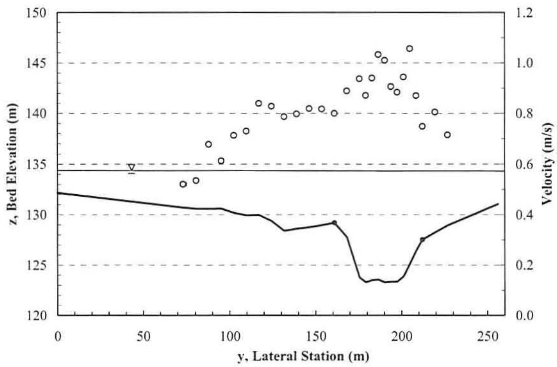

Figure 3. Measured velocity distribution in main channel and floodplain at bridge approach section for Run 10.

For each experimental condition, the scour experiments were run continuously for approximately five days to reach equilibrium. At the end of the scour experiment, the bed elevations were measured at six cross sections from the upstream to the downstream face of the bridge. The bed elevation data were adjusted to remove local pier scour (Hong et al. 2006), and the average floodplain elevation at each cross section was computed and plotted as a function of the streamwise coordinate through the bridge as shown in Figure 4. For both free–surface flow and submerged orifice flow with and without overtopping, the average floodplain contraction component of abutment scour increases with the streamwise coordinate through the bridge. The maximum value occurs near the second pier for free surface flow (Runs 13 and 14), while for submerged flows (Runs 10 and 12) it is located immediately downstream of the bridge, although a value similar to the maximum also occurs for overtopping flow at a distance of approximately 60 percent of the flow distance through the bridge. It is also clear from Figure 4 that submergence and overtopping add a significant increment of scour to the free–surface flow cases which include only the lateral contraction effect of the embankment. The largest mean floodplain scour depths through the bridge are observed for Run 12 at the maximum flow rate with overtopping.

The mean floodplain flow depth under the bridge after scour was obtained from a spatial integration of the bed profiles in Figure 4 relative to the water surface elevation. The mean depth values are given as Y_{2fc} in Table 2 and nondimensionalized in terms of the approach flow depth on the floodplain, Y_{1f}. The value of Y_{2fc} represents

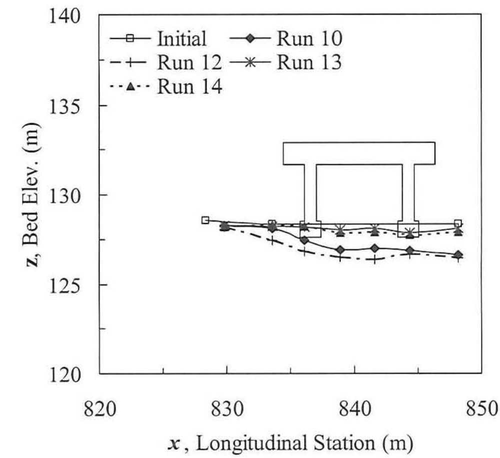

Figure 4. Mean floodplain bed elevations under the bridge after pier scour adjustment

a mean contraction/abutment scour depth on the floodplain caused by lateral flow contraction due to the floodplain flow being blocked by the embankment and forced through the bridge opening, and by vertical flow contraction in the case of submergence and overtopping. In addition to Y_{2fc}, the local maximum flow depth Y_{2fmax} was determined after removal of the local pier scour from the bed elevation data and is reported in Table 2. The excess of Y_{2fmax} relative to Y_{2fc} is the local scour contribution to abutment scour that can be attributed to the turbulence structures induced by flow separation including the horseshoe vortex and shear zone vortices around the nose of the abutment.

The dimensionless scour ratios Y_{2fc}/Y_{1f} and Y_{2fmax}/Y_{1f} from Table 2 are plotted in Figure 5 as a function of V_{1f}/V_{cf}, which is the ratio of the approach flow velocity in the floodplain to the critical velocity for sediment motion. For both the maximum and mean values of Y_2/Y_1 there is an increase in going from submerged orifice flow to a minor overtopping flow (Run 11) followed by a decrease at the larger overtopping depth and flow as V_{1f}/V_{cf} increases. The minor overtopping flow is insufficient to provide relief from the submerged orifice flow passing through the bridge so the scour increases, but as the proportion of the flow that is overtopping increases at the larger overtopping flow rate, there is a corresponding decrease in scour depth through the bridge. The maximum abutment scour ratio is approximately a constant of 1.2 times the contribution of the contraction scour ratio to abutment scour; that is

$$\frac{Y_{2f\max}}{Y_{1f}} \approx 1.2\frac{Y_{2fc}}{Y_{1f}} \tag{1}$$

Table 2. Experimental results for mean and maximum flow depths after scour (Q=discharge, V_{1f}=approach flow velocity in floodplain, V_{cf}=critical velocity in floodplain, Y_{1f}= approach flow depth in floodplain, Y_{2fc}= mean contraction flow depth under bridge after pier scour adjustment, $Y_{2f\max}$= flow depth at point of maximum abutment scour)

Run	Q (m^3/s)	$\frac{V_{1f}}{V_{cf}}$	Y_{1f} (m)	Y_{2fc} (m)	$Y_{2f\max}$ (m)	$\frac{Y_{2fc}}{Y_{1f}}$	$\frac{Y_{2f\max}}{Y_{1f}}$	Flow Condition
10	1,048	0.333	5.126	7.312	9.040	1.426	1.763	Submerged orifice flow
14	1,048	0.333	5.126	6.410	7.855	1.250	1.532	Free flow
11	1,275	0.359	5.906	9.894	12.116	1.675	2.052	Overtopping flow
12	1,472	0.390	5.946	9.339	11.083	1.571	1.864	Overtopping flow
13	1,472	0.390	5.946	7.861	9.153	1.322	1.539	Free flow

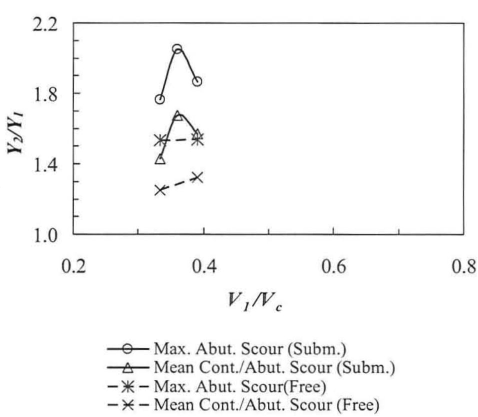

Figure 5. Maximum and mean relative flow depth ratios after scour for submerged and overtopping flow vs. free-surface flow

In other words, Eq. 1 states that the maximum abutment scour is a multiple of the mean flow–contraction contribution. Eq. 1 also holds for the maximum and mean depth ratios for the free–surface flow cases shown in Figure 5. The ratio of 1.2 in Eq. 1 is not necessarily expected to be a constant because this study considers only a fixed embankment length with a relatively small variation in the degree of flow contraction; rather, it is a confirmation that total abutment scour can be considered a multiple of contraction scour effects instead of an addition of local and contraction scour components that are incorrectly assumed to be independent. In this analysis, it is the actual contraction scour used as a reference value for abutment scour rather than the idealized long contraction scour. Finally, it can be observed in Figure 5 that a comparison of the mean depth ratios for submerged and overtopping flows with those for free–surface flows indicates a significant amount of additional scour caused by vertical flow contraction due to submergence and overtopping relative to lateral flow contraction in free–surface flow.

The location of the maximum abutment scour was found to be opposite the downstream edge of the abutment face between the first two pier bents starting from the embankment toe; that is, it was under the bridge deck. Its location was fairly consistent for all three types of flow considered in this study. Further research is continuing on this aspect of the problem.

CONCLUSIONS

A physical model study of inundation of a bridge embankment that terminates in the floodplain of a compound channel showed that lateral flow contraction, vertical flow contraction, and local turbulence effects all contribute to scour in the vicinity of the abutment. Scour at first increased in transitioning from submerged orifice flow to mild deck submergence but then decreased as the degree of submergence became more pronounced. This suggests that scour design procedures should include consideration of several overtopping cases in addition to submerged orifice flow. Using the procedures described in this paper, abutment scour is shown to be a combination of lateral and vertical flow contraction effects in addition to local scour influences and can be computed as a multiple of the contraction component of scour in the cases of submerged and overtopping flows as well as free–surface flows. Additional data are needed to confirm this relationship for a wider range of embankment lengths and flow contraction ratios.

ACKNOWLEDGMENTS
This research was partially supported by the Georgia Department of Transportation.

REFERENCES

Ettema, R., Yorozuya, A., Muste, M., and Nakato, T. (2006). "Design estimation of abutment scour depths." *Proceedings Third International Conference on Scour and Erosion*, CURNET, Gouda, The Netherlands.

Ettema, R., Nakato, T., Yorozuya, A., and Muste, M. (2008). "Three abutment scour conditions investigated with laboratory flume." *Proceedings Fourth International Conference on Scour and Erosion*, Chuo University, Tokyo, Japan.

Hong, S., Gotvald, A., Sturm, T. W., Landers, M. (2006). "Laboratory and field measurements of bridge contraction scour." *Proceedings Third International Conference on Scour and Erosion*, CURNET, Gouda, The Netherlands.

Laursen, E.M. (1963). "An analysis of relief bridge scour." *J. Hydr. Div.*, ASCE, 92(HY3), 93-118.

Lee, Seung Oh, Sturm, T. W., Gotvald, A., and Landers, M. (2004). "Comparison of laboratory and field measurements of bridge pier scour." *Proceedings Second International Conference on Scour and Erosion*, ed. by Y. M. Chiew, S. Y. Lim, and N. S. Cheng, Singapore, 231-239.

Lee, Seung Oh, and Sturm, T. W. (2009). "Effect of sediment size scaling on physical modeling of bridge pier scour." *J. Hydraul. Engrg.*, ASCE, 135(10), 793-802.

Morris, J.L., and Pagan-Ortiz, J.E. (1999). "Bridge scour evaluation program in the United States." *Stream Stability and Scour at Highway Bridges*, E.V. Richardson and P.F. Lagasse, eds., ASCE, 61-70.

Parola, A. C., Hagerty, D. J., and Kamojjala, S. (1998). *Highway infrastructure damage caused by the 1993 upper Mississippi River basin flooding*. NCHRP Report 417, Transportation Research Board, Washington, DC.

Richardson, E. V., and Davis, S. R. (2001). *Evaluating scour at bridges.* HEC-18, U.S. Federal Highway Administration, Washington, DC.

Stamey, Timothy C. (1996). *Summary of data-collection activities and effects of flooding from Tropical Storm Alberto in parts of Georgia, Alabama, and Florida, July 1994.* U.S. Geological Survey Open-File Report 96-228, 23p.

Sturm, T.W. (1999). "Abutment scour studies for compound channels." Report *FHWA-RD-99-156*, U.S. Dept. of Transportation, Federal Highway Administration, Washington, D.C.

Sturm, Terry W. (2006). "Scour Around Bankline and Setback Abutments in Compound Channels," *J. Hydraul. Engrg.*, ASCE, 132(1), 2006, 21-32.

Experimental Investigation of Critical Hydraulic Gradients for Unstable Soils

M.F. Ahlinhan[1], M.Sc. and M. Achmus[1], Prof. Dr.-Ing.

[1] Leibniz University of Hannover, Institute of Soil Mechanics, Foundation Engineering and Waterpower Engineering, Appelstr. 9A, D-30167 Hannover, Germany; email: ahlinhan@igbe.uni-hannover.de / achmus@igbe.uni-hannover.de

ABSTRACT

The presence of unstable soils, i.e. soils in which suffusion can arise, is a potential risk to structures under which seepage occurs. It is therefore necessary to clearly identify unstable soils and to estimate hydraulic gradients at which erosion may start. An experimental study was carried out to quantify critical hydraulic gradients of unstable soils with respect to vertical upward and horizontal flow. It was found that critical gradients for unstable soils lie in the range of 0.2 both for vertical and horizontal flow, with a small dependence on the relative density. For nearly stable soils a strong effect of the relative density on the critical hydraulic gradients was found. Also, the "more stable" a soil is, the greater the difference of critical gradients for vertical and horizontal flow. The obtained results are compared to the results of other researchers.

INTRODUCTION

In the risk assessment of potential damage to dams or barrages the consideration of erosion processes in connection with under-seepage of such structures is of great significance. This is particularly valid if the subsoil consists of unstable soils. These are non-cohesive soils with a large uniformity index (non-uniform soils with uniformity index C_u >5 to 10) or irregular grain size distributions. In such soils erosion, i.e. transport of soil grains, starts at much lower hydraulic gradients than in soils with regular grain size distribution. The result of the erosion process is the wash-out of the fine-grained portion of the soil (suffusion). It has not been clear how important the effect of the soil gradation on the critical gradients in vertical and horizontal direction is and how it depends on the soil composition and its relative density. Special testing devices were therefore designed to investigate the erosion phenomenon dependent on the above mentioned factors.

OVERVIEW OF THE STATE OF THE ART

To assess whether suffusion is possible, in general the composition of the soil and the geometry of the pore channels have to be considered. Suffusion is only possible if the grains of the fine soil can pass through the pores of the coarse soil matrix. Since the pore channel geometry cannot be exactly measured, the assessment is based on the grain size distribution only. If the "geometric" criterion yields the result that suffusion is possible, i.e. the soil is potentially unstable, the minimum hydraulic gradient necessary to cause erosion and to transport the fine soil grains has to be assessed by a "hydraulic" criterion.

Geometric criteria

Suffusion is the transport and wash-out of the fine grains of a soil through the grain skeleton formed by the coarse parts: it can be considered as a contact erosion process (i.e. the wash-out of a fine soil through the pores of an adjacent coarse soil layer) between the fine and coarse parts of the soil. Based on this consideration, Kezdi (1979) proposed splitting up the grain size distribution of a soil into two distributions of the fine and coarse parts, and assessing the stability by Terzaghi's well-known contact erosion criterion applied to the two distributions. This criterion, also known as Terzaghi's filter rule, is formulated as follows:

$$d_{c,15} \leq 4\, d_{f,85} \qquad (1)$$

with $d_{c,15}$ = grain diameter for which 15% of the grains by weight of the coarse soil are smaller and $d_{f,85}$ = grain diameter for which 85% of the grains by weight of the fine soil are smaller.

The Terzaghi criterion is valid only for poorly graded soil. To avoid this limitation, in the German guideline BAW (1989) the splitting method is recommended in combination with the Cistin/Ziems contact erosion criterion (see e.g. in Semar & Witt 2006), which is also applicable to non-uniform soils. In general, the grain size distribution has to be split up at several points and the resulting fine and coarse soils have to be assessed with the contact erosion criterion.

Kenney and Lau (1985) proposed transforming the ordinary grain size distribution curve to a F-H diagram. Here F is the mass percentage of grains with diameters less than a particular diameter d and H is the mass percentage of grains with diameters between d and 4d (Fig. 1). In the first version $H/F \geq 1.3$ was proposed as stability criterion. In a following publication (Kenney and Lau 1986), the less conservative requirement $H/F \geq 1.0$ was recommended for use.

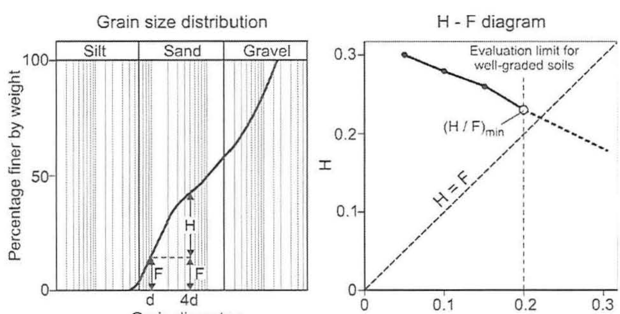

Figure 1. Geometrical suffusion criterion after Kenney and Lau (1985).

In principle, both the Kezdi and the Kenney & Lau criteria require a minimum inclination of the grain size distribution curve. Chapuis (1992) stated that the Kezdi criterion means that "the slope of the grain-size distribution is flatter than 15% per four times change in grain size", i.e. $H \leq 0.15$ for all F values. In contrast, for the Kenney & Lau criterion the required minimum inclination is dependent on F. Both criteria are depicted in Fig. 2 and the test results of several authors regarding the internal stability of soils are presented. Fig. 2 shows that all soils with points lying above the Kenney & Lau line are stable and all soils with points lying below the Kezdi line are unstable. Soils with points lying in the "transition zone" (H > F < 0.15 and 0.15 < H < F) can obviously be either stable or unstable. Li & Fannin (2008) proposed using the Kenney & Lau criterion for well-graded soils and the Kezdi criterion for a gap-graded soil.

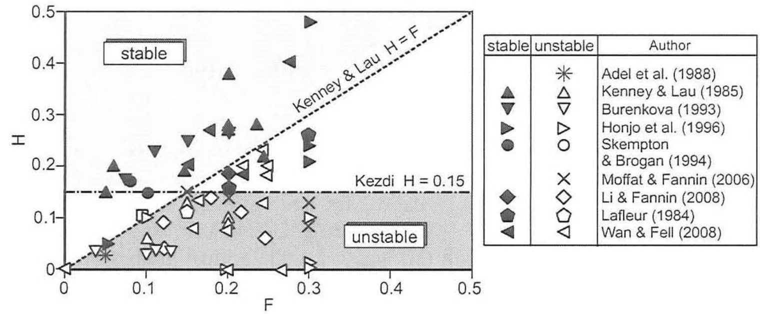

Figure 2. Compilation of test results and comparison with criteria of Kezdi and of Kenney & Lau.

For the application of the Kezdi criterion the grain size distribution has to be split up at several points and the resulting grain size distribution have to be checked with respect to contact erosion criteria. Usually the most unfavourable combination of fine and coarse soil results when the split-off point lies in the region of a small inclination of the grain size distribution. Thus, in a simplified application, the split can be done only at the point where H/F becomes a minimum ($(H/F)_{min}$). The ratio of $d_{c,15}$ and $d_{f,85}$ found for the curve splitting at that point is denoted in the following as $(d_{c,15}/d_{f,85})_{mod}$. With respect to Eq. (1), this value has to be less than 4 to indicate internal stability of the soil considered.

Hydraulic criteria

For an upward seepage flow through a stable soil without surface load the critical hydraulic gradient can be derived as follows (e.g. Terzaghi and Peck 1961):

$$i_{v,crit} = \frac{\gamma'}{\gamma_w} \qquad (2)$$

Here γ' and γ_w are the soil's buoyant unit weight and the unit weight of water, respectively.

Istomina (1957) – cited in Busch et al. (1993) – carried out tests with various soils under vertical upward flow and proposed estimating the critical hydraulic gradient dependent on the uniformity index of the soil (Fig. 3).

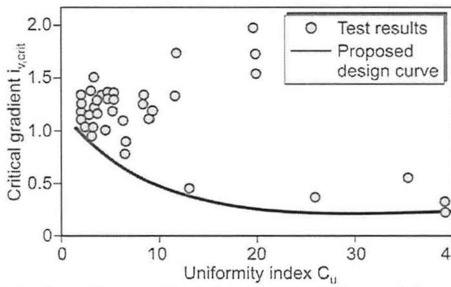

Figure 3. Critical hydraulic gradient for upward flow with respect to suffusion after Istomina (Busch et al. 1993).

Adel et al. (1988) carried out tests with stable and unstable soils (with regard to the Kenney & Lau criterion) under horizontal seepage flow. They determined critical hydraulic gradients of $i_{h,crit}$ = ca. 0.2 for three unstable soils with $(H/F)_{min} <$ 0.5. For two soils with $(H/F)_{min} = 1.3$ the critical gradients were between 0.6 and 0.7 and for a definitely stable soil with $(H/F)_{min} = 1.8$ the critical gradient was ca. 1.0. The results are depicted in Fig. 4.

Skempton and Brogan (1994) carried out tests with upward flow to determine the critical hydraulic gradients for unstable soils. They found that the values can be only one third to one fifth of the theoretical value according to Eq. (2). They presented the results for both vertical upward and horizontal flow (determined by Adel et al. 1988, see above) dependent on the $(H/F)_{min}$-value of the soil and suggested the connection shown in Fig. 4. Obviously, for unstable soils the difference between the vertical and the horizontal critical hydraulic gradient is rather small.

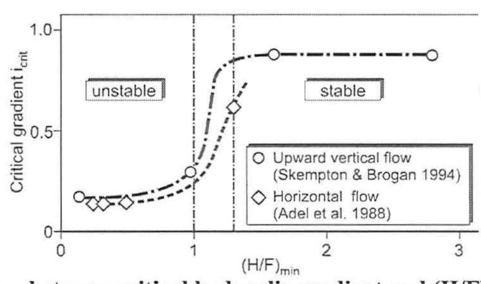

Figure 4. Relation between critical hydraulic gradient and $(H/F)_{min}$ proposed by Skempton and Brogan (1994).

Wan and Fell (2008) investigated 14 clay-silt-sand-gravel and silt-sand-gravel mixtures and found critical gradients for unstable soils less than 0.5. They also found that tendentially smaller values apply to soils in a loose state than to soils in a dense state.

Moffat and Fannin (2006) investigated the effect of vertical load acting on the sample's surface for unstable soils. They found that the critical gradients increased with an increase of the surface load.

EXPERIMENTS

Five different non-cohesive soils were tested in specially developed test devices under upward and horizontal seepage flow. The hydraulic gradient was increased slowly and gradually in order to identify the critical gradient at which erosion begins. The initial relative density of the soils was varied in the tests.

The grain size distributions of the five soils are shown in Fig. 5 and the relevant soil parameters are given in Table 1. The soils A1 and A2 are fine to medium and medium to coarse sands, respectively, which are poorly graded and stable with respect to all geometric criteria (Kenney & Lau parameter $(H/F)_{min} = 4.4$ and 5.93, respectively). The soils E1, E2 and E3 are gap-graded soils, which were produced artificially. E2 and E3 are clearly unstable soils, whereas E1 has an $(H/F)_{min}$ value of 1.1 and lies on the border between the stable and unstable region with regard to the Kenney & Lau criterion. Applying the Kezdi criterion with $(d_{c,15}/d_{f,85})_{mod} < 4$ also leads to a close decision regarding internal stability.

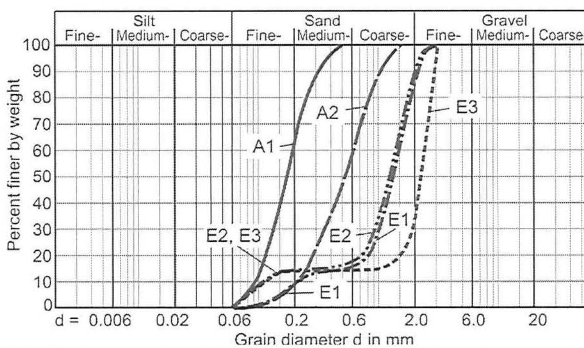

Figure 5. Grain size distributions of the soils used in the experiments.

Table 1. Properties of the soils used in the experiments

Property	Soil				
	A1	A2	E1	E2	E3
Density of grains ρ_s [t/m^3]	2.65	2.65	2.65	2.65	2.65
Minimum porosity n_{min}	0.40	0.32	0.34	0.27	0.31
Maximum porosity n_{max}	0.52	0.43	0.42	0.40	0.42
Uniformity index C_u	2.1	3.0	7.0	13.9	23.4
Index of Curvature C_c	1.0	1.0	3.3	6.7	13.8
$(H/F)_{min}$	5.93	4.44	1.10	0.20	0.03
$(d_{c,15}/d_{f,85})_{mod}$	1.31	1.50	3.30	7.20	14.40

Experiments with upward flow

A photographic view and a schematic drawing of the test device for vertical upward flow are shown in Fig. 6. The soil sample with a diameter of 28.5cm and a height of 30cm was subjected to a gradually increased vertical hydraulic gradient. During the test, the water discharge and the water pressures along the sample's height were recorded almost continuously.

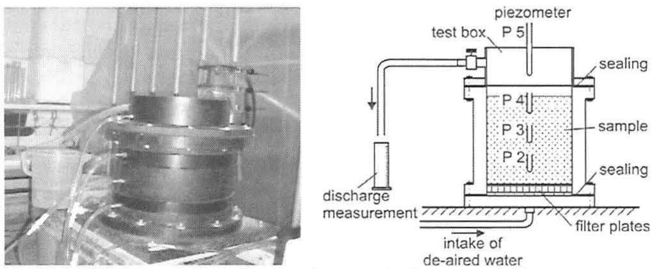

Figure 6. Test device for vertical upward flow.

The placement of the sample was carried out by pluviation under water. To prevent entrapped air falsifying the test results, the water was de-aired by boiling and cooled down to the test temperature of 20°C. A soil mass chosen with respect to the desired relative density was pluviated into the test box and compaction was then carried out by vibrating the box until the desired sample level was reached.

The determination of the critical hydraulic gradient was done by noting the water discharge and the filter velocity of the water flow, respectively. An example is shown in Fig. 7. For the internally stable soil (Fig. 7 left) the onset of erosion is connected with an immediate increase in the flow velocity and thus the permeability. Some grain movements on the sample surface already occur at smaller hydraulic gradients, but this does not lead to erosion. For the unstable soil (Fig. 7 right) the change in the permeability is more continuous. From a certain hydraulic gradient on, a strongly increased mass transport and a significant increase of the flow velocity was observed. At this state, the critical gradient was determined.

Experiments with horizontal flow

In order to grasp the directional dependence of the critical hydraulic gradients, tests with horizontal seepage flow were also carried out. A photographic view and a schematic drawing of the test device used are shown in Fig. 8. The sample had a cross section of 10cm x 30cm and was seeped horizontally on a sample length of 60cm. The placement of the material was again done by pluviation in de-aired water with the test box standing in a 90° rotated position. The sieve fabrics located at both ends of the sample were so chosen that a transport of the fine soil parts was possible.

The hydraulic gradients were increased slowly and gradually and the water discharge and the mass of eroded fines were observed almost continuously. In both curves a significant change was observed at a particular hydraulic gradient, i.e. a significant change in the permeability and an increase in the transported soil mass. At this point the critical hydraulic gradient was recorded.

TEST RESULTS

Vertical upward flow

The experimentally determined hydraulic gradients for upward flow are given in Fig. 9, dependent on the initial relative density of the soil samples.

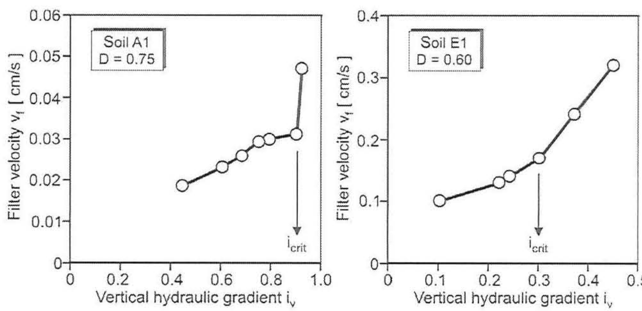

Figure 7. Development of filter velocity with the hydraulic gradient.

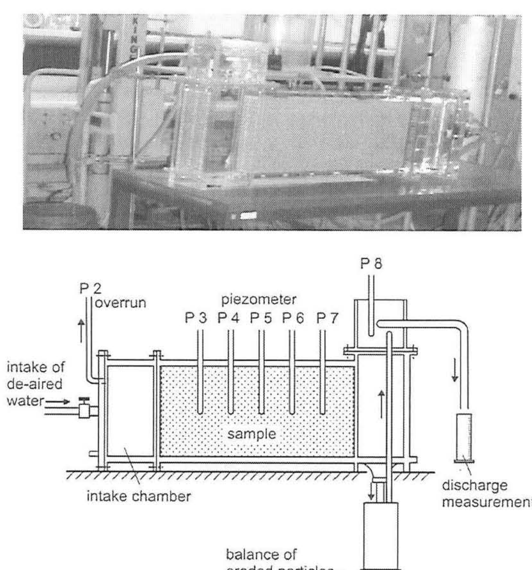

Figure 8. Test device for horizontal flow.

For the stable soils A1 and A2 the obtained critical gradients agree quite well with the theoretical values according to Eq. (2). In fact, slightly lower values were found with a maximum deviation of about 10%, which might be a result of unavoidable heterogeneities of the samples.

For the clearly unstable soils E2 and E3 very small critical gradients between 0.18 and 0.23 were measured. There is only a small dependence on the relative density of the sample. On the contrary, for soil E1, which is on the border between stable and unstable, a clear dependence of the critical hydraulic gradient on the relative densities was found. For a very dense state the critical hydraulic gradient is about double the value determined for a medium dense state. However, the value for very dense state is also significantly smaller than the theoretical critical hydraulic gradient from Eq. (2). Thus, soil E1 has to be classified as potentially unstable.

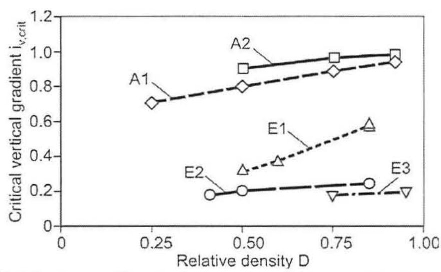

Figure 9. Critical gradients determined for vertical upward flow.

Fig. 10 shows the critical hydraulic gradients determined for the unstable soils dependent once on $(H/F)_{min}$ and once on $(d_{c,15}/d_{f,85})_{mod}$. The values obtained by Skempton and Brogan (1994) for dense sand are also depicted. The dependence on $(H/F)_{min}$ suggested by Skempton and Brogan is confirmed, with the exception of the nearly stable soil E1, where the critical gradient is very much dependent on the initial relative density. There is also a connection of the critical hydraulic gradients with the parameter $(d_{c,15}/d_{f,85})_{mod}$, but the scatter here is slightly larger. The trend lines in Fig. 11 right are suggested curves regarding the effect of relative density. Evidently, the "more stable" a soil is, the more important the relative density.

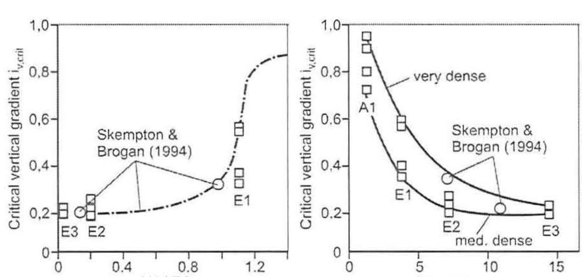

Figure 10. Critical gradients dependent on instability parameters.

Horizontal flow

In Fig. 11 the experimentally determined critical hydraulic gradients with regard to horizontal flow are presented dependent on the parameter $(d_{c,15}/d_{f,85})_{mod}$. The critical gradients for vertical flow are also given.

Tendentially, the critical gradient for horizontal flow is slightly smaller than the one for upward flow. However, the "more unstable" a soil is, the smaller the difference, and thus the smaller the critical vertical gradient. For the unstable soils E2 and E3 even slightly higher horizontal than vertical critical gradients were obtained for dense and very dense initial states. In that respect it has to be considered that in the case of vertical flow the sample surface was free and thus a certain loosening of the sample was possible due to the seepage forces acting, which of course favours internal erosion. This might also be the reason for the stronger dependence of horizontal critical gradients on the sample's relative density.

The results of Adel et al. (1988) with critical horizontal gradients of around 0.2 for unstable soils are confirmed by the tests. Unfortunately, Adel et al. did not document the relative density of the soil in their tests.

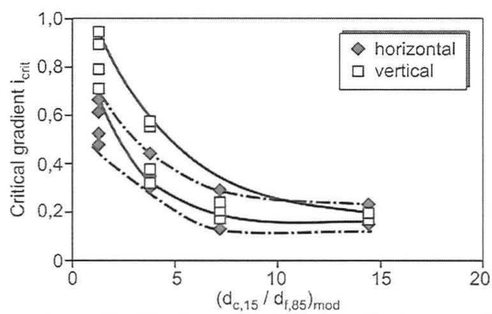

Figure 11. Comparison of critical gradients for vertical upward and horizontal flow.

CONCLUSIONS

The tests reported here show that for clearly unstable sands, i.e. with $(H/F)_{min}$-values significantly smaller than 1.0, the critical hydraulic gradients for upward flow lie at around 0.2 with only a slight dependence on the initial relative density. Also, the critical gradients for horizontal flow are nearly the same as those for vertical flow.

For clearly stable soils, e.g. poorly graded sands, the critical gradients for horizontal flow are significantly smaller than the critical gradients for vertical flow.

Sands which lie on the border between stable and unstable soils behave in a special way. For such a soil a distinct dependence of critical hydraulic gradients on the relative density was found. It can be concluded that the decision whether such a soil is stable or potentially unstable requires consideration of the compaction state.

ACKNOWLEDGEMENT

This research was partially supported by the Germany Ministry of Education and Research through IPSWaT (International Postgraduate Studies in Water Technologies). This support is gratefully acknowledged.

REFERENCES

Adel, H. den, Bakker, K.J. and Breteler, M.K. (1988): "Internal stability of minestone". *Proc. Int. Symp. Modelling Soil-Water-Structure Interaction*, pp.225-231. Rotterdam, Balkema.

BAW (1989): Bundesanstalt für Wasserbau – Merkblatt Anwendung von Kornfiltern an Wasserstraßen (MAK), Ausgabe 1989 (in German).

Burenkova, V.V. (1993): "Assessment of suffusion in non-cohesive and graded soils", *Filters in Geotechnical and Hydraulic Engineering*, ed. Brauns, Heibaum & Schuler, pp. 357-360.

Busch, K.-F., Luckner, L. and Tiemer, K. (1993): Geohydraulik: Lehrbuch der Hydrologie, 3rd ed., Gebrüder Borntraeger, Berlin / Stuttgart (in German).

Chapuis, R.P. (1992): "Similarity of internal stability criteria for granular soils", *Canadian Geotechnical Journal*, Vol. 29, pp. 711–713.

Honjo, Y., Haque, M.A., Tsai, K.A. (1996): "Self-filtration behavior of broadly and gap graded cohesionless soils". *Geofilters'96*, Montreal/Canada.

Kenney, T.C. and Lau, D. (1985): "Internal stability of granular filters", *Canadian Geotechnical Journal*, Vol. 22, pp. 215–225.

Kenney, T.C. and Lau, D. (1986): "Internal stability of granular filters: Reply", *Canadian Geotechnical Journal*, Vol. 23, pp. 420-423.

Kezdi, A. (1979): Soil physics. Elsevier Scientific Publishing Company, Amsterdam.

Lafleur, J. (1984): "Filter testing of broadly graded cohesionless tills", *Canadian Geotechnical Journal*, Vol. 21, pp. 634-643.

Li, M. and Fannin, R.J. (2008): "Comparison of two criteria for internal stability of granular soil", *Canadian Geotechnical Journal*, Vol. 45, pp. 1303–1309.

Moffat, R.A. and Fannin, R.J. (2006): "A large permeameter for study of internal stability in cohesionless soils", *Geotechnical Testing Journal*, Vol. 29. No.4, pp. 273-279.

Semar, O. and Witt, K.J. (2006): "Internal erosion – State of the art and an approach with percolation theory", 3rd *International Conference on Scour and Erosion, Amsterdam, the Netherlands.*

Skempton, W. and Brogan, J.M. (1994): "Experiments on piping in sandy gravels", *Géotechnique* No. 3, pp. 449–460.

Terzaghi, K., Peck, R.B. (1961): Die Bodenmechanik in der Baupraxis, Springer Verlag, Berlin, 1961 (in German).

Wan, C.F. and Fell, R. (2008): "Assessing the potential of internal instability and suffusion in embankment dams and their foundations", *Journal of Geotechnical and Geoenvironmental Engineering*, Vol. 134, No. 3, pp. 401-407.

Flow Velocities and Bed Shear Stresses in a Stone Cover under an Oscillatory Flow

F. Stevanato[1], A. W. Nielsen[2], B. M. Sumer[3] and J. FredsØe[4]

[1] Technical University of Denmark, DTU Mekanik, Section of Coastal, Maritime and Structural Engineering, Building 403, 2800 Kgs. Lyngby, Denmark; e-mail: Francesco.stevanato09@imperial.ac.uk. Present address: Imperial College London, Department of Civil and Environmental Engineering, London SW7 2AZ, UK

[2] Technical University of Denmark, DTU Mekanik, Section of Coastal, Maritime and Structural Engineering, Building 403, 2800 Kgs. Lyngby, Denmark; e-mail: awni@mek.dtu.dk

[3] Technical University of Denmark, DTU Mekanik, Section of Coastal, Maritime and Structural Engineering, Building 403, 2800 Kgs. Lyngby, Denmark; e-mail: bms@mek.dtu.dk

[4] Technical University of Denmark, DTU Mekanik, Section of Coastal, Maritime and Structural Engineering, Building 403, 2800 Kgs. Lyngby, Denmark; e-mail: jf@mek.dtu.dk

ABSTRACT

In order to get a better understanding of the interaction between the wave-induced, near-bed oscillatory flow, the stone cover and the sea bed, physical model tests were carried out. The tests were conducted in an oscillating water tunnel. The bottom of the tunnel was covered by one, two and three layers of stones. The flow velocities in the pores of the stones were measured using LDA (Laser Doppler Anemometer). In addition to the velocity measurements, the bed shear stresses were also measured using a hotfilm (Constant Temperature Anemometry).

It is found that the boundary layer of the outer flow penetrates quite a substantial amount of thickness into the stone cover, depending on the flow conditions above. Below this level the velocity remains constant. The level of turbulence in between the stones is found to be very high: 3 to 4 times higher than turbulence level over a ripple covered bed in steady current boundary layer without any externally generated turbulence. The bed shear stress is found to be very low, more than ten times smaller than in the case of a smooth base bottom without stone cover.

INTRODUCTION

Stone covers have been used for scour protection of offshore structures for decades. This was also the case for many of the offshore wind farms erected during the last decade. These wind farms are located in shallow waters and some of them are exposed to high waves and strong currents. Under these extreme conditions the scour protection of the wind turbines suffered unacceptable damages. One of the reasons for these damages to the scour protection could be the heavy wave action.

The purpose of the present study is to gain a better understanding of the interaction between the wave-induced near-bed flow and a stone cover, with the focus on the flow through the pores of the stone cover layer. A significant amount of flow and turbulence was measured for all three cases, namely one, two, and three layers of stones, covered in the tests.

SETUP

General description

The experiments were conducted in an oscillatory water tunnel with a rectangular working section of 29 cm height and 39 cm width. The horizontal working section of the oscillator is 10 m. Both ends of the horizontal part of the oscillator are connected to a vertical riser. One of the risers is open, while the other is closed and connected to a pneumatic system. During the experiments the bottom of the working section was covered with crushed stones. One, two and three layers of stones were tested. A sketch of the setup is shown in Figure 1.

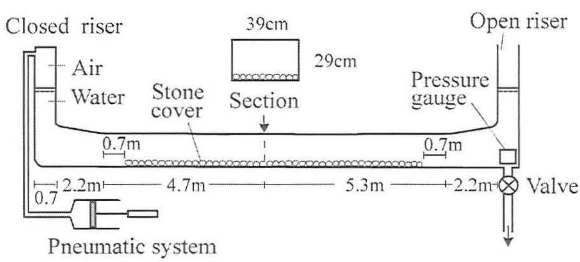

Figure 1 Sketch of the oscillating water tunnel.

The velocities were measured using a two component Laser Doppler Anemomenter (LDA). The LDA system consisted of a 300mW argon-ion laser exciter, Dantec Dynamics LDA-04 System, Dantec Dynamics 55H21 Frequency tracker, Dantec Dynamics 55N11 Frequency shifter and a laser probe with focal length of 310 mm (in air). To record the direction of the flow a pressure cell was placed at the bottom of the open riser.

The velocity measurements were made through the transparent side wall of the tunnel. The velocities above the stone layer were measured at the center line of the tunnel to reduce the effects of secondary flows due to the rectangular cross section of the tunnel. It was not possible to measure at the center line in the pores of the stone layer as the stones between the LDA probe and the pores at the center line would block the laser beams. For this reason the velocities in the pores between the stones were measured adjacent to the side wall. The sample frequency for the velocities and pressure measurements was 70 Hz, and 40 waves were recorded at each measuring point.

Three experiments have been conducted measuring the bed shear stress under three layers of stones. A one-component Dantec hot-film probe was used to measure the bed shear stress. It was mounted flush with the base bottom, and located 15.4 cm from the side wall, at the test section, and calibrated using a calibration channel. A detailed description of the measurement technique is given in Sumer et al. (1993).

The stones had a mean height of k=36 mm with a standard deviation of 9 mm. The height was measured by taking a random sample of 50 stones placed on the bottom of the tunnel, then the stone height was measured as the vertical distance from the bottom of the tunnel to the top of the stones.

Horizontal Position of the Velocity Measurements

The velocity measurements in the pores between the stones are affected by the horizontal position of the measurements. Nevertheless, measurements at the vertical line through the center of the pore would be a sensible option. However, due to the irregularities of the stones, the center of the pore is very hard to define. For this reason the "centroid" of the pore is defined, as in the following (Figure 2):

1. The points of contact A and B between the horizontal projection of two adjacent stones and the side wall of the tunnel are identified.
2. The location of point C: The middle point between points A and B, is found.
3. The horizontal line through point C, perpendicular to the line between A and B, intersects the horizontal projection of the two stones at point D.
4. The centroid P is defined as the middle point between points C and D.

The velocity was measured across the vertical line passing through point P. Twenty different pores were measured.

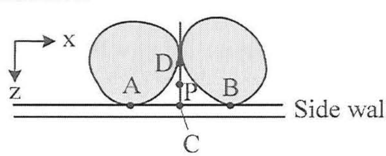

Figure 2 Definition of the centroid, plan-view.

TEST CONDITIONS

The maximum free stream velocity in the experiment was limited by the stability of the stones. The stones were stable for velocities smaller than approximately 1.1 m/s; free stream velocities larger than this would cause movements of the stones which were unacceptable for the experiment. To ensure stability for the stones a free stream velocity of approximately 1.0 m/s was used for the experiments (1.0 m/s for one layer of stones, 0.95 m/s for two layers of stones and 0.96 m/s for three layers of stones).

The wave period was governed by the natural frequency of the oscillation in the tunnel, as a wave period very different from the natural period of the tunnel would "contaminate" the velocity signal. The natural period of the flume was measured to be between 9.73 s and 10.02 s for no stones and 3 layers of stones, respectively. As the difference between the natural periods is small, the wave period was kept constant at T=9.73 s for all the experiments.

RESULTS

The velocities are phase and "pore" averaged; first the velocities are averaged over N_w=40 wave periods:

$$\tilde{u}(y,\omega t) = \frac{1}{N_w}\sum_{n=1}^{N_w} u\big(y,\omega\big(t+(n-1)T\big)\big) \tag{1}$$

where u is the measured horizontal, streamwise velocity in position P (see Figure 2) and elevation y (fixed), ω is the angular frequency of the oscillatory flow and t is the time. Then they are averaged over the N_p=20 measured pores:

$$U(y,\omega t) = \frac{1}{N_p}\sum_{m=1}^{N_p} \tilde{u}(m,y,\omega t) \tag{2}$$

ωt=0° is defined as the zero-up-crossing in the streamwise velocity in the field above the stones.

The phase- and pore-averaged horizontal velocities for three layers of stones are shown in Figure 3. The velocities are almost constant, for the particular phases, up to 6 to 7 cm above the base bottom then they increase towards the top of the stone cover. The region between y=6-7 cm and the top of the stones is influenced by the outer flow. The constant velocity layer is independent of the boundary, regardless of the number of stone layers. There will of course be a thin boundary layer at the base bottom.

There is a slight difference in the magnitude of the positive and the negative horizontal velocities. This is caused by the steady streaming induced by the convergent/divergent flow at the inlets from the risers, see Sumer et al. (1993a). This is also influencing the vertical velocities.

Due to the rectangular shape of the cross section of the tunnel, a secondary flow will appear in the cross section causing an upward-directed flow adjacent to the side wall. These secondary flows are directly linked to the streamwise flow; the larger the streamwise flow, the larger the secondary flows. As seen in Figure 4 there is a general upward directed flow in the pores. However, this is larger for the phases from ωt=0° to ωt=90° than for the phases of ωt=180° to ωt=250°. The reason is that the streamwise velocity is larger for the phases from ωt=0° to ωt=90° than from ωt=180° to ωt=250°, as seen in Figure 3.

The phase- and pore-averaged horizontal velocities for two layers of stones are shown in Figure 5. As in the case of three layers of stones, the boundary layer flow over the stone cover in the outer flow penetrates into the stone cover over a depth of 4 cm below which the velocity remains constant, the constant velocity layer.

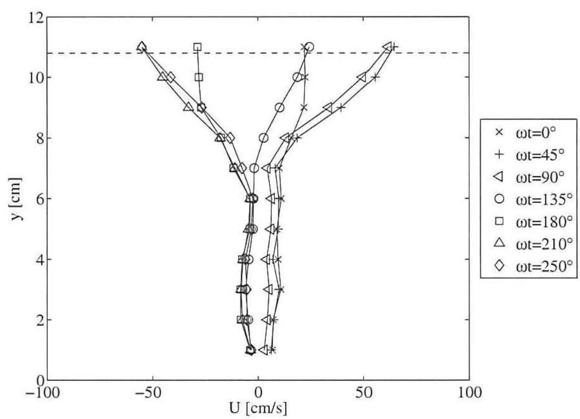

Figure 3 The velocity profiles of horizontal phase- and pore-averaged velocities. Three layers of stones. Dashed line: The average height of the stones.

The phase- and pore-averaged horizontal velocities for one layer of stones are shown in Figure 6. As in the cases of three and two layers of stones the outer boundary layer penetrates into the stone layer. In this case down to 1 cm above the base bottom. This shows that the constant velocity layer has become rather thin and it is expected, in the analogy with the two and three layer cases.

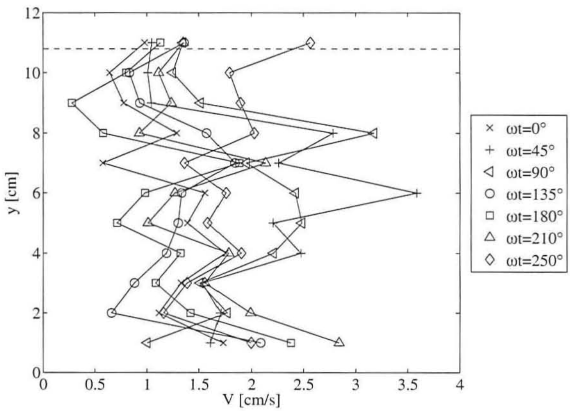

Figure 4 The velocity profiles of vertical phase- pore-averaged mean velocities. Three layers of stones. Dashed line: The average height of the stones.

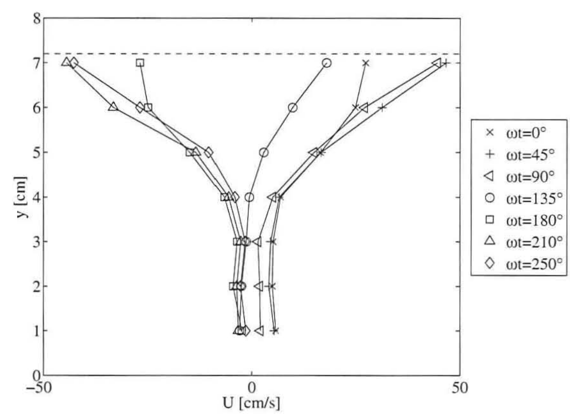

Figure 5 The velocity profiles of horizontal phase- and pore-averaged mean velocities. Two layers of stones. Dashed line: The average height of the stones.

As seen from Figure 3, Figure 5 and Figure 6, the horizontal velocities are significantly larger in the case of three layers of stones than in the case of one and two layers of stones. The level of turbulence is not influenced by this effect.

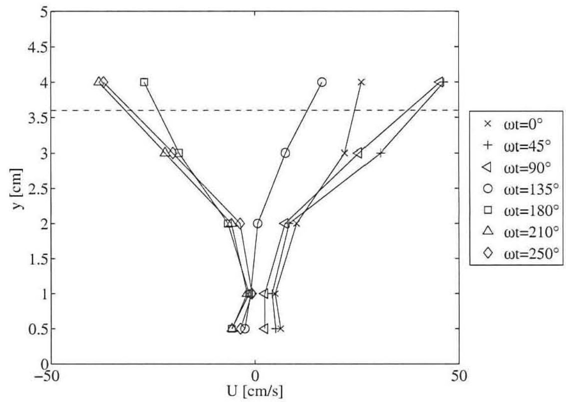

Figure 6 The velocity profiles of horizontal phase- and pore-averaged mean velocities. One layer of stones. Dashed line: The average height of the stones.

The phase- and pore-averaged horizontal turbulent velocities for three layers of stones are shown in Figure 7. The turbulent velocity is defined as:

$$U_s(y,\omega t)=\frac{\sum_{i=1}^{N_P}\sqrt{\left[u'(i,y,\omega t)\right]^2}}{N_P} \tag{3}$$

where N_P is the number of pores, u' is the measured oscillatory component of the horizontal velocity and y is the vertical position. The turbulent velocities are very large over the entire stone cover. At the top of the stone cover they are between 7 and 12 cm/s decreasing to 2.5 to 4 cm/s 1 cm above the base bottom. The turbulent velocities are almost constant in the constant velocity layer.

The phase-average of the bed shear stresses under three layers of stones are shown in Figure 8. The bed shear stresses were measured in three different layouts of the stones. The bed shear stresses measured in pore 1 and 2 were measured in the middle of the horizontal projection of a pore. In the case of pore 3 there was an offset in the streamwise direction. As seen in the figure the bed shear stress in pore 3 has a peak between 250° and 310° there is around 4 to 5 times higher than the bed shear stress measured in the two other pores. The reason for this can be the offset of the measuring position or the actual layout of the stones around the measuring point.

The bed shear stress is varying between 0.06 and 0.97 cm^2/s^2. This is a very low bed shear stress. For example Jensen et al. (1989) reported bed shear stresses up to around 10 cm^2/s^2 for an undisturbed oscillatory flow over a smooth bed with U_{m0}=0.45 m/s. However, if the critical Shields number is reached for sediment under the stone protection a high rate of bed load is expected, due to the high level of turbulence. Sands with grain size of 0.05 to 0.1 mm will be unstable under the measured bed shear stress, assuming a critical Shields parameter of 0.03 and s=2.65. Fig. 14 in Sumer et al. (2003) gives the dimensionless bed load discharge as function of the Shields parameter for different levels of turbulence near the bottom. The dimensionless bed load discharge in Sumer et al. (2003) is defined as:

$$\Phi_b = \frac{q}{\sqrt{g(s-1)d_{50}^3}} \tag{4}$$

where q is the discharge, g is the acceleration due to gravity, s is the specific gravity of the sediment and d_{50} is the mean size of the sediment. The dimensionless level of turbulence near the bottom is in the same publication defined as:

$$\left(\frac{\sqrt{\overline{u'^2}}}{U_{fb}}\right)_0 \tag{5}$$

where U_{fb} is the friction velocity at the bottom, $U_{fb} = \sqrt{\tau_0 / \rho}$.

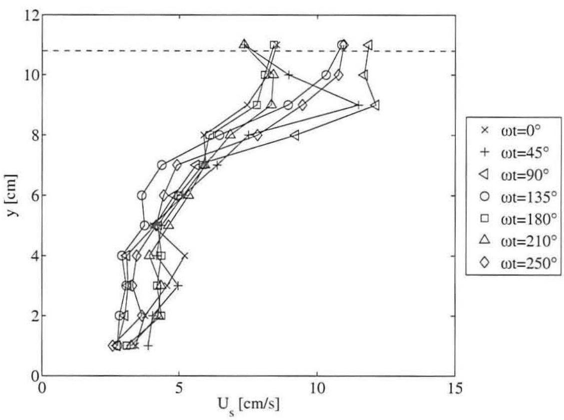

Figure 7 The horizontal phase- and pore-averaged turbulent velocities for different phase values. Three layers of stones.

A representative dimensionless peak level of turbulence will then be around 6 (ωt=45°, U_s=4 cm/s and τ/ρ=0.5 cm^2/s^2), see Figure 7 and Figure 8. The highest values of the dimensionless turbulence level given in Sumer et al. (2003) are 2.5 to 2.75. Using this and assuming that the Shields parameter reach 0.06 will give a dimensionless bed load of around 0.03. This is a really high value for so small Shields numbers. A typical dimensionless turbulence level over a ripple covered bed in current without any externally generated turbulence will be 1.7 and that will give a dimensionless bed load discharge around ten times smaller.

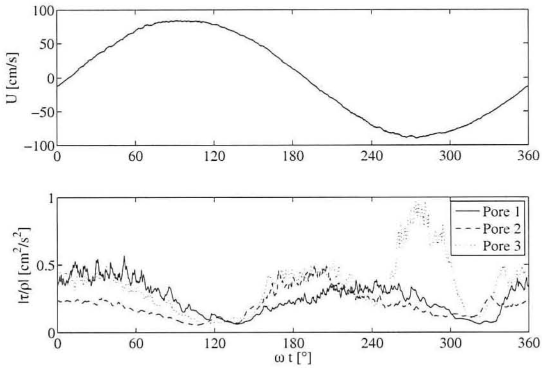

Figure 8 Phase-average of the horizontal free stream velocity and the bed shear stress measured under three layers of stones. Bed shear stresses in three different pores are presented.

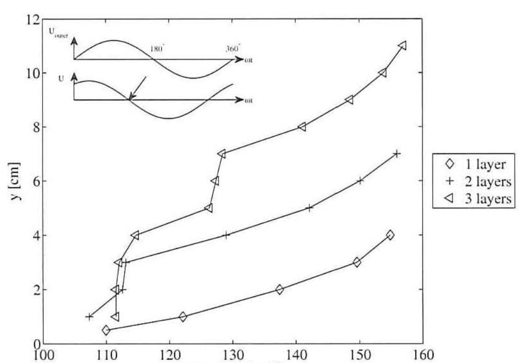

Figure 9 Profiles for zero-down-crossing phase for one, two and three layers of stones.

The zero-down-crossing phase for the three setups is shown in Figure 9. There is a large change in the zero-crossing phase from the top of the stones to the base bottom of around 45°. This is expected as the flow velocities in the stone layer is relatively small compared to the free flow velocity and the flow resistance in the stones is large. This means that the momentum of the flow in the stone layer will be "dissipated" faster than the momentum in the free flow when the pressure gradient reverses.

CONCLUSION

The velocities and turbulence have been measured in the pores of a stone cover under an oscillatory flow. Cases with one, two and three layers of 4 cm large stones have been tested. In the case of three layers of stones the bed shear stress at the base bottom was also measured. It is found that the boundary layer of the outer flow penetrates into the stone cover over a depth of 4 cm. Below this level the velocity remains constant, the constant velocity layer. The level of turbulence in between the stones is found to be very high: 3 to 4 times higher than turbulence level over a ripple covered bed in steady current boundary layer without any externally generated turbulence. The bed shear stress is found to be very low, more than ten times smaller than in the case of a smooth base bottom without stone cover.

ACKNOWLEDGEMENT

This research was carried out as part of the Statkraft Ocean Energy Research Program, sponsored by Statkraft (www.statkraft.no). The study was partially supported by the Danish Council for Strategic Research (DSF)/Energy and Environment under the program Seabed Wind Farm Interaction (http://sbwi.dhigroup.com, sagsnr. 2104-07-0010) and DHI (www.dhigroup.com). During his two years Master course, F. Stevanato was sponsored by "Universita' degli Studi di Padova" and the TIME network of Engineering Schools.

REFERENCES

Jensen B.L., Sumer B.M. and Fredsøe, J. (1989). *"Turbulent oscillatory boundary layers in high Reynolds numbers"*. J. Fluid Mech., vol. 206, 265-297

Sumer B.M., Chua, L.H.C., Cheng N.-S. and Fredsøe, J. (2003). *"Influence of turbulence on bed load sediment transport"*. J. Hydraulic Eng., Vol. 129, No. 8, 585-596.

Sumer B.M., Arnskov M.M., Christiansen, N. and Jørgensen, F.E. (1993). *"Two-component hot-film probe for measurements of wall shear stress"*. Exp. Fluids, vol. 15, 380-384.

Sumer B.M., Laursen, T.S. and Fredsøe, J. (1993a). *"Wave boundary layers in a convergent tunnel"*. Coastal Engineering, vol. 20, 317-342.

Gap Scour at a Stepped Concrete Block Grade Control Structure

J. S. Lai[1], S. C. Tsung[2], Y. M. Chiew[3] and F. Z. Lee[4]

1. Hydrotech Research Institute, National Taiwan University No. 1, Sec. 4, Roosevelt Road, Taipei, 10617 Taiwan. Tel 886-2-33662617 jslai525@ntu.edu.tw
2. Hydrotech Research Institute, National Taiwan University No. 1, Sec. 4, Roosevelt Road, Taipei, 10617 Taiwan. Tel 886-2-33662618 yinwei99@ms26.hinet.net
3. School of Civil and Environmental Engineering, Nanyang Technological University 50 Nanyang Avenue, Block N1-01a-27, 639798 Singapore. Tel +65 67905308 cymchiew@ntu.edu.sg
4. Department of Bioenvironmental Systems Engineering, National Taiwan University No. 1, Sec. 4, Roosevelt Road, Taipei, 10617 Taiwan. Tel 886-2-33662614 d94622004@ntu.edu.tw

ABSTRACT

Stepped concrete block grade control structures are widely used in Taiwan to protect riverbeds from degradation and to dissipate the associated high energy of flow over weirs. The grade control structures are constructed with concrete blocks with a specific gap width and drop height across the river. Large-size stones are placed in the gaps as lateral support. This type of structure is subject to the threat of edge and gap scour. In this study, the gap scour between the concrete blocks was examined by executing a series of physical model experiments in a laboratory flume. The configurations and depths of scour at the various approach discharges were monitored and measured to examine the scour characteristics between the blocks. Three phenomena were discovered: (1) the scour depths in specific areas were significantly deeper than the height of the cubic blocks, (2) the largest gap scour occurred at low discharges, and (3) eroded stones migrated along the gaps as bed load transport rather than suspension. The longitudinal gaps between the blocks were sealed to minimize stone movement. A physical model test was used to verify the method. The results indicated a maximum scour depth reduction of up to 98.7 %. The present paper proposes a new design methodology that includes consideration of the block heights and gap scour at low discharges.

Key Words: stepped concrete block grade control structure, gap scour

INTRODUCTION

Weirs for water intake and check dams for bridge protection are structures built across rivers. These structures raise the level of water, which increases the scour potential to the downstream riverbed. Engineers use stepped concrete block grade control structures to protect the riverbed from degradation and dissipate high flow energy. The structures normally are constructed using concrete blocks arranged in a stagger and descending manner (see Fig. 1a). Specific gap width and drop height between blocks are used and large-size stones are placed in the gaps as lateral support. The gaps aligned in the streamwise and transverse directions are called longitudinal and lateral gaps.

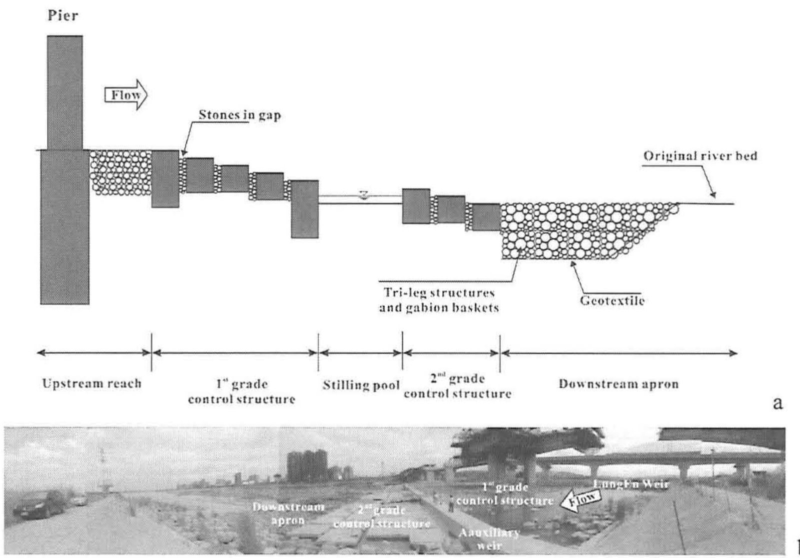

Fig 1 (a) Sketch of protection structures in a river; (b) protections downstream of Lung-En Weir, Toucian River in northern Taiwan

The stepped concrete block structures are designed based on the concept of armoring effect. The slope of the structures is steeper than that of the original riverbed slope in order to minimize construction cost. The protection structure comprises different components. Figure 1(a) illustrates the different components of a typical river bed protection work in Taiwan, namely (1) an upstream reach; (2) a first stepped concrete block grade control structure; (3) stilling pool; (4) a second stepped concrete block grade control structure; and (5) a downstream apron. Figure 1(b) shows an example of the riverbed protection downstream of the Lung-En Weir in the Toucian River in northern Taiwan. The structure consists of two sets of stepped concrete block grade control structures.

Lin (1999, 2000) classified the causes of failure of stepped concrete block grade control structures in Taiwan as gap scour, edge scour, head-cutting and lateral erosion. He found that gap scour (35.5%) and edge scour, (22.6 %), are the dominant causes of failure. Edge scour is more visible than gap scour. Research on gap scour is few compared to the studies on edge scour. Armoring effects with reference to the relationship between sediment transport and approach flow conditions are widely studied. Raudkivi and Ettema (1982) studied the stability of an armor layer before extending it to include scour protection around piers (Raudkivi and Ettema, 1985).Worman (1989, 1992) studied the transport of fine sediment with an armor layer. Sumer et al. (2001) applied flow visualization techniques to examine the suction mechanism of fine sediment under an armor layer. They found that vortices that formed in the gap sucked out fine sediment particles between the gravels. They published a regression equation to estimate bed degradation due to the erosion of the fine sediment. The results of the Sumer et al. (2001) study explains the physics government sediment entrainment and mobility associated with the gap scour of stepped concrete block grade control structures. Researchers must keep in mind the significant difference in the geometrical layout and compositions of both structures in order to apply their findings. The focus of this study is gap scour. It describes the failures, which are due to gap scour in the field. This study examined the characteristics of gap scour by executing a series of physical model experiments in a laboratory flume. The configurations and scour depths at various discharges were monitored and measured to examine the physics of scouring between the blocks. The study measured and analyzed the maximum scour depths with the aim of establishing a design methodology to reduce gap scour.

FIELD INVESTIGATIONS

This study carried out a field investigation at the stepped concrete block grade control structure downstream of Highway No.1 in Ta-Chia River in central Taiwan in November 2009. The Taiwanese Highway Department built this structure in 1999 to restrain general scour or degradation of the riverbed near the bridge. Sediment was then stored upstream of the structure. The width of the structure is 840 m. They constructed the structure using 3-m cubic concrete blocks. The height of the first-row blocks is 5 m. The gap width between the blocks is 50 cm. There are 20 step-drops in the flow direction and the drop height of each step is 50 cm. The constructors connected the blocks by using steel wires. They initially submerged the second 10 steps of the stepped concrete block grade control structure with the original bed material.

Figure 2 shows pictures of the stepped concrete block grade control structure. The field investigation showed all steps exposed because of degradation downstream. The major cause of the degradation was the sediment deposition upstream, which raised the bed elevation upstream. The controller raised the water head, which resulted in high velocity movement downstream. The scour potential also increased on the downstream reach. The study found edge scour at the toe of the structure and a few blocks in the last row tilted or overturned due to extra-added support. Figure 2 reveals how the removal of stones in the gaps resulted in the weakening of the lateral supports and tilting of the blocks. The stones in the gaps provided lateral support.

The blocks sank due to the excessive gap scour around them. Figure 2(a) shows the titling blocks and Figure 2(b) provides a closer view of the gap scour. The scour depth in some of these areas was more than 3 m, more than the height of most of the concrete blocks. The gap widths increased because of the movement of individual concrete blocks. This further enhances stones mobility, causing the steel wires to break. The tilting and sinking of the blocks compromised the structure in terms of energy dissipation. Titling and sinking of the blocks eventually spreads in all directions. The high velocity of the water in this area flushes out most fine bed material. Figure 2(c) shows the formation of a scour hole at the upstream end of the structure. A scour hole will have a profound effect on the stability of the first row of blocks. This is a serious problem for the preservation of the overall stability of the structure.

Fig 2 Failure of stepped concrete block grade control structure located downstream of Highway No.1 in Ta-Chia River in central Taiwan (November 2009): (a) blocks tilting and sinking; (b) deeper scour depth than block height; and (c) a scour hole upstream of the sinking area

EXPERIMENTS

Sumer et al. (2001) discussed how the vortices that developed in the gaps formed within the gravel have contributed to the entrainment of the fine sediment particles. Such a mode of entrainment is unlikely to take place in the present condition in which the main flow passes through the gap (Tsorng et al. 2009). Evidence from both field and laboratory observations reveal that the stones in the lateral gaps, gaps that are perpendicular to the main flow direction, were stable.

Conventional design of stepped concrete block grade control structures considers the stability of concrete blocks by block weight under a specific flow condition, usually at high designed discharges (Lagasse et al. 1997, Wu 2004, Guo and Chang 2006). They ignore failures due to gap scour. Recent experiences in Taiwan have exposed the fallacy of that design philosophy. A better understanding of the mechanism and the development of a design methodology that takes into consideration gap scour is necessary. This study used a physical model in order to study gap scour for design modification and a proposal for cost-effective gap scour countermeasures.

It was necessary to determine the general block geometry and stone dimension to match the real flow and scour characteristics. Most of the stepped concrete block grade control structures in Taiwan consist of five steps with an individual step drop-height of 50 cm. The projection area of the block is 2 x 2 m2 and the gap width is 50 cm. The average median stone size used to fill the gap is about 20 cm. We fixed the upstream and downstream beds of the structure since this study only considered the scour between the blocks. A rectangular flume was used that is 30 cm in width, 60 cm in height, and 1500 cm in length located at the Hydrotech Research Institute, National Taiwan University to carry out the experiments. At least six blocks in each row was determined in order to display the global scour patterns and avoid boundary effect. A 1/50 scaled model was built in the flume using scaled blocks with an area = 4 x 4 cm2. The block heights were at least 25 cm to measure the equilibrium scour depth in the gaps. The scaled gap width and drop height of each step was 1 cm. A uniform sand with median grain size = 3.56 mm was used to fill the gaps. Figure 3 shows the model design of the experiments. The researchers simulated the slope of 0.01 in the model tests since the longitudinal bed slope of rivers in Taiwan generally ranges from 0.01 to 0.001. The study adopted a clear-water condition without sediment influx from upstream. The bed elevation in the gaps was the same as the ambient block surfaces before the tests. We performed two sets of experiments, the "all-gaps-opened" and "only-lateral-gaps-opened" conditions.

The scour depth variations were monitored in both cases to ensure the equilibrium scour condition. The scour hole approached its equilibrium stage in approximately 15 minutes. The measurement of the bed elevation in both the longitudinal and lateral gaps continued for 40 minutes. The average bed elevation in the stream wise direction was the mean value of all the measured data in the transverse direction at the same streamwise positions. This study tested the scour depth variation for five different unit discharges, which varied from 0.008 to 0.051 m2/s. Table 1 summarizes the test conditions of all the experiments conducted in this study.

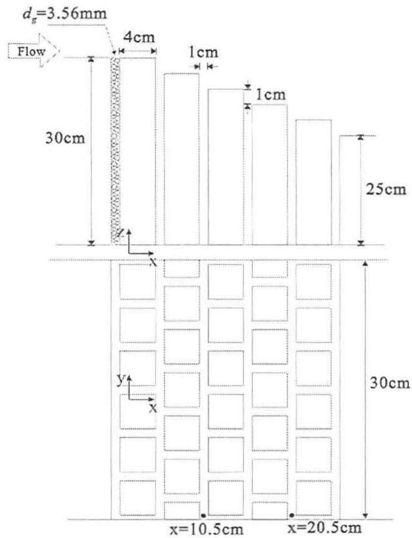

Fig 3 Sketch of scaled physical model and dimensions (side and top view)

Table 1 Experimental conditions and measured data: q – unit discharge; d_{50} – diameter of stone in the gaps; S_b – flume slope, S_{rm} – slope of structure; y_{bm} –lowest bed elevation; x_s – the corresponding position of y_{bm}; y_{bo} –original bed elevation at x_s; e –maximum scour depth

Run	q [m^2/s]	d_{50} [mm]	S_b	S_{rm}	y_{bm} [cm]	x_s [cm]	y_{bo} [cm]	e [cm]
GS1	0.0089	3.56	0.01	0.20	21.98	15.50	27.00	5.02
GS2	0.0188				21.65	12.00	28.00	6.35
GS3	0.0314				22.31	15.50	27.00	4.69
GS4	0.0433				22.91	15.50	27.00	4.09
GS5	0.0505				23.45	15.50	27.00	3.55
GSP1	0.0089	3.56	0.01	0.20	28.75	5.50	29.00	0.25
GSP2	0.0188				29.92	0.50	30.00	0.08
GSP3	0.0314				25.79	20.50	26.00	0.21
GSP4	0.0433				25.84	20.50	26.00	0.16
GSP5	0.0505				28.80	5.50	29.00	0.20

RESULTS AND DISCUSSIONS

Mechanics of Gap Scour

Figure 4 shows the temporal development of the measured scour depth for Test GS3 at x = 10.5 and 20.5 cm, where x is the horizontal distance measured from the upstream end of the structure (see Fig. 3). The figure shows that the rate of scour is high in the initial stages of the test. Figure 5 presents the process of gap scour evolution. The stones near the surface of the block eroded as soon as the flow arrived, Figure 5(a). Gap scouring occurred in the first three rows. Figure 5(b) shows the gap scour at t=6 seconds. It indicates how the eroded stones migrated along the longitudinal gaps downstream with no apparent sediment suspension. Some stones spun behind the block due to flow separation within the wake created by the downstream flow. The measured temporal scour depth development curves show that the scour rates gradually decreased with time. Figure 5(c) shows the gap scour at t = 30 seconds. The stones driven by the flow in the gaps continued to move slower downstream. The downstream flow temporarily deposited some of the stones behind the final-row of blocks. These stones eventually washed away. The stones in the gaps stabilized as the equilibrium state approached. The behavior of stone mobility in the gaps was similar to bed load transport dominated by gap flows.

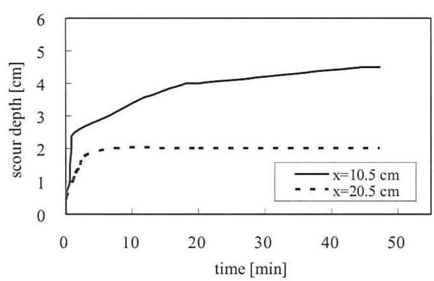

Fig 4 Temporal development of gap scour at x = 10.5 and 20.5 cm (monitoring position referred to Figure 3)

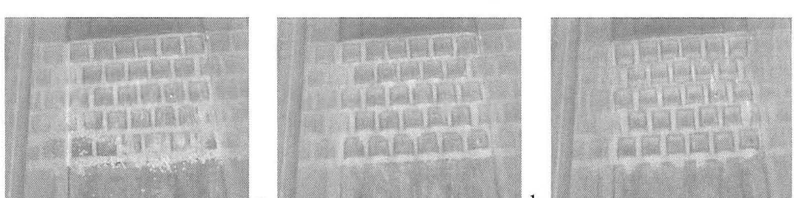

a b c

Fig 5 Gap scour evolution of Test GS3 at (a) 2 sec; (b) 6 sec; (c) 30 sec

Scour of "All-Gaps-Opened" Conditions

Figure 6 shows the average measured bed profiles for Tests GS1 – GS5. Table 1 contains the measured data, which includes the lowest bed elevation, their corresponding position, and the maximum scour depth. The figure shows that the average bed profiles for all five tests were similar. The bed elevation decreased from the first-row of blocks reaching the minimum level near the third-row of blocks. The minimum level was approximately 15 cm downstream from the leading edge of the structure and coinciding with the lateral gap behind the third-row of blocks. The bed elevation increased beyond this location.

The measured data show that the maximum scour depth for all the tests was e = 6.35 cm, which is for Test GS2, with unit flow rate, q = 0.0188 m2/s. The scour depth in the gap of a stepped concrete block grade control structure was not directly proportional to the approach discharge. The scour depth increased as the discharge increased initially. It then decreased with a further increment of the approach flow rate. Serious gap scour occurs at a low or moderate rate of flow. The design of a stepped concrete block grade control structure should be re-examined in light of this finding. Furthermore, the gap scour depth at the first to third-row of blocks could potentially exceed 4 cm, which was deeper than the height of the adjacent cubic blocks. The gaps can potentially be completely entrained leaving no lateral support for the concrete blocks. The height of the concrete blocks used in Taiwan is insufficient. Field investigation supported this conclusion, Figure 2a.

The experimental results show that the design of stepped concrete block grade control structures should consider the stability of a single concrete block under a designed flow condition and the extent of the gap scour depth. The designed height of a block must be more than the estimated scour depth and the block height should be dependent on its location.

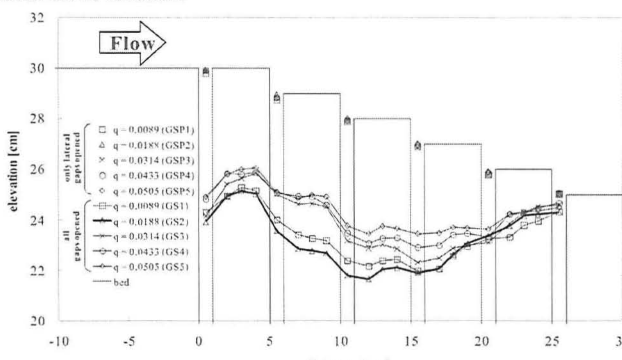

Fig 6 Mean bed form profiles in the gaps

Scour of "Only-Lateral-Gaps-Opened" Conditions

The results for the condition of "all-gaps-opened," Tests GS1 –GS5, show how the stones migrate along the lateral and longitudinal gaps in the downstream direction. We proposed to open only the lateral gaps and validate the performance (Tests GSP1–5). Figure 6 and Table 1 show the average bed elevation and measured data for the "only-lateral-gaps-opened" condition. The maximum scour depth for all the tests was 0.25 cm (Test GSP1), which was significantly lower than the 6.35 cm for the "all-gaps-opened" condition. Entrainment of the stones from the gaps resulted from the vortices in the gaps when only lateral gaps existed in a stepped concrete block grade control structure. The main flow above the lateral gaps drived the vortices in the gaps. The required mean velocity of flow to suspend the 3.56-mm stones on a flat flume was 115 m/s (Hjulstorm, 1935 , Yang 1996). The maximum velocity of flow over the current stepped concrete block grade control structure for all cases was 112 m/s (at x = 26 cm, Test GSP5). The velocities in the gaps were less than the requirement for the initiation of sediment suspension.

The experimental results show that the presence of longitudinal gaps promoted the development of gap scour. The scour depth appeared to be unrelated to the approach discharge in contrast to the all-gaps-opened Tests GS1–5. The reduction of the bed elevation from 6.35 cm (Test GS2) to 0.08 cm (Test GSP2) was significant. The test showed that sealing the longitudinal gaps could effectively reduce the scour depth by up to 98.7 %. Solid or impermeable material could be considered to seal the longitudinal gap.

CONCLUSIONS

This study identifies the main causes for failure of stepped concrete block grade control structures in Taiwan through field investigations. One of the main causes of failure in these structures is gap scour. The scaled physical model experiments with different approach discharges were conducted to study this problem. The longitudinal gaps of the structure were sealed to reduce the extent of gap scour. This method showed a significant decrease in development of scour holes.

The study considered the five-stepped concrete block grade control structure used in Taiwan. The shape of the average bed profiles in the longitudinal gaps was similar for different approach discharges. The experimental results indicated the maximum scour depth was in the middle of the stepped concrete block grade control structure. The experimental results also showed that the scour depth in the first three rows of blocks was deeper than the height of the cubic blocks. The designed block height used in Taiwan was insufficient. The scour depth in the gaps was not proportional to the approach discharge. The maximum scour depth in this study occurred at a relatively low approach discharge. The designers of these structures need to consider gap scour at comparatively low or intermediate discharge and adequate block heights. The experimental results showed that sealing the longitudinal gaps offers a promising solution to keep the stones within the lateral gaps.

ACKNOWLEDGEMENTS

Financial support for this work was provided by the Water Resources Planning Institute, Taiwan. We thank Ms.Y. L. Chen for her help in data measurement and analyses.

REFERENCES

Lin, C (1999). "Study on technology and tactics for scour prevention of cross-river structures." *Public Construction Commission.* (in Chinese)

Lin, C (2000). "Guidelines for preventions of scour due to free overfall and hydraulic jump." *Sinotech Engineering Consultant.* (in Chinese)

Raudkivi, A.J. and Ettema, R. (1982). "Stability of armour layers in rivers." *J. Hydraul Div.,* 108 (9): 1047-1057.

Raudkivi, A.J. and Ettema, R. (1985). "Scour at cylindrical bridge piers in armored beds." *J. Hydr. Engrg.,* 111 (4): 713-731.

Worman, A. (1989). "Riprap protection without filter layers." *J. Hydr. Engrg.,* 115 (12): 1615-1630.

Worman, A. (1992). "Incipient motion during static armoring." *J. Hydr. Engrg.,* 118 (3): 496-501.

Raudkivi, A. J. (1998). "Loose boundary hydraulics." *Balkema.*

Sumer, B.M., Cokgor, S. and Fredsoe, J. (2001). "Suction removal of sediment from between armor blocks." *J. Hydr. Engrg.,* 127 (4): 293-306.

Tsorng, S.J., Yang, Z.S., and Lai, J.S. (2009). "Measurements of flow field between blocks in various geometries." *18th Conference of Hydraulic Engineering, PingTung, Taiwan,* H-11. (in Chinese)

Lagasse P.F., Byars M.S., Zevenbergen L.W. and Clopper, P. E. (1997). "Bridge Scour and Stream Instability Countermeasures." *Federal Highway Administration,* FHWA-HI-97-030.

Wu, C.S. (2004). "Design of stepped concrete block grade control structure." *Master Thesis,* Hydraulics & Ocean Engineering, NCKU, Tainan, Taiwan. (in Chinese)

Guo, Y.H. and Chang, Y.Z. (2006). "Failure mechanisms of flexible grade control and protections. "*Hydraulics,* (16): 201-210. (in Chinese)

Hjulstorm, F. (1935). "The Morphological Activity of Rivers as Illustrated by River Fyris." *Bulletin of Geological Institute,* Uppsala, vol.25, chap3.

Yang, C.T. (1996). "Sediment Transport - theory and practice." *McGraw-Hill.*

Centrifuge Modelling of an Internal Erosion Mechanism

V.D. Le[1], D. Marot[2], L. Thorel[1], J. Garnier[1] and P. Audrain[1],

[1] Université Nantes Angers Le Mans, Laboratoire Central des Ponts et Chaussées, Centre de Nantes, Département Géotechnique Eau Risques, Route de Bouaye, BP 19, 44340 Bouguenais, France ; email : van-duong.le@lcpc.fr, luc.thorel@lcpc.fr, jacques.garnier@lcpc.fr, philippe.audrain@lcpc.fr

[2] University of Nantes, Institut GeM, BP 420 44606 Saint-Nazaire Cedex, France; email : didier.marot@univ-nantes.fr

ABSTRACT

Suffusion is an internal erosion mechanism, which means the transport of fine particles within the soil due to hydraulic interflows. With the objective to characterize this mechanism and to study a scale effect presented in literature, a specific centrifuge bench is designed.

Test specimens of mixture of sand and kaolinite are compacted in rigid walled cells. The specimen height is selected according to the applied gravity and the chosen effective stress. After saturation, specimens are subjected to centrifugal acceleration and to a vertical downward flow under a constant hydraulic head.

The effect of the applied hydraulic gradient is examined and the study underlines that the increase of specimen height induces the decrease of critical hydraulic gradient and the increase of erosion rate. A new energy analysis of tests is developed, linking the expended power to the erosion rate. This method permits to avoid the effect of specimen height.

INTRODUCTION

Under the action of water flow, grains constituting the soil of embankment of dams or dikes can be detached and transported. This process is named internal erosion and can induce the failure of hydraulic earth structures. The two main phenomena of internal erosion in uncracked soils are backward erosion and suffusion. This paper deals with suffusion which concerns only finer fraction of soil. The fine particles are detached and transported through a skeleton constituted by coarser grains.

With a hydraulic approach, several authors have developed expressions that relate initiation of internal erosion to the critical hydraulic gradient. Sellmeijer (1988) proposed an expression of hydraulic gradient that is inversely proportional to the length of seepage path. Moreover Li (2008) performed tests with a large and a small permeameter. For a same type of tested specimen and identical mean vertical effective stress, Li (2008) observed that the critical hydraulic gradient can be seven times higher with the small permeameter than with the large one.

A program of centrifuge tests was performed on clayey sand to characterize suffusion process and to examine the scale effect on initiation and development of suffusion. The use of the centrifuge allows to vary the height of the soil sample keeping constant the hydraulic gradient and the distribution of effective stresses.

CENTRIFUGE TEST DEVICE

The device comprises a rigid wall cylinder cell, a hydraulic control system and an effluent sampling system. The device is placed in the basket platform of the LCPC centrifuge in order to reproduce stress states upon full scale (see Figure 1).

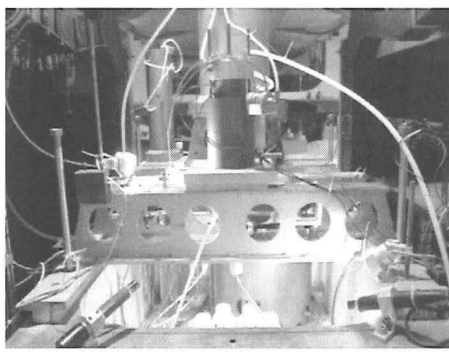

Figure 1. General view of the centrifuge bench.

A downward seepage flow is applied to the specimen under a constant hydraulic gradient. The fluid circulates into the top of the specimen using a layer of glass beads to diffuse the fluid on the specimen contact interface uniformly. At the bottom of the specimen, the funnel-shaped draining system is specially designed to allow the transport of eroded particles.

The cell outlet is connected with an effluent sampling system by a drainage pipe and a needle valve. This type of gate is chosen to enable the opening even under a high gravity. The draining system is equipped with a controlled vent which avoids the generation of a depression in the specimen induced by the outlet valve opening. The opening of downstream valve is realized in flight when the selected centrifugal acceleration is reached.

To perform a sampling of the effluent during the test duration, a rotating system is developed (see Figure 2) and thanks to a camera it is controlled remotely from the centrifuge operator's room.

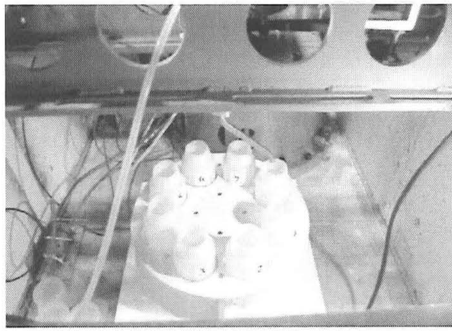

Figure 2. View of rotating effluent sampling system.

EXPERIMENTAL PROCEDURE

Tested materials

The tested material is a mixture composed of 90% of Fontainebleau sand and 10% of clay. The washed Fontainebleau sand has grain unit weight of 26.5 kN/m^3 and a grain size distribution within the range 0.1 mm to 0.4 mm. The clay is kaolinite Speswhite (grain unit weight: 26.5 kN/m^3), without deflocculation its grain size distribution is measured between 0.5 μm and 0.125 mm. Figure 3 shows the grain size distribution of tested materials.

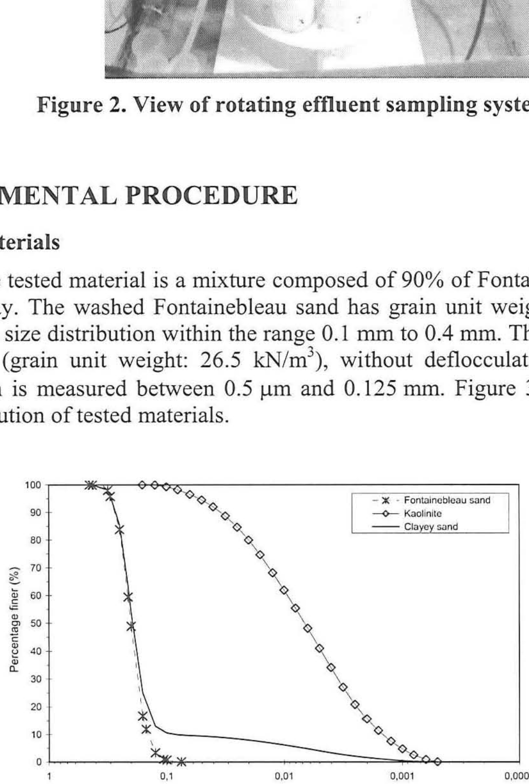

Figure 3. Grain size distribution of tested materials.

Specimen reconstitution and test principle

The sand is first mixed with a water content of 8 %. While mixing continues, power clay is progressively added. The mixture is left for 24 hours (at least) in a plastic bag in order to improve the moisture homogeneity. Specimens are realized by compaction in 73 mm diameter cells. The reduced scale model height is within a range from 60 mm to 120 mm. For 60 mm height, the compaction is made in six layers of 25 blows with a mini Proctor rammer. The saturation phase begins by an injection of carbon dioxide at the specimen bottom. Saturation is completed in upward direction by using demineralized and deaerated water.

The saturated specimens are then subjected to centrifuge acceleration with a g-level N between 10 and 60. During the centrifugation, a constant hydraulic head H_w (origin = bottom of specimen) is applied at the top of specimens by using demineralized and deaerated water. Hydraulic gradient is determined by:

$$i = \frac{H_w N}{H_m} \tag{1}$$

where H_w: water height applied on the specimen top,

N: centrifugal acceleration factor,

H_m: reduced scale model height.

With the objective to take into account the influence of the test duration, the average rate of erosion is expressed by:

$$\dot{m} = \frac{m_{\text{eroded clay}}}{S\,d} \tag{2}$$

where $m_{\text{eroded clay}}$: cumulative dry mass of eroded clay, S: specimen cross section; d = test duration.

TESTS RESULTS AND DISCUSSION

Influence of hydraulic gradient

Twenty tests were performed. The average erosion rate versus the hydraulic gradient shows a great variation of erosion rate for an identical value of hydraulic gradient (see Figure 4).

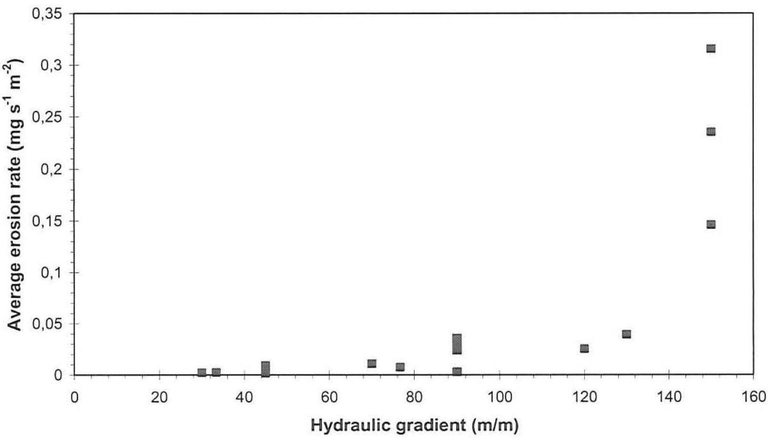

Figure 4. Influence of hydraulic gradient on average rate of erosion.

Scale effect

According to Li (2008)'s conclusions, the value of critical hydraulic gradient decreases with the specimen height. To verify this influence, the reduced scale model height is distinguished in Figure 5.

For reduced scale model height of 90 mm, the average erosion rate (expressed in mg s^{-1} m^{-2}) seems to be related to hydraulic gradient by a power law which is:

$$\dot{m} = 0.23\ 10^{-3}\left(10^{0.02\ i} - 1\right) \quad (3)$$

This relation confirms the power law proposed by Bendahmane et al. (2008) for the maximum value of erosion rate in the case of clay suffusion:

$$\dot{m}_{max} = 12\left(10^{0.02\ i} - 1\right) \quad (4)$$

where $\dot{m}_{max}$ is the maximum value of erosion rate.

The factor 12 is higher than the factor in equation (3). This difference of magnitude may be due to three different reasons. Bendahmane et al. (2008) performed tests on different clayed sand. The type of sand and also the clay were different than materials tested in this study. Equation (4) was defined for the maximum value of erosion which was measured instantaneously by an optical sensor (Bendahmane et al., 2008). Unfortunately this optical sensor can not stand high gravity. Thus the sensor could not be used for this test program and the sampling device leads to an average value of erosion rate for each step of the sampling. The third reason is related to the greater filter pore opening size (4mm) for Bendahmane et al. (2008) tests. The filter opening size is an important parameter to quantify erosion rate and with a 0.08 mm filter opening, the critical gradient can be six to seven times smaller than with a 4 mm filter opening (Marot et al., 2009).

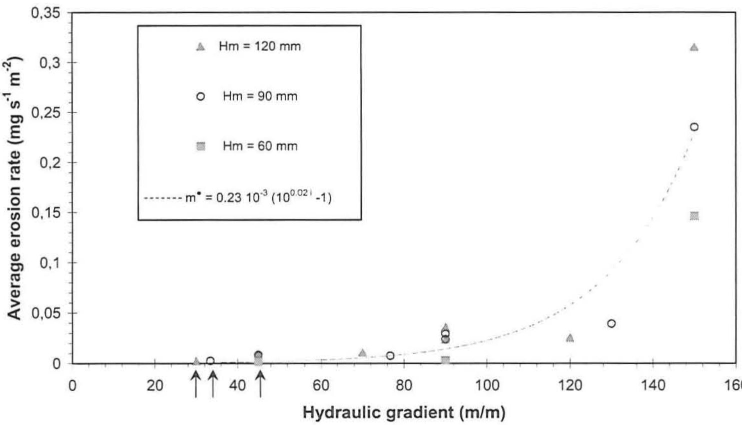

Figure 5. Influence of hydraulic gradient and reduced scale model height on average erosion rate.

In Figure 5 it can be noted that the critical hydraulic gradient to initiate suffusion (indicated by arrows in Fig. 5) decreases with the reduced scale model height: $i_{cr} = 45$ m/m for Hm = 60 mm, $i_{cr} = 33$ m/m for Hm = 90 mm and $i_{cr} = 30$ m/m for Hm = 120 mm.

These values of critical hydraulic gradient confirm Li (2008) conclusions: the magnitude of critical hydraulic gradient decreases with tested specimen height.

In order to study the scale effect on development of suffusion, Figure 6 plots the average erosion rate versus the reduced scale model height for identical value of hydraulic gradient and effective stress.

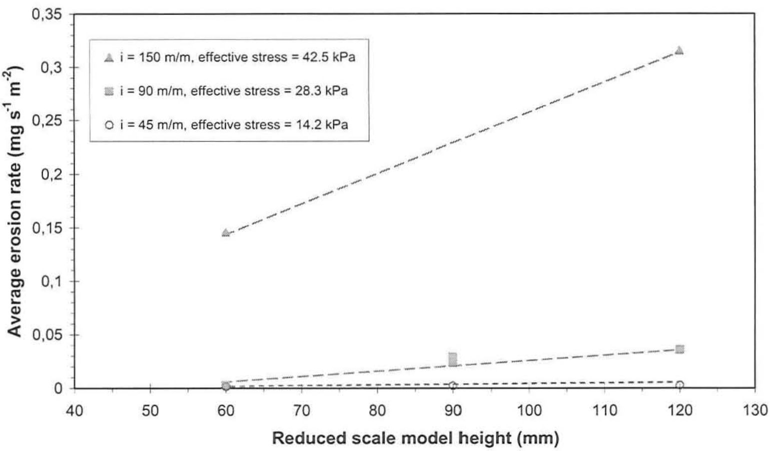

Figure 6. Influence of reduced scale model height on average rate of erosion.

Rate of erosion appears as a function of reduced scale model height so the scale effect seems to influence both initiation and development of suffusion.

Energy analysis

The new analysis proposed here is based on a fluid energy dissipation model and this energy is assumed to be transformed into erosion.

The energy equation is applied between the upstream section A and the downstream section B of the specimen (White, 1999). A volume V of fluid, with a mass M and a density ρ, is assumed with a surface S in contact with environment. The external surface of the volume is oriented by its normal vector $\vec{n}$ from fluid to environment. The energy equation for the fluid through the specimen can be written by the following equation (Regazzoni, 2009):

$$\frac{dE}{dt}=\frac{d}{dt}\iiint_{Mass}\left(e_{int}+\frac{u^2}{2}+\vec{g}\,\vec{z}\right).dM=\frac{\partial}{\partial t}\iiint_{Volume}\left(e_{int}+\frac{u^2}{2}+\vec{g}\,\vec{z}\right)\rho dV+\oint\!\!\oint_{S}\left(e_{int}+\frac{u^2}{2}+\vec{g}\,\vec{z}\right)\rho(\vec{U}\,\vec{n}).dS \qquad (5)$$

and

$$\frac{dE}{dt}=\frac{dE_{Ther}}{dt}+\frac{dW}{dt} \qquad (6)$$

with: E_{Ther}: energy exchange between the system and the environment; W: mechanical work between the sections A and B; e_{int}: internal energy of the fluid; U: velocity of the fluid, components (u, v, w); g: gravity; z: coordinates

Three assumptions can be used to simplify the equation. The temperature (isothermal in time), so the internal energy (e_{int}) are assumed constant on the volume. The system can be considered as adiabatic, only mechanical work (W) takes place between sections A and B, that can be expressed by:

$$\frac{dE_{Ther}}{dt} = 0 \tag{7}$$

The assumption of a steady state (locally in time) allows neglecting the unsteady term of the kinetic energy. Finally equation (5) becomes:

$$\frac{dW}{dt} = \oiint_S \left(\frac{u^2}{2} + \vec{g}\,\vec{z} \right) \rho \left(\vec{U}\,\vec{n} \right) dS \tag{8}$$

The total energy dissipation is the sum of energy dissipation by pressure, by shear stress at the interface fluid-solid and by viscosity and turbulence in the fluid phase. The shear stress is assumed to cause erosion, so the dissipation of total energy in the system can be written as:

$$\frac{dW}{dt} = \frac{d\,W_{pression}}{dt} + \frac{d\,W_{intra\ fluid}}{dt} + \frac{d\,W_{erosion}}{dt} \tag{9}$$

The temporal derivative of work done by pressure is defined by:

$$\frac{dW_{pression}}{dt} = -\oiint_s P(\vec{U}\,\vec{n})\,ds \tag{10}$$

Equations (8) to (10) lead to:

$$\frac{d\,W_{intra\ fluid}}{dt} + \frac{d\,W_{erosion}}{dt} = \oiint_S \left(\frac{u^2}{2} + \vec{g}\,\vec{z} + \frac{P}{\rho} \right) \rho \left(\vec{U}\,\vec{n} \right) dS \tag{11}$$

The flow conservation with a same specimen section on the whole length leads to assume the same average velocity in the sections A and B. Equation (11) becomes:

$$\frac{d\,W_{intra\ fluid}}{dt} + \frac{d\,W_{erosion}}{dt} = \oiint_S \left(\vec{g}\,\vec{z} + \frac{P}{\rho} \right) \rho \left(\vec{U}\,\vec{n} \right) dS = Q\,\Delta P + \rho\,g\,\Delta z\,Q \tag{12}$$

It is assumed that the dissipation of energy is mainly transformed into erosion and the dissipation intra fluid is neglected. In consequence, the temporal derivative of mechanical work through erosion can be expressed by:

$$\frac{d\,W_{erosion}}{dt} = Q\,\Delta P + \rho\,g\,\Delta z\,Q \tag{13}$$

For convenience, the temporal derivative mechanical work by erosion is named erosion power. The energy dissipation is the temporal integration of the instantaneous erosion power for the test duration.

With the objective to verify the energy analysis ability to avoid scale effect as previously described, Figure 7 presents the average rate of erosion versus the erosion power.

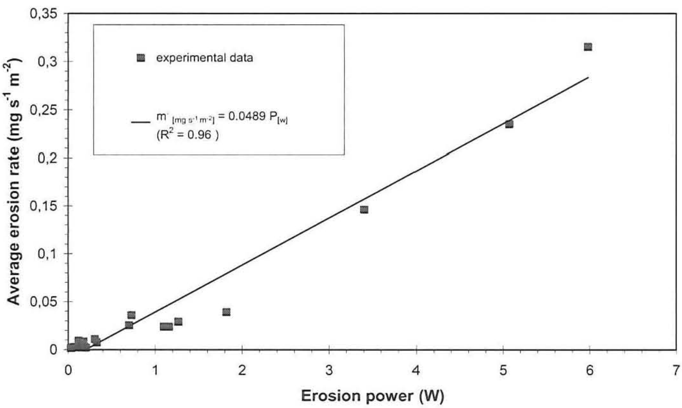

Figure 7. Average erosion rate versus erosion power.

The linear increase of the average erosion rate (expressed in mg s^{-1} m^{-2}) according to the erosion power P (expressed in W) can be estimated by:

$$\dot{m} = 0.0489\ P \qquad \text{(correlation coefficient } R^2 = 0.96) \qquad (14)$$

For each test, the eroded clay mass and total energy dissipation can be determined by integration over the test duration. Figure 8 shows that the eroded clay mass (in mg) can be related to the total energy dissipation (E, in J) by a linear law as:

$$m_{\text{eroded clay}} = 0.0017\,(E - 60) \qquad (R^2 = 0.95) \qquad (15)$$

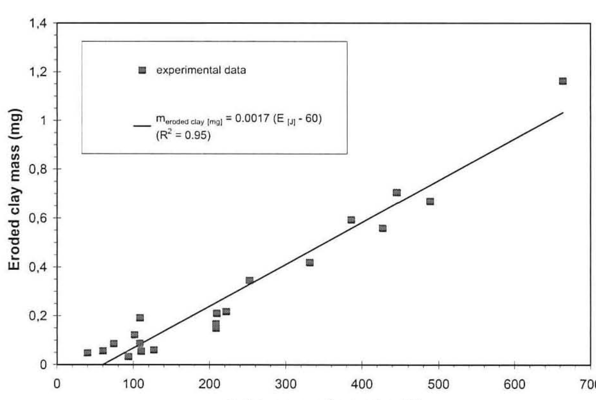

Figure 8. Eroded clay mass versus total energy dissipation.

So the analysis based on energy dissipation offers the potential for a consistent interpretation of suffusion tests, without significant influence of specimen height.

CONCLUSION

A centrifuge bench is developed in order to characterize the sensitivity of a clayey sand to suffusion process and to study scale effect. The realized study examines the influence of hydraulic gradient on initiation and development of suffusion. Using the hydraulic gradient concept, the characterization of suffusion depends on the tested specimen height. The difference in the results is in the magnitude of critical hydraulic gradient and of erosion rate.

An energy analysis of interstitial fluid is made. By integrating over the time, the eroded clay mass is linearly correlated to the energy dissipation. Using the energy analysis, the suffusion characterization does not depend on specimen height.

ACKNOWLEDGEMENT

The authors wish to acknowledge the support of the Region Pays de la Loire (project R2GC) for this research.

REFERENCES

Bendahmane F., Marot D., Alexis A. (2008). "Parametric study of suffusion and backward erosion." *J. of Geotechnical and Geoenvironmental Engineering (ASCE)*, 134 (1): 57-67.

Li M. (2008). Seepage induced instability in widely graded soils, *PhD thesis*, University of British Columbia, Vancouver, 300 p.

Marot D., Bendahmane F., Rosquoet F. Alexis A. (2009). "Internal flow effects on isotropic confined sand-clay mixtures." *Soil & Sediment Contamination, an Int. J.* 18 (3): 557-567.

Regazzoni P.-L. (2009). Confrontation et analyse d'érodimètres et caractérisation de la sensibilité à l'érosion d'interface. *PhD thesis,* Université de Nantes, 155 p.

Sellmeijer J.B. (1988). On the mechanism of piping under impervious structures, *PhD thesis*, Delft University of Technology, 56 p.

White F. M. (1999). Fluid Mechanics 4th ed., book, edition Mc Graw-Hill, 826 p.

Experimental Study of the Influence of Non-Hydrostatic Pressure in Rip Rap Pier Protection

Allen Bateman-Pinzon[1], Vicente Medina-Iglesias[1], Alex Guevara[1]

Sediment Research Group (GITS-UPC) Technical University of Catalonia. Calle Gran Capitán s/n. 08034 Barcelona. Spain. Email: allen.bateman@gits.ws; vicente.medina@gits.ws

ABSTRACT

The non-hydrostatic pressure distribution is one of the main factors that affect the particles motion threshold around piers. The present paper focuses on the comparison of the motion threshold between circular-shaped and square-shaped piers under the influence of the non-hydrostatic pressure factor. A total of 30 runs were performed with different geometric dimensions and different Rip Rap diameter protection. The hydrostatic pressure factor distinguishes quite well between circular-shaped and square-shaped piers. Comparison with other authors has been made in order to extract some conclusions and confirm the experimental data. The non-hydrostatic pressure distribution on bed surfaces is very important to distinguish between different behaviors in sediment transport bed processes; local scour protection around piers is only an example. The main idea would be finding the threshold of motion of the Rip Rap around the circular-shaped and square-shaped base piers.

Keywords: Rip Rap, Pier Scour, Threshold of Motion

INTRODUCTION

Obstructions elements such as piers located in the middle of streams are responsible for the formation of local scour around thereof. Bridge-Piers are one of the most famous elements due to the impact on highways traffic flow and normal life when they fail; literally the bridge collapses and the traffic is interrupted. The present work relates to to understanding the influence of the non-hydrostatic pressure distribution around piers as one of the most important parameters which affects the maximum depth of the local scour, (Bateman et al 2005).

Bridge piers and abutments collapsing frequently occurs around the world and is the main factor causing bridges to fall due to hydraulics and scour, in the U.S at least 90% of the times, Richardson et al. (1993). Protection of piers using Rip Rap is one of the principal actions carried out to avoid the collapse under storm conditions.

The present paper focuses on the threshold of the movement of particles located around the pier, being different due to the shape of the pier, -square or circular-, and to the influence of the non-hydrostatic pressure present around the pier.

All the experiments were performed at the Morphodynamic Laboratory of the Hydraulic, Marine and Environmental Department of the Technical University of Catalonia under the supervision of GITS-UPC(Sediment Transport Research Group).

Some theoretical aspects

In order to analyze the process describing the initial process of threshold of motion of particles around piers, the parameters can be classified as:

Parameters describing the fluid: The density (ρ) and the viscosity (ν) depend on the fluid temperature and salinity.

Parameters describing sediment: 50% by weight passing through the sieve size (D_{50}), the standard deviation of the sediment bed (σ), the density of the sediment (ρ_s) and the internal friction angle (ϕ).

Parameters describing the flow: Water depth (h), mean velocity (u), mean friction slope (S_f), mean slope of the stream (S_0), shear stress (τ_0) and non-hydrostatic pressure head increment $(\Delta P/\gamma)$.

Parameters describing the obstacle: The shape and dimension (Circular with diameter (D) or Square with length size (D)), the orientation related to the flow direction (α).

Relation of the main authors whom work with Rip Rap protection in bridge piers

There are many authors since Shields fixed the basis of threshold of motion of particles. Indeed the first Rip Rap equation used is the relation between the dynamic fluid stress and the submerged weight of the sediment particle is the Shields relationship, (FHWA Hydraulic Engineering Circular, 1997). An expression of the same type was introduced by Isbash (1935) ((FHWA Hydraulic Engineering Circular, 1995), the change in the formulation was based on the equivalence of fluid stress to momentum flux. The equation explicitly presents now the velocity. The Maynord (1989) formula was the most extended one to evaluate the Rip Rap diameter protection. The equation is similar to Isbash equation, including the mean velocity of the fluid, but introducing a factor which depends on the sediment characteristics D_{30}.

In 1973 Neill proposed a dimensionless formula including the Froude number to an exponent of 2.5, but excluding the velocity, see Choi et al (2002). Also you can look for Bonasoundas (1973), Quazi Peterson (1973) Breusers et al. (1977), Parola C. (1993), Chiew (1995), Richardson et al. (1993), Yoon & Park (1997), Launchlan & Melville (2001), and finally Unger et al. (2006). All the formulae have the same type of parameters, Froude number, sediment size ratio or standard deviation, the size of the pier and in general adjusting parameters. The most exhaustive formula is presented by Launchlan & Melville (2001) and can be expressed as:

$$\frac{D_{50}}{h} = K_y K_D K_C K_T K_S K_\alpha Fr^2 \quad (1)$$

wherein, K_y is a parameter that includes the sediment depth Rip Rap protection with respect to the water depth, K_D is a parameter that includes the influence of the pier diameter, K_C is a factor relative to the protected area, K_T includes the effect of the protection depth, K_S corresponds to the influence of the pier shape, K_α is the alienation of the pier with respect to the flow direction. Launchlan & Melville (1999) describe several parameters which influence the Rip Rap protection, but which only fixed the K_y and K_C parameters.

Experimental Set Up

The Flume: To carry out the experiments, the flume from the Morphodynamic Laboratory of GITS-UPC was used; one of its devices consists in a flume having a 40 cm width and 60 cm height rectangular section and a total length of 9 meters. The discharge capacity goes from 250 cm^3/s to 50 l/s controlled by two valves and two ultrasonic flowmeters. The downstream level was controlled by a mechanical slice gate locates at the end section of the flume.

Sediment characteristics: Four types of sediment size were used and were classified from big to small size with colours; white stones, black stones, gray stones, and gray filtered stones. Density and sediment size distribution can be seen in Table 2. The density was measured with a pycnometer and due to the uniform size of the stones, the mean diameter was measured with a Venier Caliper, at least one hundred stones were measured from a quarter sample methodology.

Experiment arrangement: A 10 cm gray stone base material (D_{50}=7.34 mm) was placed at the middle of the flume filling a length of 3m, as shown in Figure 1. The slope of the flume and sediment bed was 0°. The piers were placed one by one in the downstream at the 2/3 end part of the sediment bed.

Piers: Three circular-shaped and four square-shaped piers, for a total of 7 piers were used; the diameters of the circular piers were 1, 2 and 3 cm and the sides of the square-shaped ones were 1, 2, 3 and 4.2 cm.

Pressure measuring system: The pressure system consists of four water manometers strategically placed, the first one was placed 1 meter upstream from the front pier in order to control the normal pressure, the second one was placed in front of the pier and the third one was placed at the lateral side of the pier. The lateral manometer was placed at the point where the minimum pressure was predicted to appear. The manometers were formed by two mm diameter plastic tubes and the water inside them was coloured with red ink to facilitate the visualization of the measurements.

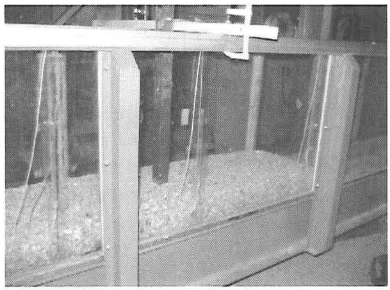

Figure 1. A photograph showing the experiment set up.

Discharge and water level measurements: Discharge measurements were carried out with an ultrasonic flowmeter and corroborated by a rectangular weir, and the water levels, upstream and downstream from the pier, were measured with a level meter.

Threshold of motion: The experiment purpose is to visually detect the threshold of motion of the particles surrounding the pier, as well as to precise the location where a displacement of stones is more susceptible to occur. The material was arranged at least in two layers around the pier covering an area more than three times the width of the pier.

The Rip-Rap movement was visually detected, when one or two stones were dragged by the flow stream; the threshold of the motion location was marked. In this case the discharge, pressure and water levels were measured. The discharge was increased by steps, firstly with the gate in a completely closed position, and then the gate was manually opened by steps, thus increasing the stress on the material until a movement has or has not been noticed. As soon as the range of discharges were accomplished, another pier and/or material was replaced, and the experiments was started again. Ninety experiments were established in order to detect the threshold of motion of the particles; six of them were discarded due to specific problems or due to a wrong procedure being carried out. The bigger problems were detected when small pier or sediment size begun to affect accuracy of measurements shown by data having the highest deviation.

A VORTEX ENERGY APPROACH.

The threshold of motion can be defined as the moment in which the work done by the fluid (vortex activity or stresses) exceeds the work done by gravity plus friction forces. It is possible to analyze the power of the fluid and gravity forces to find a relationship between the parameters at the moment in which the threshold of motion occurs.

The power of the flow has to be equal to the rate of work done by the gravity in order to reach the threshold of motion. The power caused by gravity on the particle can be evaluated by multiplying the fall velocity of the particle times the submerged weight per unit mass.

$$P_g = (S_s - 1) g \cdot \omega_s \tag{1}$$

Wherein P_g is the work done by gravity forces per unit time and unit mass, S_s is the relative density of the bed sample, g is the gravity acceleration and ω_s is the fall velocity for a specific diameter. By definition the specific submerged weight is $R=S_s-1$. The dimensions of equation (1) are L^2/T^3.

The fall velocity, simply expressed, can be evaluated by the following expression:

$$\omega_s = \sqrt{\frac{4}{3}\frac{D}{C_D} Rg} \tag{2}$$

On the other hand some of the main reasons for sediment motion around the pier, and therefore the threshold of motion of the particles, are the horseshoe vortices formed in front of the pier. In Bateman et al. (2005) a relationship between the flow velocity and the power per unit mass contained in the vortex is:

$$\frac{\frac{1}{2} d\left(u^2\right)}{dt} = \frac{u^3}{\ell} \tag{3}$$

Batchelor (1953) expresses the kinetic energy velocity dissipation per unit mass of the vortex. Wherein, u is the mean approximation velocity and ℓ the integral length. Indeed the flow in the channel must have enough energy per unit time as to maintain the vortex activity. This is the main idea to relate the activity of the vortex with the sediment stability in the bed close to the pier. The length of the vortex has to be proportional to the depth of water in front of the pier, which is the depth of water in the approximation zone plus the excess of elevation due to the stagnancy of the flow in front the pier. That is:

$$\ell = \alpha\left(s_e + y_0\right) \tag{4}$$

Wherein S_e is the excess of depth of water in front of the pier and y_0 the approximation depth and α is a parameter to approximate the best vortex size, (see Bateman et al., 2005).

It is possible to define a parameter which compares the rate of work done by gravity forces with the vortex dissipation rate as:

$$\phi_p = \frac{d\left(\frac{1}{2}u^2\right)}{P_g} = \frac{u}{R\omega_s} F^2 \tag{5}$$

Wherein F is the Froude number evaluated with the velocity approximation and the depth of water in front of the pier. The parameter α has no relevance in this context and thus its value was assumed to be one. The relationship ϕ_p greatly depends on the correct determination of the velocity, due to its dependence on the cube of the velocity.

PRESSURE GRADIENT DETERMINATION

In order to evaluate the influence of the non-hydrostatic pressure distribution a couple of manometers were installed around the pier. The idea is to evaluate the pressure drop around the pier. As we do not know exactly where the pressure drop will be higher, we measure the pressure difference between the front (maximum pressure) and the side (minimum pressure). The measurement of the difference of pressure is done along a length l_m between those points. This gradient generates an internal flow inside the sediment pores; the internal flow exerts a force on the particle which is normal to the surface of the bed facilitating the threshold of motion of the particles. It is difficult to predict where will the force be bigger, unless a 3D internal and external coupled flow numerical model is applied. The length l_m between measures is used to evaluate the gradient from both points of measure.

Figure 2 shows a schematic view of the pier location and the points on which the pressure has been obtained. The pressure gradient is calculated as:

$$\frac{\partial P/\gamma}{\partial l} = \frac{(P_S - P_P)}{\gamma L_m} \qquad (6)$$

Ps and Pp are the pressure measured at the surface of the test bed at the front and side of the pier respectively and γ is the water specific weight.

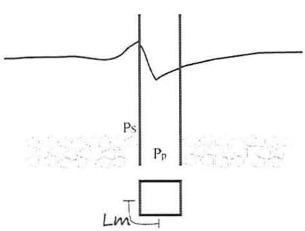

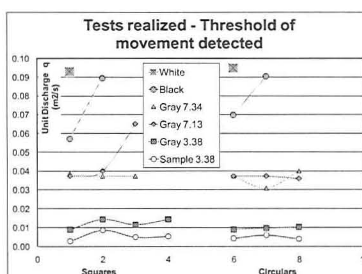

Figure 2. a) Description of the measurement pressure points. L_m is the length between the measurement pressure points P_p and P_s. b) Unit discharge at the threshold of motion for piers.

EXPERIMENTAL RESULTS

Table 1 shows the unit discharges in which the threshold of motion was detected. The data in parentheses shows no movement detected, the dash line shows non carried out experiments.

Table 1. Unit discharges in m^2/s at which threshold of motion was detected during the experiments.

Type and width of pier number –shape-size-(cm)	White (16,9mm)	Black (13,32mm)	Grey (7.34 mm)	Grey (7.13mm)	Grey (3.38mm)	Sample (3.38mm)
1 □ 4.2	[0,093]	0,057	0,039	0,037	0,009	0,003
2 □ 3	-	[0,089]	0,037	0,040	0,014	0,009
3 □ 2	-	-	0,037	0,065	0,011	0,005
4 □ 1	-	-	-	-	0,014	0,005
6 ○ 4	[0,095]	0,070	0,037	0,037	0,009	0,004
7 ○ 3	-	[0,090]	0,031	0,037	0,010	0,006
8 ○ 2	-	-	0,040	0,036	0,010	0,004

Figure 3 shows the plots of the experiments of ϕ_p vs. the grain size and pier size ratio: Dg/Dp. The behavior of the circular- and square-shaped piers are clearly different. The lines show the conservative limit that can be used to make a design for pier protection.

In order to prove the consistency, a comparison with the main formulas was carried out. The method used was simply applying the formulae to the condition of the experimental data in order to obtain the D50 to protect the pier. Figure 6 shows the results upon applying the following formulae: Isbash, Richardson, Breusers, Bonasoundas and the implicitly presented formulation; more dispersion is detected compared with results shown in Figure 3.

Table 2 indicates the net pressure force due to the pressure gradient, and as can be seen it bears the same order of magnitude of the weight of the particle, depends on the type of experiment, but oscillates around from half to twice the weight of the particle. This quantity is relevant and capable for reducing the Shields parameter of the Rip Rap.

The most relevant results are given in Figure 3, wherein the variation of the pressure gradient respect to the relationship between sediment diameter and the pier width is shown. The data lies on two different paths; one for circular-shaped piers and the other for square-shaped piers. The white stones were so big and heavy that no movement thereof was caused during the experiments and therefore were not included in the table. From 90 equilibrated experiments only on 29 occasions a movement was detected. Figure 4 shows the points in which a stone has been seen moving. Note that all moving particles lie in the side part of the pier, except in the square-shaped ones where some particles were moving in the back. The color graduation represents the relation between the grain size Dg with respect to the pier size Dp. The position at which the particles of sediment start to move are marked in a plan view in Figure 4.

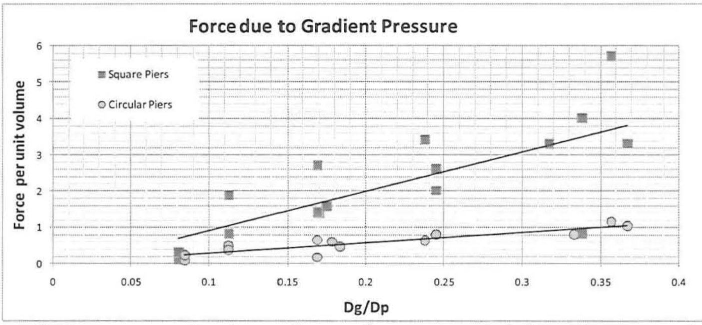

Figure 3. Force per unit volume due to the pressure gradient in square-shaped and circular-shaped piers to different grain size to pier size ratio.

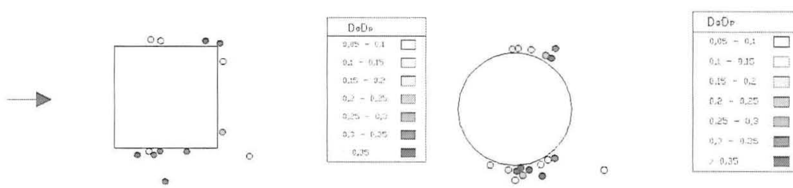

Figure 4. Points at which the particles start to move-colors are the ratio D_g/D_p. a) Square-shaped pier b) Circular-shaped pier

PROPOSED RELATIONSHIP

Once the pressure influence in both square-shaped and circular-shaped piers has been reached, we define the product of equation (5) and (6) and plot the results against the ratio between grain size and pier size diameter. This relationship is defined as:

$$\phi_p = \frac{u}{R\omega_s} F^2 \frac{\Delta P}{\gamma L_m} \tag{7}$$

Figure 5 shows the plots of the experiments of ϕ_p vs the grain size and pier size ratio: D_g/D_p. The behaviors of the circular- and square-shaped piers were clearly different. The lines show the conservative limit that can be used for designing pier protection.

In order to prove the consistency, a comparison between the main formulae was made. The method was carried out by simply applying the formulae to the conditions of the experimental data in order to obtain the D_{50} to protect the pier. Figure 6 shows the results of applying the following formulae: Isbash, Richardson, Breusers, Bonasoundas and the formulation implicitly presented in (7); there was more dispersion detected compared with results shown in Figure 3.

Table 2. Results obtained from the pressure gradient in the experiments at the threshold of motion in square-shaped and circular-shaped piers.

Pier Type	Material	ρ_s	D_{50} (m)	Pressure increment (meters headwater)	Mean length Lm (m)	Pressure Gradient (m/m) or (T/m3)	Mean Particle Pressure Force (gr)	Particle Weight (gr)	Pressure Force over Weight (%)
Square 4.2	Grey	2.9	0.0071	0.029	0.021	1.38	0.262	0.556	47.1
Square 4.2	Grey	2.9	0.0073	0.033	0.021	1.57	0.325	0.607	53.6
Square 4.2	Black	3	0.0133	0.069	0.021	3.29	4,061	3,671	110.6
Square 3	Grey	2.9	0.0073	0.03	0.015	2.00	0.414	0.607	68.3
Square 3	Grey	2.9	0.0073	0.039	0.015	2.60	0.538	0.607	88.7
Square 3	sample	2.7	0.0034	0.012	0.015	0.80	0.016	0.054	30
Square 3	Grey	2.9	0.0071	0.051	0.015	3.40	0.645	0.556	116
Square 3	Grey	2.9	0.0034	0.028	0.015	1.87	0.038	0.059	63.7
Circular 4	Black	3	0.0133	0.037	0.047	0.79	0.97	3,671	26.4
Circular 4	Grey	2.9	0.0073	0.022	0.047	0.47	0.097	0.607	15.9
Circular 4	sample	2.7	0.0034	0.004	0.047	0.09	0.002	0.054	3.2
Circular 4	Grey	2.9	0.0071	0.028	0.047	0.59	0.113	0.556	20.3
Circular 4	Grey	2.9	0.0034	0.011	0.047	0.23	0.005	0.059	8
Circular3	Grey	2.9	0.0034	0.017	0.035	0.48	0.01	0.059	16.4
Circular3	sample	2.7	0.0034	0.013	0.035	0.37	0.007	0.054	13.8
Circular3	Grey	2.9	0.0071	0.022	0.035	0.62	0.118	0.556	21.2
Circular3	Grey	2.9	0.0073	0.028	0.035	0.79	0.164	0.607	27
Circular 2	Grey	2.9	0.0071	0.027	0.024	1.15	0.217	0.556	39.1
Circular 2	Grey	2.9	0.0034	0.015	0.024	0.64	0.013	0.059	21.7
Circular 2	sample	2.7	0.0034	0.004	0.024	0.17	0.003	0.054	6.4
Square 2	Grey	2.9	0.0073	0.033	0.01	3.30	0.683	0.607	112.6
Square 2	Grey	2.9	0.0071	0.057	0.01	5.70	1,082	0.556	194.5
Square 2	Grey	2.9	0.0034	0.027	0.01	2.70	0.055	0.059	92.2
Square 2	sample	2.7	0.0034	0.014	0.01	1.40	0.028	0.054	52.4
Square1	sample	2.7	0.0034	0.004	0.005	0.80	0.016	0.054	30
Square1	Grey	2.9	0.0034	0.02	0.005	4.00	0.081	0.059	136.5
Square 4.2	sample	2.7	0.0034	0.002	0.021	0.095	0.002	0.054	3.6
Square 4.2	Grey	2.9	0.0034	0.006	0.021	0.29	0.006	0.059	9.8
Circular 2	Grey	2.9	0.0073	0.024	0.024	1.02	0.211	0.607	34.8

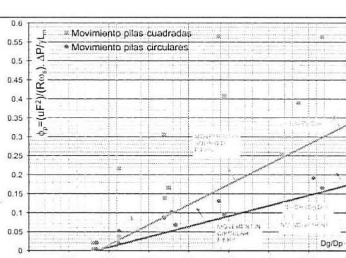

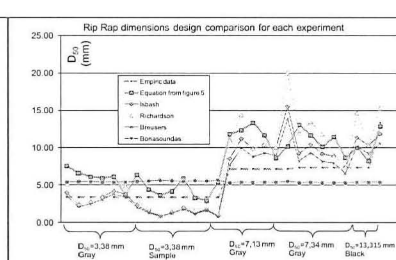

Figure 5. Plot of the equation (7) against the ratio of Dg to Dp. Figure 6. Application of the different formulae, Isbash, Richardson, Breusers, Bonasoundas and eq.(7).

CONCLUSION

The experiments that have been carried out at the Morphodynamic Laboratory of the Hydraulic, Marine and Environmental Engineering Department demonstrate the direct influence of the non-hydrostatic pressure distribution around the pier, and also that such situations are responsible in great measure for the threshold condition of the Rip Rap protection in piers. The application of the vortex power and work gravitational rate gives some physical explanation for the presence of the different parameters that will be present in the pier Rip Rap formulations.

BIBLIOGRAPHY

Bateman, A. Fernández, Parker (2005), Morphodynamic model to predict temporal evolution of local scour in bridges piers. RCEM Urbana Champain. Illinois 2005.

Breusers, H. y Raudkivi, A.J. (1991), *Scouring*. IAHR Hydraulic Structures Design Manual. A.A. Balkema, Rotterdam, Holanda.

Lauchlan, C.S. y Melville, B.W. (2001), *Riprap protection at bridge piers*. Journal of Hydraulic Engineering, Vol. 127 nº5, Mayo.

Richardson, E.V., Harrison, L.J., Richardson J.r., y Davies, S. R. (1993), *Evaluating scour at bridges*. Publ. FHWA-IP-90-017, Federal Highway Administration, Washington, D.C.

Stephen T. Maynord, James F. Ruff Steven R. Abt (1989), *Riprap design*. ASCE Journal of Hydraulic Engineering, Vol. 115 nº 7, Julio.

S.V. Isbash. 1936 "Construction of Dams by Depositing Rock in Running Water," Communication No. 3, Second Congress on Large Dams, Washington, DC.

FHWA-HI-97-030. 1997. HEC-23 http: //www.fhwa.dot.gov / engineering /hydraulics /pubs /hec /hec23.pdf.

Breusers, H. y Raudkivi, A.J. (1991), Scouring. IAHR Hydraulic Structures Design Manual. A.A. Balkema, Rotterdam, Holanda.

Chiew, Y.M. (1995), *Mechanics of riprap failure at bridge piers*. ASCE Journal of Hydraulic Engineering, Vol. 121 nº 9. Septiembre.

Choi, G.W. et al. (2002), Riprap equation for protecting the local scour at bridge piers. Journal of Korea Water Resources Association, Vol. 37 nº6.

Isbash, S. V. 1936. "Construction of Dams by Depositing Rock in Running Water," Transaction, Second Congress on Large Dams, Vol 5, pp 123-126.

Maynord S.T. (1988) "Stable Rip Rap Size for open channerl Flows" tech. Rep. HL 884-4 US Army Engineering Waterways Experiment Station, Vickburg Miss.

Parola, A.C. (1993), Stability of riprap at bridge piers. Journal of Hydraulic Engineering, Vol. 119 nº10, Octubre.

Richardson, E.V., Harrison, L.J., Richardson J.r., y Davies, S. R. (1993), Evaluating scour at bridges. Publ. FHWA-IP-90-017, Federal Highway Administration, Washington, D.C.

Unger, J. y Hager, W.H. (2006), Riprap failure at circular bridge piers. ASCE Journal of Hydraulic Engineering, Vol. 132 nº4, Abril.

Yoon, T.H. y Park, K. (2001), Effects of nonuniform bridge piers on riprap scour countermeasures. Proc. of 29th Congress of Int. Assoc. for Hydraulic Research.

IJkdijk Full Scale Underseepage Erosion (Piping) Test: Evaluation of Innovative Sensor Technology

G. de Vries[1], A.R. Koelewijn[1] and V. Hopman[1]

[1]Deltares, P.O. Box 177, 2600 MH, Delft, Netherlands; PH +31(0)88-3357398; email: goaitske.devries@deltares.nl

ABSTRACT

The IJkdijk (Dutch for 'calibration levee') is an unique Dutch facility where full scale levees are built and brought to failure with two explicit goals: to increase the knowledge on levee behaviour and to develop and test new sensor technologies for flood early warning systems under field conditions. In 2009 four experiments have been carried out, aiming at failure caused by underseepage erosion (piping). Several innovative sensor technologies have been tested during these experiments. In this article the use of fibre optics is evaluated. To ensure a proper calibration of these experimental measurements, an extensive reference monitoring program has been carried out employing proven technology. The process of seepage erosion resulted in a huge amount of advanced sensor information. The results and predictive values of the measurements are analysed, compared and evaluated.

INTRODUCTION

The IJkdijk (pronounced as 'Ikedike' and Dutch for 'calibration levee') is an initiative where knowledge on levees and sensor technology comes together. As part of the IJkdijk program, in Booneschans, the Netherlands, levees are built at full scale and brought to failure with two explicit goals: to increase the knowledge on levee behaviour and to develop and test new sensor technologies for flood early warning systems under field conditions. This should increase both the quality of the levee inspection process and the safety assessment of levees. The final goal is to develop a flood response toolbox aimed at ensuring the timely execution of appropriate measures. The IJkdijk project functions as an open innovation platform for testing sensor techniques and to improve dike technology, providing benchmarking to all contributors. By conducting experiments in a controlled environment and under pre-determined conditions, knowledge about the failure mechanisms of levees can be improved and the value of new technologies can be demonstrated. At present, more than forty companies and institutions from five different countries cooperate in this initiative.

The full-scale piping tests were performed at the location of the IJkdijk in the Northeast of the Netherlands. Two large basins were created (size 30x15m in area), each filled with a different type of sand, having a d_{50} of 150 μm and 210 μm respectively. Throughout this paper, these sands are denoted as 'fine sand' and 'coarse sand'. A clay levee with a height of 3.5m and slopes of 1V:2H was built on top of the sand by densification of smaller clay lumps. After construction a levee with a 15 m seepage length was obtained. Figure 1 shows a cross-section and longitudinal section of the full-scale tests. At the downstream side, a weir has been created to keep the downstream water level at a constant level (approx 0.15m above the sand layer). At the upstream side, the water level could be raised to a level of 3 m.

A total of four tests has been carried out:

1. Fine sand, with reference monitoring and little disturbing innovative monitoring techniques (monitoring placed with a distance to the interface sand-clay);
2. Coarse sand, with reference monitoring techniques only;
3. Fine sand, with reference monitoring techniques only;
4. Coarse sand, with reference monitoring and little and medium disturbing innovative monitoring techniques (monitoring placed with and without a distance to the interface sand-clay).

In this paper results from the first experiment are presented.

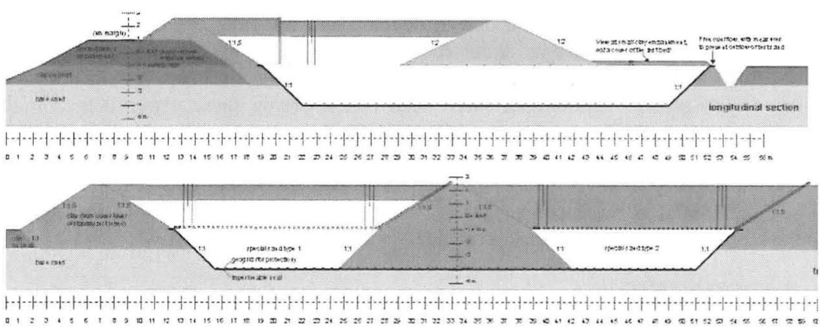

Figure 1. Cross-section and longitudinal section of the full-scale tests.

The innovative sensor technologies which have been tested during these experiments comprised measurements of deformations, vibrations and temperature by glass and plastic fibre optics, dynamic imaging by acoustics, waterleakage from self potential, deformation and well location with infrared cameras, and pore pressure, tilt and temperature from transducers integrated with MEMS technology. In this article the glass fibre optics measurements are evaluated against visual observations and pore pressure measurements from 'traditional' vibrating wire piezometers, laid in a dense grid at the interface of the levee and the sand layer.

GTC Kappelmeyer has tested the leakage detection capability of fibre optic cables in conjunction with the Heat-Up (or Heat-Pulse) method (Dornstädter, 2010). TenCate Geosynthetics, Inventec, EDF and geophyConsult have been involved in the IJkdijk Piping project to provide a monitoring solution based on optical cable and on the GeoDetect® monitoring solution (Artières, 2010).

PIPING

The process, presented in Figure 2, is considered one of the most dominant failure mechanisms of levees in the Netherlands (Havinga and Kok, 2005). The process, visualized in Figure 2, starts with heave and cracking of the soft soil top layer at the land side of the levee, caused by high water pressures which are easily transferred through the permeable sand layer. The cracks in the top soft soil layer allow for seepage. In case the water level difference between river and land side (the hydraulic head) is large enough, sand grains may be transported along with the water flow, thereby creating a pipe underneath the levee. Continued erosion may finally lead to instability and failure of the levee.

Several models and empirical relations are available to predict the occurrence of retrograde piping, of which the most well-known are the empirical rule of Bligh (1910) and the model of Sellmeijer (1988), of which the latter describes the process in most detail. However, in a recently performed safety assessment of Dutch levees using the model of Sellmeijer, a discrepancy emerged between calculation results and the opinion of levee managers. Scepticism existed on whether piping would actually result in failure of the levee and the validity of the model was questioned. A large research program was started to validate and possibly improve the model. This program and its results are more extensively described in Van Beek & Knoeff (2009) and Van Beek et al. (2010).

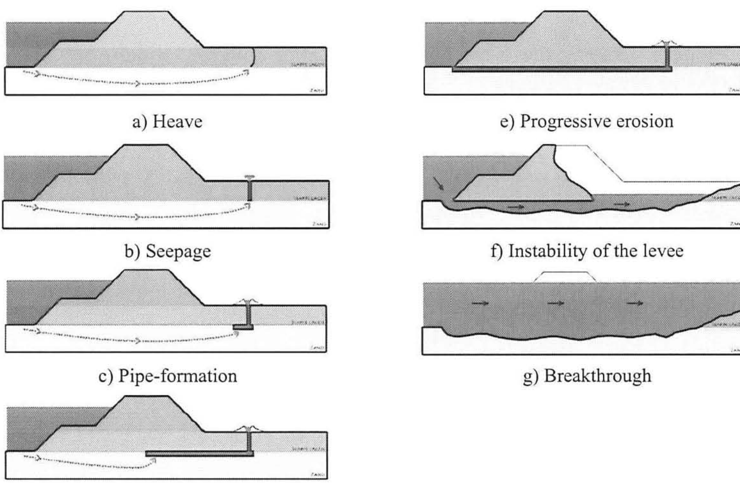

d) Pipe-formation

Figure 2. Process of retrograde erosion.

INSTRUMENTATION

Reference monitoring

The piping formation, more specifically the growth of the pipe, can be monitored by the pore pressure meters. The pore pressure meters have been placed in 4 rows of 16 pressure meters each. These rows were placed at 0.2 m, 1.2 m, 3.8 m and 7.6 m from the downstream toe of the levee. A local decrease of water pressure is an indication for pipe formation. During the progressive erosion phase, an increase of water pressure is measured (because of the connection of the pipe with the upstream side). Figure 3 shows two contour plots of the hydraulic gradients as measured in the sand layer during pipe formation (phase d in Figure 2) and near the end of the progressive erosion phase (phase e in Figure 2).

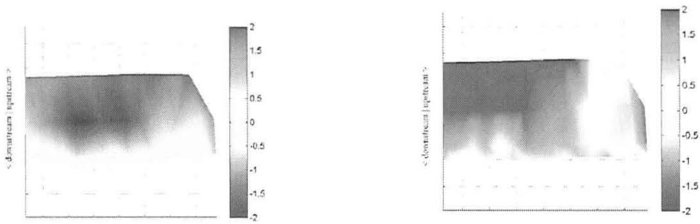

1 Oct 2009, 6:25 pm (t=54.4 hours) 3 Oct 2009, 4:00 pm (t=100 hours)

Figure 3. Contour plots of hydraulic gradients in sand layer.

Figure 4 shows the levee half an hour after collapse, which took place on October 3rd, 2009 at 4:20 pm.

Figure 4. The first IJkdijk piping test shortly after collapse.

Heated fibre optic cables

GTC Kappelmeyer has tested the leakage detection capability of fibre optic cables in conjunction with the Heat-Up (or Heat-Pulse) method (Dornstädter, 2010). The fibre optic cable was deployed both in sand and clay, parallel to the length axis of the levee. All cables were installed as single lines, except for one cable which runs in equidistant parallel loops in a mat, see Figure 5.

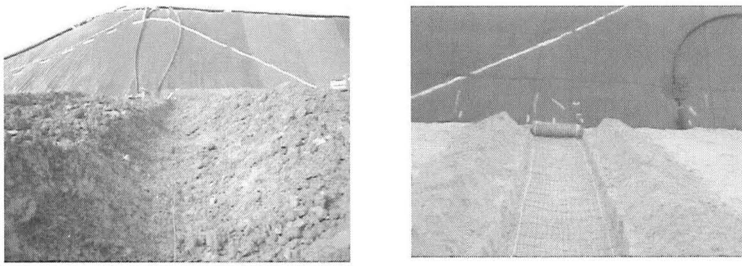

Figure 5. left: cable deployed in clay; right: mat deployed in sand.

For the Heat-Up method the fibre optic cable was heated up by sending an electrical current through the metallic cable coating (stranded steel wires). The fibre optic temperature measurements were conducted with an OTS 40P laser unit. All the instruments and the steering unit for the heating was place in a box on the crest of the dam. A mobile generator supplied the power for the heating.

Six cables were placed in the test. Three were placed at a depth of 10 cm in the sand layer, one at 1.5 m, one at 7.5 m and one at 13.5 m from the downstream toe of the levee. The other three were placed about 10 cm above the sand-clay interface, in the clay, one at 5m, one at 8.5m and one at 10m from the downstream toe.

Failure of the levee occurred at 3 October 2009, at 4:20 pm. The cables placed in the sand layer give more detailed information about the failure than the cables placed in the clay, see Figures 6 and 7. The cables show local shifts in temperature one hour before the failure of the levee occurs. The locations of these shifts (at the white and blue parts) correspond with the locations where an increase of the water pressures is measured during the progressive erosion phase (measured by the pore pressure meters, the reference monitoring).

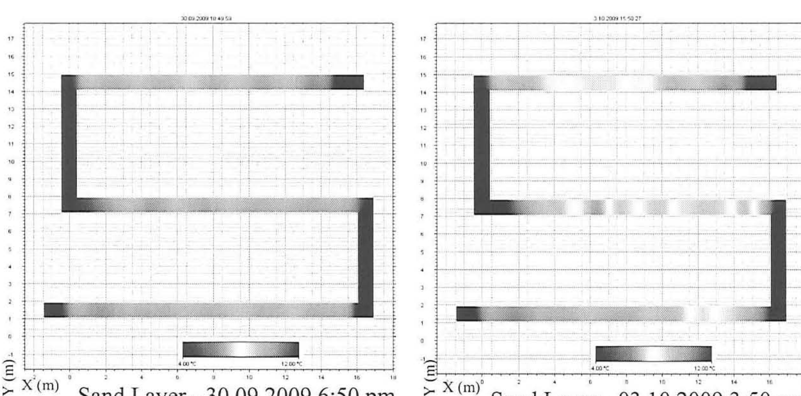

Figure 6. Test 1, results cables sand layer.

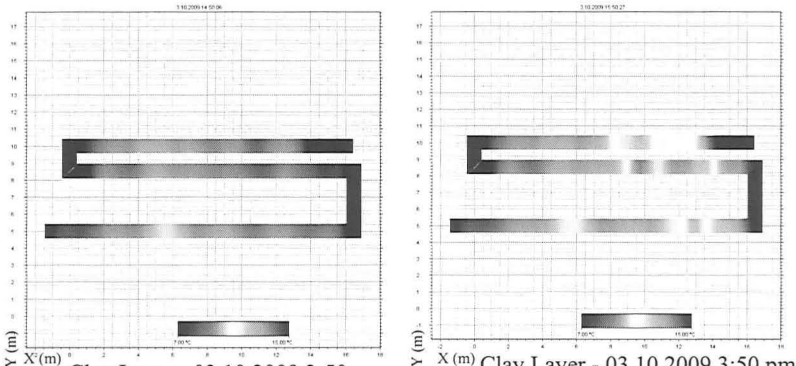

Clay Layer - 03.10.2009 2:50 pm Clay Layer - 03.10.2009 3:50 pm

Figure 7. Test 1, results cables clay layer.

Geotextile glass fibre optics

TenCate Geosynthetics, Inventec, EDF and geophyConsult have been involved in the IJkdijk Piping project to provide a monitoring solution based on optical cable and on the GeoDetect® monitoring solution (Artières, 2010).

The experiment in test 1 was to monitor the erosion process at the interface between the clayey levee and the erodible sandy subsoil. The optical cables were used without textile to avoid any perturbation. Having the geotextile in place would provide the added value of anchoring the optical cable to the soil to prevent slippage and act as a filter to delay micro-erosion's progress which may give levee owners more time to react (hence the 'little disturbing' influence of the innovative monitoring techniques in this test). One multimode optical cable was installed and connected to the instrumentation to measure a temperature profile. The optical cable was installed in the saturated sand at a depth of 10 cm below the sand surface, see Figure 8. The cable was installed parallel to the dike at six parallel lines at an increasing distance to the downstream toe, see Figure 9.

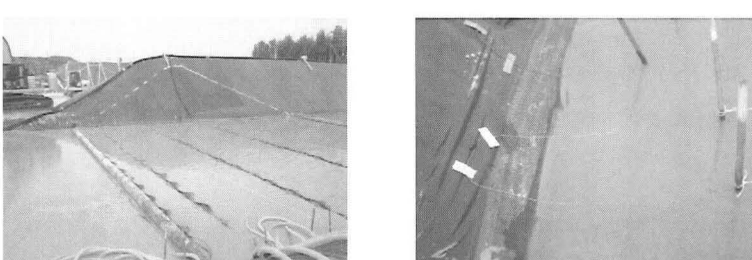

Figure 8. **Installation of the optical cable (blue) in the submerged sand layer.**

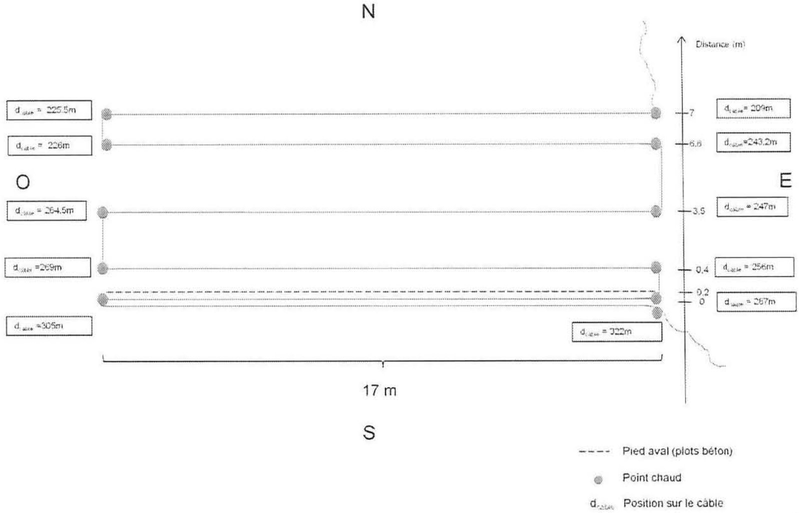

Figure 9. Test 1, Location of the six optical cables – the dotted line is the toe of the levee.

The plots of the raw temperatures measured by the optical cable indicate progressive erosion of the pipe from the upstream side to the downstream side of the dike on October 3rd, 2009 at 1:26 pm (see the green circle in Figure 10), i.e. about 4 hours before the levee failed. A post-failure analysis that is about to be included in real-time data analysis modules has revealed the presence of precursors several days before collapse (Artières et al., 2010).

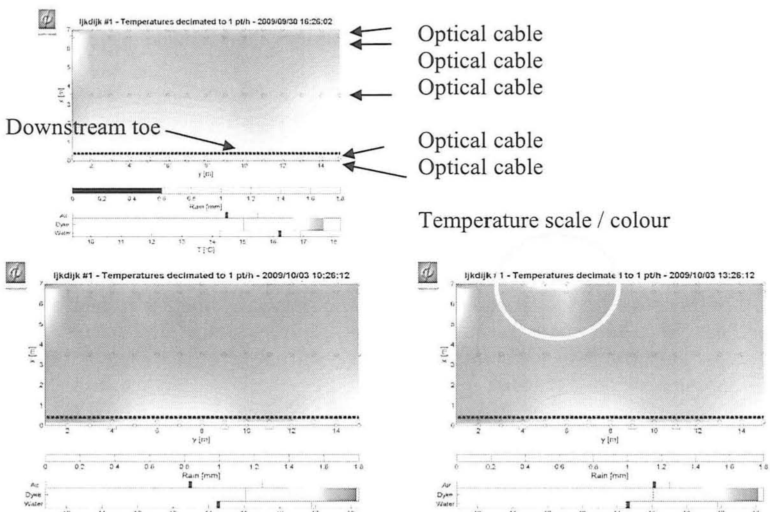

3 Oct 2009 10:26 am 3 Oct 2009 1:26 pm

Figure 10. Test 1, results of temperature measurements.

In the fourth test, a 40 cm wide GeoDetect® strip embedding optical cables both for temperature and strain measurement was buried at 10 cm depth in dry sand well before the test in the three lines the nearest to the downstream toe, while in the other three locations only temperature was measured. Figure 11 shows some results from this other test. In test 4, failure took place at 5 December 2009, at 2:25 pm.

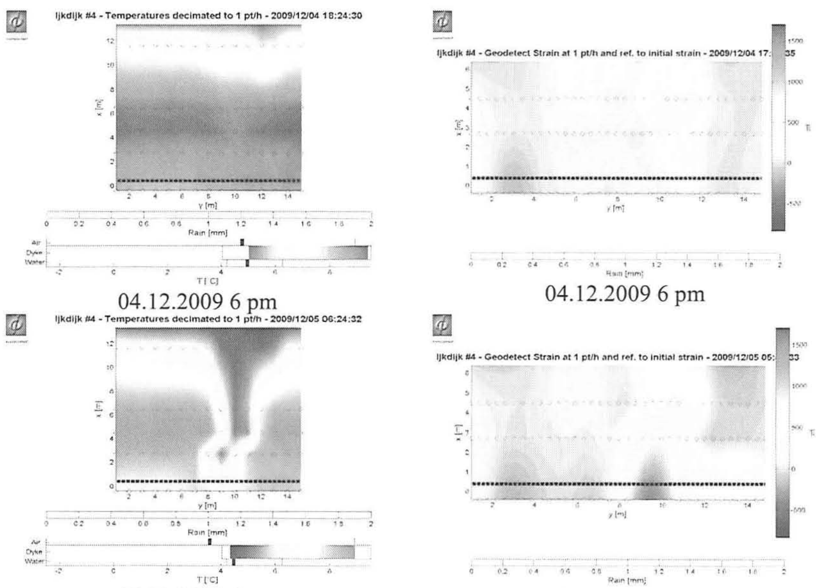

04.12.2009 6 pm 04.12.2009 6 pm

05.12.2009 6 am 05.12.2009 6 am

Figure 11. Test 4, results of temperature (left) and strain (right) measurements.

The upper right plot indicates a pipe right to the middle already on the afternoon before failure. The intermediate effects of the progressive failure process on the temperature below the levee early in the next morning is clearly shown in the lower left plot. The strain measurements give complementary information, even though they are less sensitive in this case as the geotextile fiber optic sensors were not placed close to failure zone for experimental reasons.

CONCLUSIONS

The process of piping is studied in full-scale tests at IJkdijk experiment site in Booneschans. The use of pore pressure meters as an early warning system for piping in levees is demonstrated. Water pressure measurements give an indication of the phase of piping attained in the test.

Temperature measurements turn out to be effective for detecting signs of failure by piping, especially the progressive erosion phase is easily detected this way. As expected, the closer the optical fibers are located to the leaks, the better the predictions are, both for temperature and strain measurements. The cables placed in the sand layer give more detailed information about the failure than the cables placed in the clay because of the permeability of the sand layer.

The results presented here show that temperature measurements near the top of a sand layer sensitive to underseepage erosion can be quite effective for the early detection of progressive erosion. Combined with the fact that such measurements may be performed at much lower costs than pore pressure measurements, this may become an efficient detection method in flood safety programs, especially if local last-minute measures can be taken to avoid failure of the levee.

REFERENCES

Artières, O. (2010). "IJkdijk Piping experimentation – Report of the measurements made with the TenCate GeoDetect® system and separate optical fibers on the tests 1, 2, 3 and 4" Ten Cate / Inventec / EDF / geophyConsult, Paris.

Artières O., Beck Y.L., Khan A.A., Cunat P., Fry J.J., Guidoux C., Pinettes P. (2010). "Thermal and stability monitoring of earthdams with a fiber-optics based monitoring system", *Proc. 2nd Int. Conf. on Dam Maintenance & Rehabilitation*, Zaragoza, Spain, 28-30 September 2010.

Beek, V. van and Knoeff, H. (2009). "SBW Piping: Hervalidatie piping, HP5.5 Analyse en validatie full-scale proeven", *Report no. 1200690-005-GEO-0006*, Deltares, Delft.

Beek, V.M. van, Bruijn, H.T.J. de, Knoeff, J.G., Bezuijen, A. and Förster, U. (2010). "Levee failure due to piping: A full-scale experiment", *Proc. 5th Intl. Conference on Scour and Erosion*, San Fransisco (CD-ROM), ASCE, Reston, VA.

Bligh, W.G. (1910). "Dams, barrages and weirs on porous foundations", *Engineering News*, 64(26):708-710.

Dornstädter, J. (2010). "IJkdijk - Experiment 1 and 4 - Fibre Optic Leakage Detection System Using the Heat-up Method", *Final report*, GTC Kappelmeyer, Karlsruhe.

Havinga, F.J. and Kok, M. (2005). "Flood Risks and Safety in the Netherlands (Floris)", Ministry of Public Works, Delft. ISBN 90-369-5604-9.

Koelewijn, A. (2009). "New Measurement Technology for Dike Monitoring", *Deltares GeoAcademy Course on Geotechnical Instrumentation for Field Monitoring*, 21-23 April 2009, session S, Deltares, Delft..

Sellmeijer, J.B. (1988). "On the mechanism of piping under impervious structures", *PhD Thesis*, Delft University of Technology, 56 p.

Analysis of the Temporal Evolution of the Sediment Movement in the Vicinity of a Cylindrical Bridge Pier

Florian Pfleger[1], Christoph Rapp[2], Michael Manhart[3]

[1] Dipl.-Ing., Fachgebiet Hydromechanik, Technische Universität München, Arcisstr. 21, 80333 München, Germany, f.pfleger@bv.tum.de, +49/89/28922419
[2] Dr.-Ing., Fachgebiet Hydromechanik, Technische Universität München, Arcisstr. 21, 80333 München, Germany, ch.rapp@bv.tum.de
[3] Prof. Dr.-Ing. habil., Fachgebiet Hydromechanik, Technische Universität München, Arcisstr. 21, 80333 München, Germany, m.manhart@bv.tum.de

ABSTRACT: A detailed analysis of the sediment movement in the vicinity of a cylindrical pier is presented. The experiments were conducted in a laboratory flume. The movement of the sediment grains was detected and evaluated by image processing techniques at several stages of the scouring process. The pictures of the sediment surface were captured with a CMOS-camera from above through a plexiglass plate which was slightly submerged on the water surface. 20% of the sediment grains were colored black to assure a significant contrast. The experiments were conducted for 20 h at 80% of the critical section averaged velocity. The results of the study comprise time-averaged moving directions and magnitudes, scatterplots of the displacement events and transport intensities at a high spatial resolution for all scouring stages. The temporal evolution of the main scouring agents (tangential velocity components and the horseshoe-vortex system) and their importance during the particular stages were evaluated. The development of the grain velocity magnitudes, the dispersion of movement events and the transport intensities are discussed.

INTRODUCTION

Despite a notable amount of scientific investigations on scouring around cylindrical piers the prediction of the maximum scour depth and the temporal evolution of the scour hole is still not possible with a satisfying reliability. Most of the scour formula available are based on experimental laboratory investigations of the scour depth evolution. Due to the specific conditions of these different experiments their field of application is limited. This fact leads to significant deviations of the predicted scour depth and temporal evolution in comparative calculations (Link (2006)). For the development of a more universal approach for the prediction of scour at bridge constructions further detailed investigations of the flow field and the related erosion processes are necessary. Additionally a great demand arises for these experimental studies to improve and validate numerical models for the simulation of scouring processes.

Many investigations on the main influencing factors of the scour hole development (flow field, erosion processes, scour hole geometry) can be found in the literature. Hjorth (1975) studied the flow field and the bed shear stress at the initial stage (flat bed), Melville (1975) and Melville and Raudkivi (1977) measured velocities near the bed and in radial planes and described the erosion processes for initial, intermediate and equilibrium scour holes. Zanke (1982) also gave a detailed description of the erosion processes and their evolution in time. Dargahi (1990) analysed the horseshoe vortex system (HV-system) at the pier front and related his findings to the development of the scour hole geometry. Dey and Raikar (2007) measured the flow field in radial planes with an ADV-probe for several evolution stages respectively and analysed the HV-system. Unger and Hager (2007) conducted PIV measurements in several vertical and horizontal planes around a half-cylinder mounted at the side wall of a flume and analysed the HV characteristics.

During the last years several researchers designed image processing based methods for the measurement of sediment movement in laboratory flumes. Pilotti et al. (1997), Sechet and LeGuennec (1999), Keshavarzy and Ball (1999) and Papanicolaou et al. (1999) recorded image series of particles moving along the flume bottom in uniform open channel flow and processed them manually or automatically. Radice et al. (2008) applied image processing techniques to map the sediment movement in the vicinity of abutments.

In this work the kinematics of the sediment erosion processes in the vicinity of a cylindrical bridge pier are analysed. The grain movements were mapped in image series and analysed via digital image processing techniques. Eight different stages of the scour evolution (after $5, 30, 60, 120, 240, 480, 720$ and 1200 min) were analysed and the qualitative results of the above mentioned literature were compared to these findings.

EXPERIMENTAL SETUP

In the following the experimental setup is presented. A more detailed description can be found in Pfleger et al. (2010).

Flume

The experiments were conducted in the Hydromechanics Laboratory of the Technische Universität München. 16 m downstream of the inlet of a 1.20 m wide flume a cylindrical pier ($D = 0.10$ m) was embedded in the center of the flume in a 0.30 m deep sand bed. 6.5 m upstream of the cylinder the bottom was elevated and covered with a sediment layer. Two flow straighteners of different mesh size were placed in the approach flow.

Sediment

Uniform natural coarse sand with a representative diameter $d_{50} = 1.9$ mm was used. The angle of repose was measured to be 30°. 20% of the grains were colored black to ensure a significant contrast for the image processing.

Hydraulic conditions

The presented experiment was conducted at a flow depth of 0.15 m and a section averaged flow velocity of 0.365 m/s. This corresponds to 80% of the critical section averaged flow velocity at a flow depth of 0.15 m. The Reynolds number based on the pier diameter is $\mathrm{Re} = 32000$.

Measurement setup

The image series of the sediment surface were captured from vertically above in two camera positions by a black and white CMOS-camera at 0.63 Mpx and a frame rate of 27 fps. The pixel to grain ratio was found to be $0.145d_{50}$. A plexiglass plate was slightly submerged on the water surface to provide a defined optical access to the sediment surface. The measurement area was lightened continuously by two spotlights from above and an additional light source inside the cylinder. The setup is sketched in Figure 1.

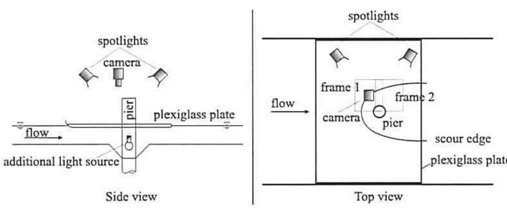

Figure 1: Measurement setup

IMAGE PROCESSING

The images captured in this setup were analysed by digital image processing techniques. The basic principles are presented in the following section. A detailed description can be found in Pfleger et al. (2010).

Image processing and evaluation algorithm

Parts of the methods introduced by Papanicolaou et al. (1999) and Radice et al. (2008) were adopted to develop a new algorithm which suits the conditions of the pier scour experiment best.

The image processing is based on the subtraction of the intensity matrices of consecutive frames and the evaluation of non-zero spots in the resulting difference images. To avoid problems with moving uncoloured sediment grains which only have a minor contrast to their background only the movement of black colored grains is detected. In most cases they have a significant contrast to the background except moving above other black grains.

The images are first top-hat filtered to eliminate all non-black pixels and afterwards difference images are produced such that moving black grains appear in the first difference frame in the original position and in the second in their new position. After applying a median filter the non-black pixel groups (the former black grains) are defined to be grains if they meet a certain size criterion. For the grains in the first difference image corresponding grains in the second image are determined via a correlation coefficient. Therefore a maximum movement radius is defined and for grains within this radius the correlation coefficient composed of the gray scale similarity, the deviation from the most probable movement direction in this area (out of a first iteration step) and the exclusion of white grains moving over black background is calculated for each of these grains (Pfleger et al. (2010)). The grain pair with the highest correlation coefficient leads to the calculation of displacement and velocity.

Perspective calibration

Due to the three dimensional scour hole surface a perspective calibration of the images is necessary. Therefore geometry measurements of the sediment surface at the investigated stages of the scouring process were made. For each stage an experiment was done for the corresponding time and the geometry was mapped by a laser distance sensor. The topography data are used to conduct a coordinate transformation to determine the real positions that are represented by each pixel.

Postprocessing

Since only the black grains are detected and the movement intensities in some scour regions are very low, the number of detected displacements in some areas is not high enough to yield sufficient statistics. Thus a spatial median filter is applied to the averaged vector fields. In Pfleger et al. (2010) it is shown that the filter is smoothing the field and not changing the tendencies of the raw pattern.

RESULTS

The sediment movement patterns of the above described scour experiment were analysed for eight scouring stages (after 5, 30, 60, 120, 240, 480, 720 and 1200 min). 40,000 to 50,000 frames per stage were recorded since only the displacements of the black grains were detected and in some areas of the scour hole the movement intensity is very low. Since at most about 10,000 frames (recording time about 6 min) can be captured without a considerable change in scour geometry the experiment was run several times to get a satisfying amount of samples.

The temporal evolution of the scour depth shows the typical logarithmic shape. After 1200 min the deepening rate is lower than one grain diameter per hour and therefore quasi-equilibrium is considered to be reached (Link et al. (2006)).

In Figure 2 the vicinity of the pier is divided in hydrodynamically reasonable sections for a better understanding of the following explanations.

As described in the previous section the measurement system assumes that no suspended transport occurs since all detected movements are projected to the sediment surface. For the transport situation of this experiment the assumption is right for all regions of the scour hole except a small area directly at the backside of the pier (6.1 and the neighboring part of 7).

In general all velocities mentioned in the following section are grain velocities.

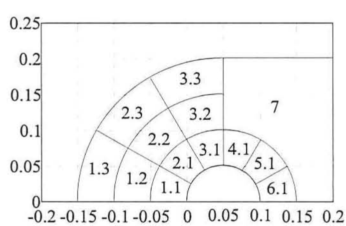

Figure 2: Definition of regions in the pier vicinity

Mean grain velocity fields

The mean grain velocities and movement directions were investigated in squared interrogation areas with a length of 0.01 m. In Figure 3 the kinematic patterns of all stages are presented. The background by color represents the ratio of the radial to the tangential component of the grain velocity field with respect to the cylinder axis. Dark gray stands for movement radially inwards, white radially outwards and areas with tangential or no movement are colored as shown in the center of the colormap in Figure 3.

After 5 min the pattern is dominated by tangential components. Directly at the pier bottom a circular region (1.1-5.1) with high grain velocities can be depicted. Especially in this area almost no radial component appears. Very close to the stagnation plane upstream the cylinder a small area of displacements directed outwards can be seen. This pattern matches with the velocity and bed shear stress fields measured by Hjorth (1975) and Melville (1975) and observations described by Zanke (1982) and Dargahi (1990). The main scouring agent during the initial stage is the accelerated flow at the pier sides. The HV-system is present but weak. The footprint of its rotation can be seen at the pier front but at the pier sides the vortex system is almost eliminated by the tangential flow. This corresponds to the PIV-measurements of Unger and Hager (2007) who showed that the downflow at the pier front is initially mainly deflected in the tangential direction. Outside of this inner ring (everywhere but 1.1-5.1) the grains move mainly in the streamwise direction.

The characteristics of the movements have not changed after 30 min. Upstream the pier the radial components in the inner ring (1.1) become slightly more dominant due to the growth of the HV-system when the scour gets deeper (Melville (1975), Zanke (1982), Dargahi (1990)). Additionally further outside (1.2, 2.2, 3.2) the grains begin to slide down the scour slope. Thus the component pointing radially inwards grows.

The results after 60 and 120 min do not differ significantly. The structure of a slowly growing and strengthening HV-system, tangential transport at the pier sides (2.1, 3.1, 4.1, 5.1) and sliding movements along the upper scour slope (1.2, 2.2, 3.2) are still observable. Especially after 120 min the magnitude of the tangential vectors at the sides decreases.

For the vector fields after 240, 480, 720 and 1200 min a general tendency is noticeable. In the sections 1.2, 2.2, 3.2, 1.3, 2.3 and 3.3 avalanches occur. Below this area (1.1, 2.1, 3.1) the influence of the HV-system is constantly growing. The contours in Figure 3 show a white area representing the impact of the HV-system on the erosion process. While the scour deepens this ring expands downstream and in radial direction. Near the stagnation plane the ring reaches the pier front, corresponding to the vortex structure e.g. measured by Dey and Raikar (2007) or Unger and Hager (2007). Following the pier side downstream after 240 and 480 min an area of tangential movement is present where the influence of the tangentially deflected downflow is evident (2.1, 3.1, 4.1, 5.1). This tangential movement decreases during the further process. The effective range of the HV-system expands towards the pier in the upstream half of the scour (1.1, 2.1, 3.1). This corresponds to the vortex size evolution measurements by Muzzammil and Gangadhariah (2003). The influence of the accelerated tangential flow components decreases.

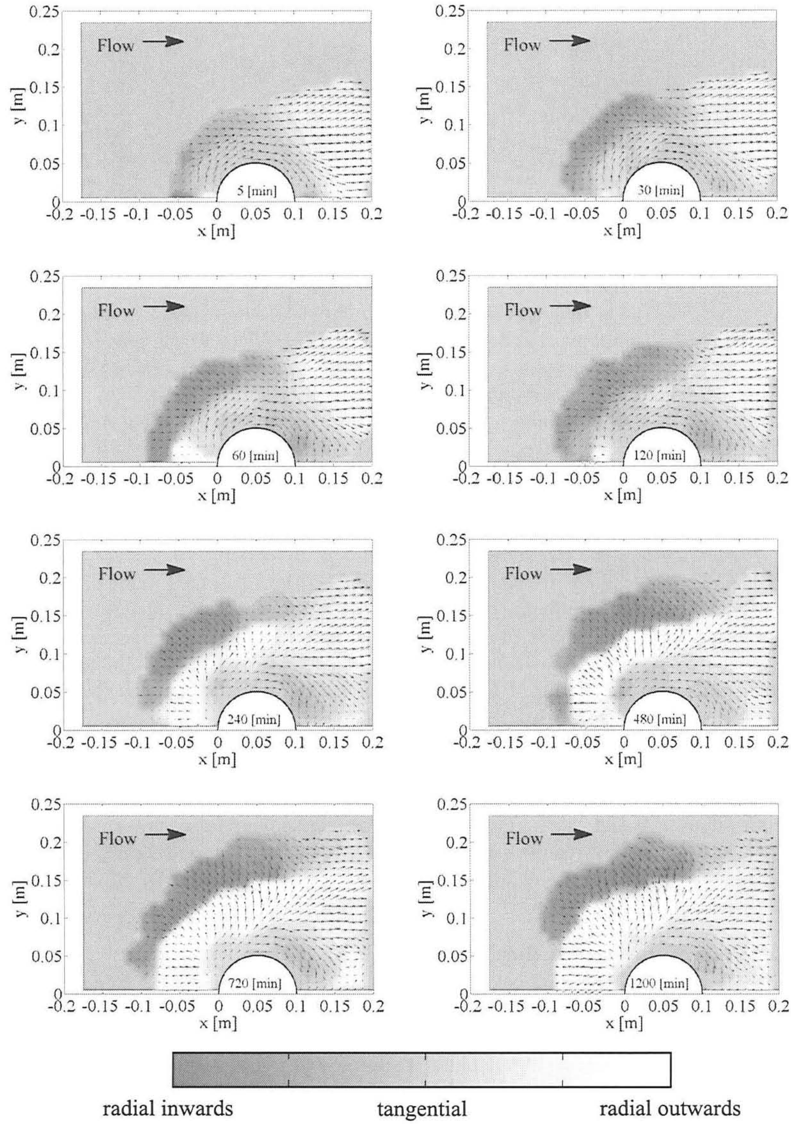

Figure 3: Mean grain velocity vector field with contour of the ratio of radial to tangential components

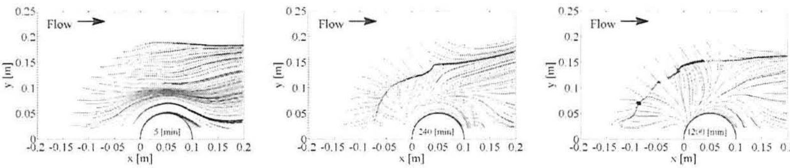

Figure 4: Streamlines of sediment movement after 5, 240 and 1200 min

In the downstream half of the scour hole initially sediment is deposited and forms a small hill (7). At the outer side of this hill streamwise movement is superposed by a slight sliding component directed down the hillside. Close to the pier (5.1, 6.1) for all scouring stages the erosive effect of a small detachment zone (non uniform movement directions) can be observed.

In Figure 4 the streamline plots of the sediment movement after 5, 240 and 1200 min are shown. The patterns agree very well with the mean near-bed velocity directions shown in Melville (1975) for the initial, the intermediate and the equilibrium scour hole respectively. The change of the main erosion directions in between these three stages is evident. This reveals the processes described before.

Figure 5 shows the magnitude of the mean grain velocity vectors after 5, 240 and 1200 min. The values are normalized by the section averaged velocity of the channel flow *u_bulk*. After 5 min the highest values appear at the upstream facing cylinder sides (2.1, 3.1) where the scouring process starts and downstream of the cylinder where the grains are transported off the scour hole (7). The mean grain velocities are lower than 30% of the approaching flow velocity even in the initial stage . The grain velocities in the later stages are in general lower than at the beginning. This is especially essential in the upstream half where the transport is now dominated by the HV-system and avalanches in the upper slope. In this part a ring with very low mean grain velocities appears approximately in the middle of the scour slope (1.2, 2.2, 3.2). This is where the two phenomena converge and an unstable rim is formed (Melville and Raudkivi (1977)). During the scouring process the velocities downstream the cylinder where the grains are transported off the scour hole (7) decrease significantly.

Scatterplots of movement directions

Since the averaged grain velocity values do not fully represent the dynamics of the erosion process scatterplots of the two cartesian velocity components are shown for every second interrogation area in Figure 6. Each point corresponds to one measured combination of grain velocity components in the x- and y-direction within this area. The scour hole is shown after 5 and 240 min. As described for the mean value plots the properties of the intermediate and the equilibrium scour hole are very similar.

In the initial stage the point clouds in the high velocity area at the upstream facing pier sides (1.1, 2.1, 3.1) are relatively compact. In the section 1.2, 2.2 and 3.2 the data points are distributed across a wider area in many directions. This could be referred to an already established small detachment zone along the scour edge.

Close to the stagnation plane the influence of the growing HV-system scatters the points significantly. In the detachment zone in the wake of the pier (5.1, 6.1) the grain movements fill all quadrants of the scatterplots equally. In section 7 where the movement direction is comparatively straight out of the scour the allocation of the displacement events is uniform.

After 240 min the influence of the HV-system can be distinguished (1.1-3.1, 1.2-3.2). Even if there are quite distinct mean movement directions in this area the displacements are spread over a wide range. This refers to the uphill transport by the HV and the temporary collapsing rim. Additionally the highly turbulent nature of the HV-system leads to spatially and temporarily fluctuating transport events. In the downstream half of the scour the data points are again less scattered (7). Here the less fluctuating accelerated flow components dominate the erosion process.

Transport intensities

In Figure 7 the transport intensities are represented by the number of displaced grains per second and square centimetre.

After 5 min in the upstream part a concentrically shaped area with high transport intensities is evident (2.1-4.1). Here also relatively high grain velocity magnitudes appear which lead to an effective transport. Inside this ring close to the pier the number of moving grains is significantly lower. The grain velocities are comparable but the tangentially accelerated flow as the main scouring agent reaches the scour bottom not constantly. An explanation for this is that the already weakly acting HV-system pushes the effective flow components temporarily away from the pier sides. In the downstream part high but not effective transport intensities in the detachment zone (5.1, 6.1) and considerably smaller but uniform transport events in section 7 can be observed.

For the intermediate and the equilibrium scour hole the HV-system causes high intensities in its effective range (1.2-3.2). In contrast to the equilibrium stage after 240 min many grains are also displaced in the sections 5.1 and 6.1 pointing to a detached flow. This matches with the velocity measurement in horizontal planes by Unger and Hager (2007) who state that inside a developed scour hole the flow does not detach from the cylinder. In general the transport intensities after 1200 min tend to zero.

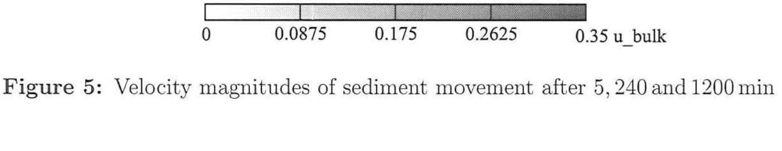

Figure 5: Velocity magnitudes of sediment movement after 5, 240 and 1200 min

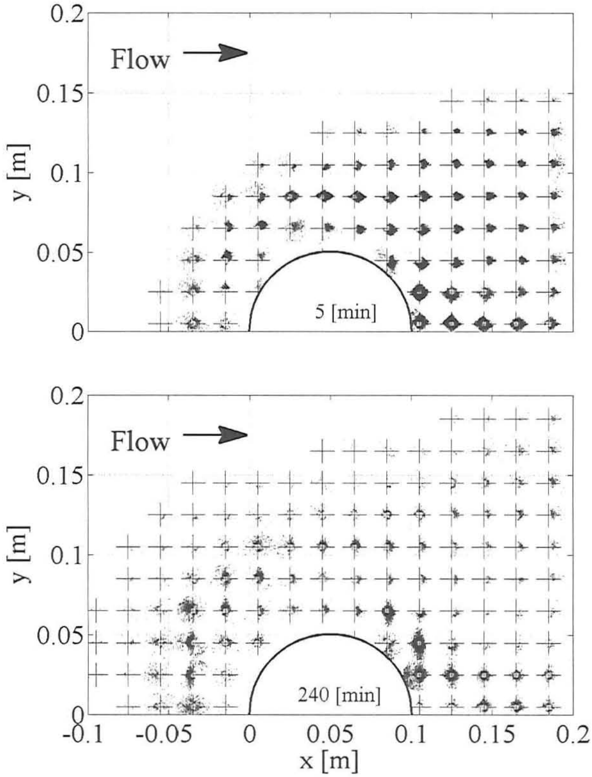

Figure 6: Scatterplots of instantaneous movement events after 5 and 240 min

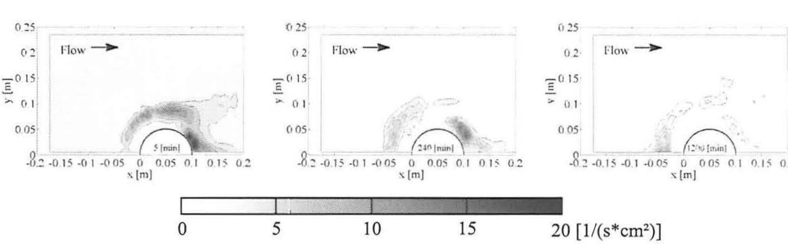

Figure 7: Number of displaced grains $[1/(s \cdot cm^2)]$ after 5, 240 and 1200 min

CONCLUSION AND OUTLOOK

The initial scour hole formation is mainly caused by tangentially accelerated flow components. This results in relatively uniform movement directions at the pier sides and in the downstream part at comparably high mean grain velocities. The combination of mainly downstream directed grain movements and high erosion rates leads to a rapid scour growth. In the growing scour the influence of the HV-system on the erosion is increased. The caused movements are a combination of uphill transport by the HV and avalanches due to temporarily collapses of the scour slope. Thereby a rim is established in the middle of the slope. The contribution of these displacements to the mass transport off the scour is small since the two described transport effects have almost opposite directions. In the regions where the effective transport out of the scour takes place the intensities and grain velocity magnitudes are decreasing. This combination leads to the deceleration of the scouring process.

In a continuative work near wall LDA measurements in the scour region will be conducted. In a fixed scour hole geometry mean velocities and turbulence intensities will be measured and combined with the results of this study to gain more detailed dependencies between flow field and sediment transport within a scour hole.

REFERENCES

Dargahi, B. (1990). "Controlling mechanism of local scouring." *Journal of Hydraulic Engineering*, 116(10), 1197–1214.

Dey, S. and Raikar, R. (2007). "Characteristics of horseshoe vortex in developing scour holes at piers." *Journal of Hydraulic Engineering*, 133(4), 399–413.

Hjorth, P. (1975). "Studies on the nature of local scour," PhD thesis, University of Lund.

Keshavarzy, A. and Ball, J. (1999). "An application of image processing in the study of sediment motion." *Journal of Hydraulic Research*, 37(4), 559–576.

Link, O. (2006). "Untersuchung der Kolkung an einem schlanken zylindrischen Pfeiler in sandigem Boden," PhD thesis, Technische Universität Darmstadt.

Link, O., Pfleger, F., and Zanke, U. (2006). "Automatic non-intrusive measurement of scour-hole geometry." *Proceedings to ICSE3*, H. Verheij and G. Hoffmans, eds., 3rd International Conference on Scour and Erosion, Gouda, The Netherlands. CURNET, 403–408.

Melville, B. W. (1975). "Local scour at bridge sites," PhD thesis, University of Auckland.

Melville, B. W. and Raudkivi, A. (1977). "Flow characteristics in local scour at bridge piers." *Journal of Hydraulic Research*, 15(4), 373–380.

Muzzammil, M. and Gangadhariah, T. (2003). "The mean characteristics of horseshoe vortex at a cylindrical pier." *Journal of Hydraulic Research*, 41(3), 285–297.

Papanicolaou, A. N., Diplas, P., Balakrishnan, M., and Dancey, C. L. (1999). "Computer vision technique for tracking bed load movement." *Journal of Computation in Civil Engineering*, 71–79.

Pfleger, F., Rapp, C., and Manhart, M. (2010). "Experimental investigation on the sediment movement in the vicinity of a cylindrical bridge pier." *Proceedings to Riverflow conference 2010*. Accepted for publication.

Pilotti, M., Menduni, G., and Castelli, E. (1997). "Monitoring the inception of sediment transport by image processing techniques." *Experiments in Fluids*, 23, 202–208.

Radice, A., Malavasi, S., and Ballio, F. (2008). "Sediment kinematics in abutment scour." *Journal of Hydraulic Engineering*, 134(2), 146–156.

Sechet, P. and LeGuennec, B. (1999). "Bursting phenomenon and incipient motion of solid particles in bed-load transport." *Journal of Hydraulic Research*, 37(5), 683–696.

Unger, J. and Hager, W. (2007). "Down-flow and horseshoe vortex characteristics of sediment embedded bridge piers." *Exp Fluids*, 42, 1–19.

Zanke, U. (1982). "Kolke am Pfeiler in richtungskonstanter Strömung und unter Welleneinfluss." *Mitteilungen des Franzius-Instituts für Wasserbau- und Küsteningenieurwesen der Universität Hannover*, 54, 381–416.

Time Evolution of the Horseshoe Vortex System Forming Around a Bridge Abutment

Mete Koken, and Mustafa Gogus

Civil Engineering Department
Middle East Technical University; Ankara
Turkey; email: mkoken@metu.edu.tr

ABSTRACT

Scour forming around an isolated bridge abutment with curved end is investigated in this study. Clear water scour experiments are conducted for an abutment in a 25 m long sediment flume at a Reynolds number of 45000. 3D scour patterns forming around the abutments are obtained using an array of acoustic transducers along a grid refined up to 1-2 cm spacing at different stages of the scour. Detached Eddy Simulation (DES) is performed at the same channel Reynolds number for flat bed case (initiation of the scour) and for two deformed bed cases (intermediate stages of scour). Incoming flow in the simulations were fully turbulent containing unsteady velocity fluctuations. Variations in the structure and intensity of the horseshoe vortex system are investigated. At the initial stage of the scour the main and secondary horseshoe vortices undergo aperiodic bimodal oscillations. Those oscillations cause the horseshoe vortices to induce large bed shear stress values beneath them. As the scour hole starts forming secondary necklace vortex, HV2, gets closer to the primary necklace vortex, HV1, and merges with it at a location close to the abutment tip.

INTRODUCTION

Bridge abutments cause a very complex 3D flow field to occur within its proximity. The incoming boundary layer separates as the abutment is approached in the presence of the adverse pressure gradients. As a result of this separation, necklace shaped vortical structures (so called horseshoe vortex system) form around base of the abutment. When the abutment lies on top of an erodible bed material, the horseshoe vortex (HV) system plays an important role in the evolution of the scour hole around this structure.

Although there are many studies that tried to predict the scouring pattern and maximum scour depth for different hydraulic conditions and shapes of the structure (for a review see Melville, 1997), less effort has been made to understand the intricate flow physics behind the local scouring process and, in particular, the role played by the large-scale coherent structures present around the bridge abutments.

The turbulent horseshoe vortex system that forms around the bridge abutment is unsteady as its size, intensity and location changes with time. HV system is responsible for the increase in the turbulent kinetic energy and pressure r.m.s. fluctuations around its core locations along its trajectory. Furthermore HV system induces large bed shear stress and pressure r.m.s. fluctuations on the bed.

Koken and Constantinescu (2008a, 2008b) provided the first in-depth study of the structure and the unsteady dynamics of the flow field forming around vertical wall abutments both for flat bed and deformed bed conditions. They used a well resolved Large Eddy Simulation (LES) to simulate the flow field around the vertical wall abutment at a Reynolds number of 18,000 for both flat bed and deformed bed conditions. Flat bed conditions corresponded to the initiation of the scouring process and the deformed bed conditions represented the equilibrium scour conditions.

Although the initial and final stages of the scour are investigated in their study Koken and Constantinescu (2008a, 2008b) did not consider the intermediate stages. It is not clear how the coherent structures forming around the abutment changes throughout the scouring process. In the present study for a selected abutment length, the coherent structures, (especially the HV system) forming around the abutment are investigated at initial and two intermediate stages of the scour using DES.

EXPERIMENTAL SETUP

Experiments used in this study are performed in a 25 m long laboratory sediment flume which has width and height of 1.5 m and 0.5 m, respectively. Sand particles with a median size of d_{50} = 1.5 mm was used in the experiments. Sediment compartment of the channel, which is 6 m long, was filled with this material. These particles were also stuck on the channel surface to maintain uniform roughness. An abutment which has a 10 cm diameter semi-circular end was attached to one of the sidewalls within the sediment compartment section of the channel. The total length of the abutment including the semi-circular end was 15 cm. Mean approach velocity, U, and the flow depth, D, are selected as 0.335 m/s and 0.135 m, respectively, to ensure clear water scour conditions within the channel. The channel Reynolds number obtained using the mean approach velocity and flow depth was around 45,000. Experiment was started and run for 2 hours. Then 3D scour patterns forming around the abutment were measured using an array of acoustic transducers along a grid refined up to 1-2 cm spacing. After this, experiment was run for another 2 hours which continued with the similar bathymetric measurements. Obtained bathymetric data together with the typical scour and deposition dimensions are given for both scour stages in Figure-1.

NUMERICAL MODEL

Detached Eddy Simulation is used to simulate the flow forming around the isolated bridge abutment which was described above. No wall functions are used in the simulations. The code uses fractional step method to integrate 3-D incompressible Navier-Stokes equations. Generalized curvilinear coordinates are used on non-staggered grid. Convective terms in the momentum equations are discretized using a blend of fifth-order accurate upwind biased scheme and second-order central scheme. All other terms in the momentum and pressure-Poisson equations are approximated using second-order central differences. The discrete momentum (predictor step) and turbulence model equations are integrated in pseudo-time using alternate direction implicit (ADI) approximate factorization scheme. In the present DES simulation, the Spalart-Allmaras (SA) one-equation model was used. Time integration in the DES code is done using a double time-stepping algorithm and local time stepping is used to accelerate the convergence at each physical time step. The time discretization is second order accurate. A general description of the code used in this study is given by Constantinescu and Squires (2004).

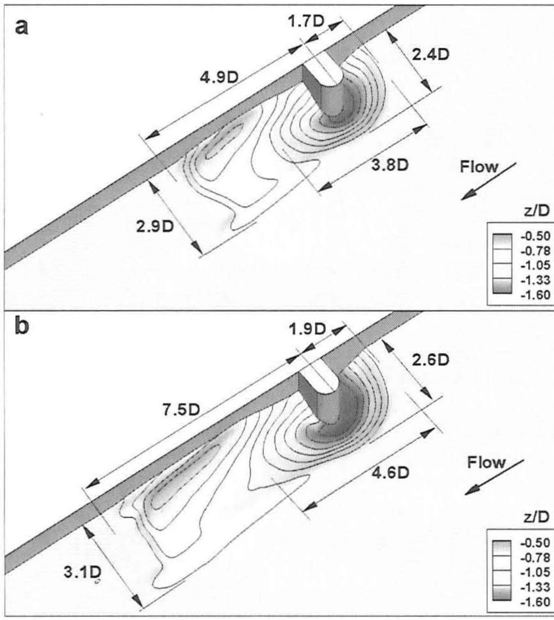

Figure-1: Scour and deposition pattern around the abutment obtained experimentally after: a) 2 hours (stage-1); b) 4 hours (stage-2).

All the parameters are normalized using the mean approach velocity U, and flow depth D for the simulations. One flat bed (initiation of scour) and two deformed bed (intermediate stages of scour) simulations are conducted for the same abutment. The bathymetry data obtained from the experiments are used in the latter two simulations. Simulation performed at two hour scour conditions will be called as stage-1 and the one performed at four hour scour conditions will be called as stage-2 throughout the rest of the text. For all three simulations, total length of the domain was 38D where the abutment was placed at 8D distance from the inlet section. Consistent with the experimental model, flow domain had a width of 11.11D. Abutment has a width of 0.74D and a length of 1.11D including the semi-circular end. The domain is meshed using more than 4 million computational nodes. Non-dimensional grid spacing along all the solid boundaries in the wall normal direction was $\Delta y^+ = yu_\tau/\nu \sim 1$ wall units (assuming that $u_\tau/U = 0.04$, see Figure-2). At the inlet section a fully developed velocity profile which contained turbulent fluctuations are introduced in a time accurate fashion. This data is previously obtained from another

Large Eddy Simulation performed at the same Reynolds number in a periodic straight channel and stored in a file. A convective boundary condition is used at the outlet which allowed the turbulent structures to leave the domain in a time accurate fashion without producing unphysical oscillations. Free surface is treated as a rigid lid. This is a reasonable assumption since the Froude number is ~0.29 within the experiments.

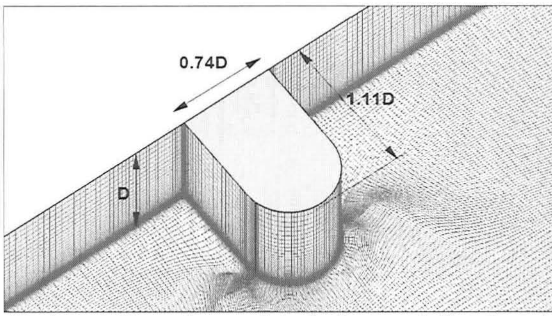

Figure-2: Abutment dimensions and typical computational mesh around it.

RESULTS

Horseshoe Vortex System

Coherent structures at the upstream of the abutment together with the horseshoe vortex system that wraps around the abutment are visualized using Q-criterion in Figure 3 for flat bed conditions and at two different scour stages (note that separated shear layers are covered in this figure). At the initiation of the scour (see Figure-3a) there are three horseshoe vortices which wrap around the base of the abutment together with a vertically oriented corner vortex, CV1, at the upstream recirculation region. Similar to the findings of Koken and Constantinescu (2008a), this corner vortex originates at the free surface and bends in the lateral direction as the bed is approached, where it merges with HV1. As a result it convects additional fluid and momentum from the regions close to the free surface into the core of HV1.

Main horseshoe vortex, HV1, originates close to the lateral wall and follows the upstream abutment face until the tip of the abutment where it bends in the flow direction. Past the abutment this vortex rapidly diffuses within the flow filed. On the other hand, secondary horseshoe vortex HV2 is larger in size and it is more coherent compared to HV1 and HV3. In the flow direction HV2 preserves its coherence up to a distance of 17D away from the abutment axis.

At scour stage-1, with the formation of the scour hole around the abutment, not only new coherent structures are observed around the abutment but also new interactions arise among these vortices (see Figure-3b). At this stage a secondary corner vortex CV2 is observed as well as the main corner vortex CV1 inside the upstream recirculation region. CV2 is located at the upstream of the main corner vortex, CV1, and is smaller in size compared to it. CV1 continues to feed the main necklace vortex HV1, whereas the secondary corner vortex CV2 feeds HV2 in a similar manner.

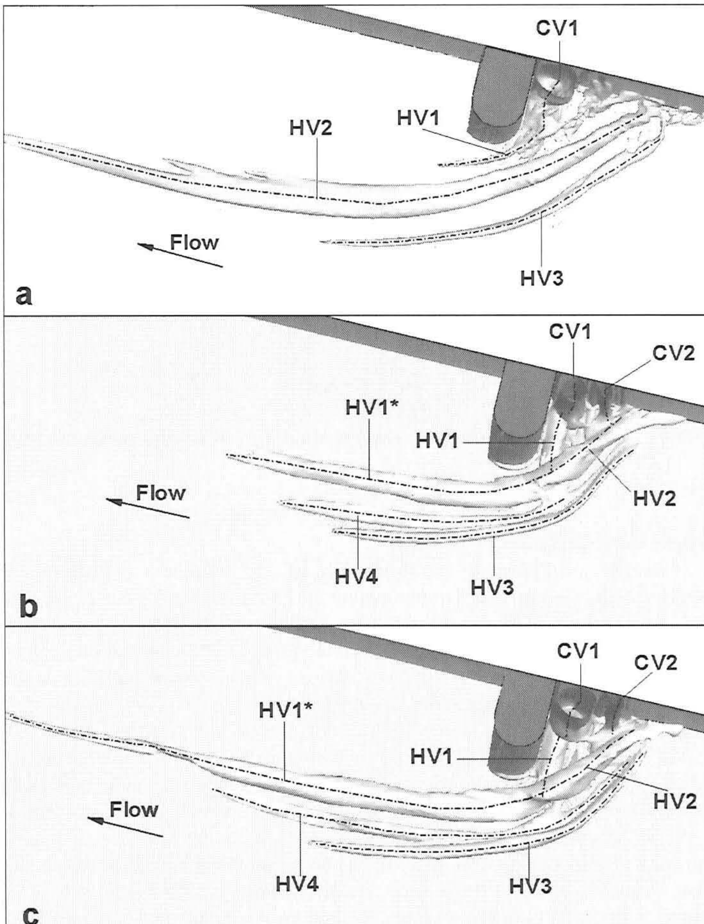

Figure-3: Vortical structures around the abutment for the mean flow (DES) visualized by Q criterion for: a) Flat bed; b) Scour stage-1; c) Scour stage-2. (HV: horseshoe vortex, CV: corner vortex)

Secondary and tertiary horseshoe vortices HV2 and HV3 get closer to the abutment at this stage. At the upstream of the abutment HV1 and HV2 are confined within the scour hole whereas HV3 follows its edge. With the formation of the scour hole, a new counter rotating horseshoe vortex HV4 forms in between HV2 and HV3 close to the bed. This vortex pushes HV2 away from the bed (see Figure-4b). As a result this vortex gets closer to the main horseshoe vortex HV1 and starts interacting with it. At a location close to the tip of the abutment HV1 and HV2 merges into one vortex which will be called as HV1* (see Figure-4c). Past the abutment HV1* follows the upslope and gets away from the bed. At a distance approximately 3.5D downstream of the abutment axis, core of HV1* reaches mid-flow depth.

Compared with the first scour stage at stage-2 scour hole gets approximately 8% and 21% larger in the lateral and streamwise directions respectively (see Figure-1). Moreover, the maximum scour depth measured from the free surface increases from 1.70D to 1.85D. However the horseshoe vortex system is very similar to the one observed in stage-1. The only difference is the length scale over which HV1* remains coherent. At stage-1 HV1* remains coherent up to a distance of 4D from the abutment axis in the downstream direction whereas in stage-2 HV1* is coherent up to 7D away from the abutment axis. This is related to the difference in the bathymetry at different scour stages, especially the steepness of the upslope at the downstream of the abutment (see Figure-1). Since at stage-1 the magnitude of this slope is larger, $HV1^*$ gets away from the channel bed at a shorter length and diffuses within the flow quickly.

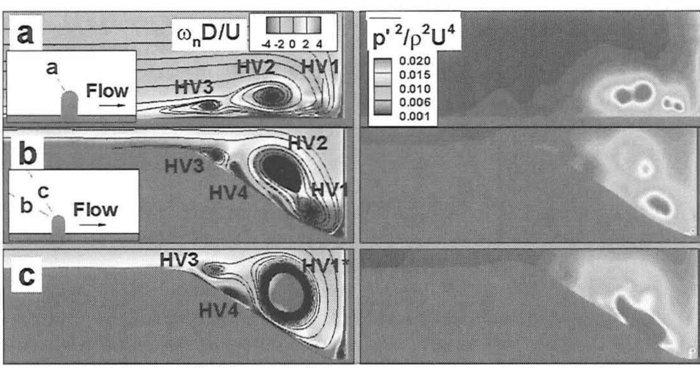

Figure-4: Mean out of plane vorticity contours together with the streamline patterns and resolved pressure r.m.s. fluctuations in representative vertical sections for: a) Initial scour stage; b) Scour stage-2; c) Scour stage-2. (see insets in a and b for plane locations)

Figures 4 show the streamline patterns superimposed on normalized out-of-plane vorticity contours, $\omega_n D/U$, and the distribution of the normalized pressure r.m.s. fluctuations $\overline{p'^2}/(\rho^2 U^4)$ on vertical planes which cut through the HV system at different stages of scour. Here ω_n is the out of plane vorticity, whereas ρ is the density. Throughout all the scour process pressure r.m.s. fluctuations are amplified within the core location of the primary and secondary necklace vortices. Moreover, at the initial stage of scour both for HV1 and HV2 r.m.s. pressure fluctuations show a double peaked distribution (see Figure-4a). This is a consequence of the bimodal nature of the flow within the main and secondary horseshoe vortices. The presence of large scale aperiodic oscillations were identified within the HV system forming around junction flows for the first time by Devenport and Simpson (1990). Koken and Constantinescu (2008a and 2008b) also identified this kind of oscillations for vertical wall abutment flows. However this is the first time these bimodal oscillations are observed both for the main and the secondary horseshoe vortices. The main reason for HV2 to have this bimodal behavior just like HV1 is that the core of HV2 is close enough to the abutment wall to get affected by it. Once the scour hole starts forming, as discussed earlier, HV2 is pushed towards HV1 because of the presence of a counter-rotating horseshoe vortex HV4 beneath HV2 close to the bed (see Figure-4b). At this section the bimodal nature is still present for HV1 (see the elongated amplification region within the core location of HV1). Even after the merging of HV1 and HV2 bimodal oscillations are observed within the core of HV1* at sections close to the abutment tip (see Figure-4c).

Bed Shear Stress

The distribution of the normalized mean bed shear stress at initial stage and two later stages of the scour are given in Figure-5. At the initial stage, large bed shear stress values are observed in the acceleration region close to the tip of the abutment and beneath the horseshoe vortices (especially beneath HV1). Maximum normalized mean bed shear stress is measured as 0.015 at a location close to the tip of the abutment. For the experimental flow conditions the critical normalized bed shear stress is obtained from the Shields diagram as $\tau_{wc}/(\rho U^2) = 0.007$. Possible scour regions where τ_w is larger than τ_{wc} are located at the upstream of the abutment and beneath the upstream part of the separated shear layers and the main horseshoe vortex HV1 (see Figure 5a).

At scour stage-1, with the formation of the scour hole at distances close to the bed, separated shear layers tend to curve behind the abutment. Because of this mechanism, some of the separated shear layer eddies tend to be entrained within the recirculation region. As a result, large bed shear stress values are observed at the downstream part of the abutment close to its tip. Also beneath the position where HV1 and HV2 merges, large bed shear stress values are observed. The maximum normalized mean bed shear stress value observed at stage-1 and stage-2 is around 0.01 and there is only a very small region at the downstream of the abutment where normalized mean bed shear stress is larger than $\tau_{wc}/(\rho U^2) = 0.007$. However this critical value is obtained for flat bed conditions and has to be modified to take into account the bed slope effects. This is done by the formulation provided by Brooks and Shukry (1963), and the corrected normalized critical bed shear stress, $\tau_{wc}^*/(\rho U^2)$, for sediment entrainment is calculated at every point on the bed. Obtaining this value, distribution of τ_w/τ_{wc}^* is plotted over the bathymetry both at stage-1 and stage-2 (see Figure-6). Locations where this ratio is larger than 1 (which is enclosed by solid lines in Figure-6) represents the possible scour regions. Consistent with the experimental observations, the scour occurs mostly at the upstream of the abutment along the walls of the scour hole at two separate locations. There is also a small region at the base of the scour hole which is exposed to erosion. Compared with stage-1, one can see the considerable decrease in the possible erosion area at stage-2. This is logical as stage-2 is closer to the equilibrium scour conditions at which there is practically no erosion (τ_w / τ_{wc}^* is always less than 1).

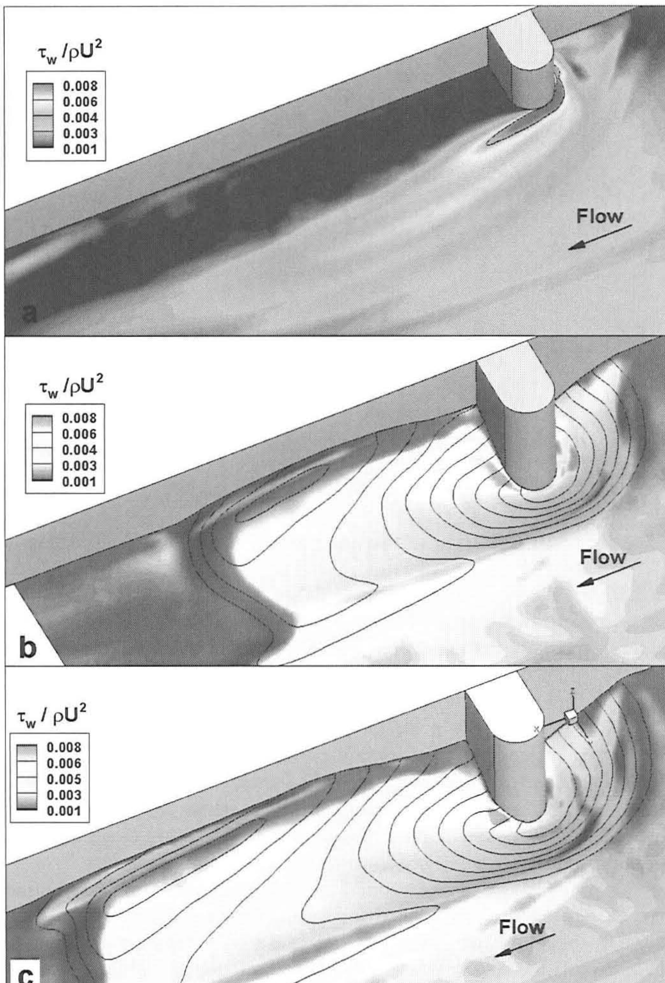

Figure-5: Distribution of the normalized mean bed shear stress for: a) Flat bed (solid line is $\tau_w / \rho U^2 = 0.007$); b) Scour stage-1; c) Scour stage-2.

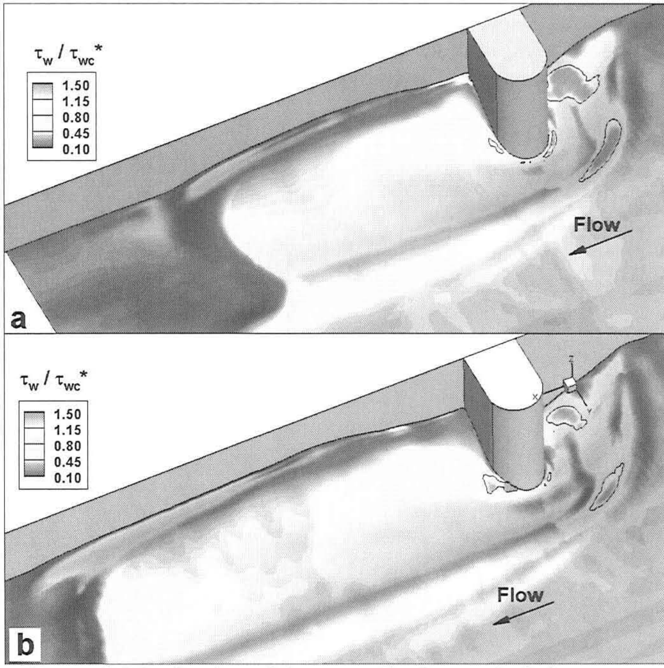

Figure-6: Distribution of the normalized mean bed shear stress

CONCLUSIONS

DES is used in the present study to investigate the changes in the coherent structures and especially the horseshoe vortex system at different stages of the scour process. At the initial stage of the scour, main horseshoe vortex is smaller in size and diffuses rapidly within the flow filed while the secondary necklace vortex is larger in size and remains coherent for a longer length in the streamwise direction. At this stage both of the vortices undergo aperiodic bimodal oscillations. Those oscillations cause the horseshoe vortices to induce large bed shear stress values beneath them. As the scour hole starts forming secondary necklace vortex HV2 gets closer to the primary necklace vortex HV1 and merges with it at a location close to the abutment tip. Bimodal oscillations are still present for this newly formed vortex.

At the initial stage of the scour bed shear stress values are obtained to be larger than the critical value required for sediment entrainment in the acceleration region close to the tip of the abutment and especially beneath the main necklace vortex HV1. This is the region where erosion starts forming. As the scour hole starts developing, at stage-1 mainly at two locations shear stress values exceed critical bed shear stress. These regions lay on the downslope of the scour hole at the downstream of the abutment and at the location where the scour hole is curved in the flow direction. This explains how the scour hole grows in the lateral and longitudinal directions. As the erosion continues at stage-2 at the same locations shear stress values are still larger than the critical value. However the area of these regions are considerably smaller. This is an expected result as the flow is approaching to the equilibrium scour conditions.

Since the changes in the structure of the horseshoe vortex system is not very different at stage-1 (2 hour scour) and stage-2 (4 hour scour); as a next step, a new experiment and a simulation will be held i.e. for 8 hour scour conditions.

ACKNOWLEDGEMENTS

This project is supported by TUBITAK (The Scientific and Technological Research Council of Turkey) under Project No: 108M590 and the computational resources used in this study were partly provided by TUBITAK ULAKBIM High Performance Computing Center, which are gratefully acknowledged here.

REFERENCES

Brooks, N. H., and Shukry, A. (1963). Discussion of "Boundary shear stress in curved trapezoidal channels." by A. T. Ippen and P. A. Drinker, Proc. ASCE, Journal Hydraulics Division, 89, HY3, 327-333.

Devenport, W. J., Simpson, R. L. 1990. Time-dependent and time-averaged turbulence structure near the nose of a wing-body junction. *J. Fluid Mech.*, 210, 23-55.

Melville, B. W. (1997). "Pier and abutment scour: integrated approach." *Journal of Hydraulic Engineering*, Vol. 123(2), 125-136.

Constantinescu, G. and Squires, K. (2004). "Numerical investigations of flow over a sphere in the subcritical and supercritical regimes." *Phys. of Fluids*, 16(5), pp. 1449-1466, 2004.

Koken, M. and Constantinescu, G. (2008a). "An investigation of the flow and scour mechanisms around isolated spur dikes in a shallow open channel. Part I. Conditions corresponding to the initiation of the erosion and deposition process." *Water Resources Research*, 44, W08406, doi:10.1029/2007WR006489.

Koken, M. and Constantinescu, G. (2008b). "An investigation of the flow and scour mechanisms around isolated spur dikes in a shallow open channel. Part II. Conditions corresponding to the final stages of the erosion and deposition process." *Water Resources Research*, 44, W08407, doi:10.1029/2007WR006491.

Experiments Identifying Scour-Inducing Flow Patterns At a Gated Weir Stilling Basin

Ted M. Champagne[1], Santosh R. Ghimire, Ph.D., A.M. ASCE[2], Brian D. Barkdoll, P.E., Ph.D., D.WRE, F.ASCE[3], Juan A. González-Castrom Ph.D., M.ASCE[4], and Larry Deaton, Ph.D.[5]

[1]Graduate Research Assistant (tchampag@mtu.edu), [2]Post -Doctoral Associate, [3]Associate Professor (barkdoll@mtu.edu) Michigan Technological University, Civil and Environmental Engineering Department, Houghton, MI 49931

[4] Engineering Chief (jgonzal@sfwmd.gov), [5] Division Director (ldeaton@sfwmd.gov), Operations & Hydro Data Management Division, South Florida Water Management District, 3301 Gun Club Road, West Palm Beach, Florida 33406

ABSTRACT

Excessive scour downstream of stilling basins poses significant risk of structural failure. This problem was experimentally investigated at Michigan Technological University in a Froude-scaled, physical model of one such structure operated by the South Florida Water Management District. Detailed flow measurements were taken on a flow scenario that resulted in high scour, namely that of a high flow rate and upstream headwater depth and a low tailwater depth. Equilibrium bed scour and velocity measurements were taken using an Acoustic Doppler Velocimeter. Velocity data was used to construct a vector plot in order to identify which flow components contribute to the scour hole. It was found that downward-plunging flow upon leaving the stilling basin induces the primary scour hole.

INTRODUCTION

Despite the best efforts by engineers to design robust water control structures, bed scour can lead to unexpected structure failure if it is not monitored on a regular basis. Determining the extent of bed scour may require specialized equipment and training. In situations where bed scour is known to threaten a structure, steps should be taken to reduce the rate at which bed scour occurs. The costs of both monitoring and remediation of bed scour can be minimized by conducting experiments on a scale-model structure. A model of the structure in question may be constructed in order to study the effectiveness of the chosen method of bed scour reduction. These results, when used in conjunction with numerical modeling, should give the user a good idea of what to expect.

A significant amount of study has been devoted to address scour related issues in hydraulic structures including spillways, bridges, and culverts. Many researchers and scientists performed various kinds of experiments to understand the scour phenomena. Xu et al. (2004) performed an experiment in a glass flume and predicted scour depth ratio for non-aerated and aerated jets. Canepa and Hager (2003) performed experiments in which a free jet at an angle of 30° was injected to estimate the scour profile. Schmocker et al. (2008) conducted an experiment in a rectangular approach channel to study aeration distribution. Dey and Westrich (2003) conducted an experiment to study the scour hole profiles and flow characterization in a cohesive bed downstream of apron. Rahmeyer (1990) studied the effect of aeration on scour. Afify and Urroz (1993) studied the impact of jet height, nozzle impinging angle, and diameter on the air entrainment rate. The current paper presents the experimental results and analysis of flow characteristics and their impact on bed scour downstream of a stilling basin for one flow scenario. A real hydraulic structure, S65E, of the South Florida Water Management District (SFWMD) was modeled at a 1:30 scale in the hydrodynamic lab at the Michigan Tech to investigate the scenario.

SCOUR AT THE S65E

It was discovered that considerable scour had occurred downstream of the S65E control structure maintained and operated by the South Florida Water Management District. This structure consists of a gated weir stilling basin with six parallel lift-gates, and is the hinge-pin structure regulating flow from the Kissimmee River / C-38 canal into Lake Okeechobee (Gonzalez-Castro and Mohamed, 2009).

PROCEDURE

Preliminary experiments were conducted in the hydrodynamic lab at Michigan Tech to identify the flow scenario which yielded the most bed scour. Prior to starting the experiment, the scour region (see Figures 1-3) was filled with fine sand and leveled from the top of the end sill to the top of the partition separating the scour region from the sediment trap. The flume was then filled with water to the desired depth and a Nortek Vectrino Acoustic Doppler Velocimeter (ADV) was set up to measure scour in a location of expected deep scour until equilibrium condition were satisfied.

Description of Laboratory Set-up

A Scour Flume at Michigan Technological University, shown in Figure 1-3, was used to conduct the bed scour experiment. The flume is comprised of an inlet, flow-developing, spillway/stilling basin, scour, and sediment trap, and outlet sections (in order from upstream to down). The flume has an inside width of 0.92m (3ft) and a total inside length of 10.18m (33.39ft). The total flume height is 1.04m (3.41ft).

The bed contains 12.7mm (0.5in) gravel to roughen the boundary layer to ensure fully-developed flow prior to entering the spillway test section. Fully-developed flow was verified through the use of a Nortek Vectrino Fixed Probe Acoustic Doppler Velocimeter (ADV) in the flow developing section (ADV used for bed elevation previously). Data was collected at various elevations with the ADV, both at the beginning of the upward-slanted approach (x = -150) to the spillway and

30cm (11.81in) upstream (x = -180). The velocity of lateral and vertical flow was approximately zero at all elevations. The velocity profile of longitudinal flow was consistent with developed flow in that it was zero at the bed and increased as the distance from the bed was increased.

The spillway is 0.457m (1.5ft) wide and was modeled at a 1:30 vertical and longitudinal scale of a section of the SFWMD's gate structure S65E of 9.15 m (30ft) out of the prototype spillway length of 54.9m (180ft). The spillway is 0.1m (3.94in) high and 0.23m (9.05in) long (Figure 4) to comply with the 1:30 scale criterion. The spillway is followed by a stilling basin consisting of two rows of 40mm (1.57in) cubic blocks in which the blocks from each of the rows was offset from the other. At the end of the stilling basin was a 40mm (1.57in) tall triangular sill. There is a 90^{o} sudden expansion of the channel downstream of the stilling basin, even though in the S65E structure has a relatively smooth transition with sidewalls protected by rip-rap.

Downstream of the stilling basin was a 2.805m (9.20ft) long scour region filled to the top of the end sill with fine sand with a d_{50} = 0.56mm. This size was chosen to be as close as possible to the scaled size needed to model the sand size found in the prototype without being so small that it was cohesive. The scour region had an internal wall at the downstream end of 630mm (2.07ft) tall. The sand surface tilted downstream at a 1:30 slope to be consistent with the prototype.

Downstream of the scour section was a 1.70m (5.58ft) long sediment trap section where sediment settled out to keep it from re-circulating through the pump and return piping, thereby minimizing internal pump and pipe wear. This trap was seen to be effective in removing sediment as evidenced by the fact that virtually no sediment was observed going into the outlet section or anywhere else in the flume, especially going over the spillway and entering the stilling basin and scour region. The spillway height is high enough and vertical velocities low enough to ensure this.

Next the flow entered the 900mm (2.9 ft) long outlet section where it entered the 0.254m (10in) diameter outlet piping, after which it was re-circulated to the upstream end of the flume. Flow was re-circulated by a centrifugal pump and return piping.

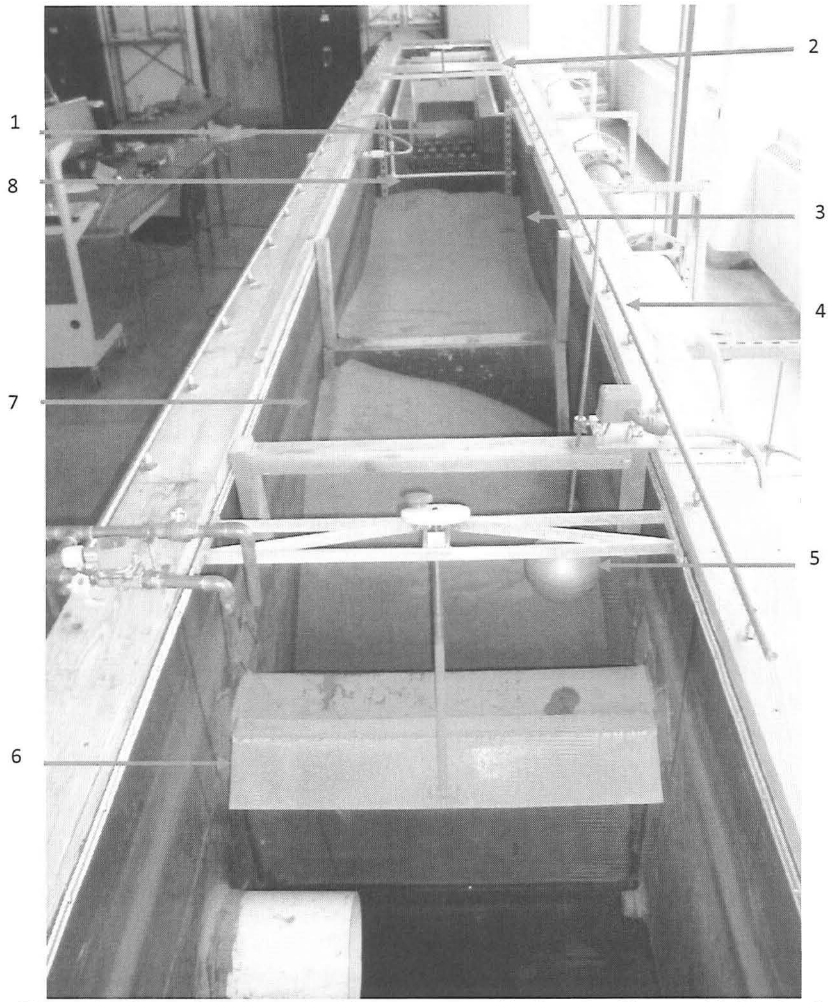

Figure 1. View of the flume looking upstream. (1. Gated spillway with blocks, 2. Instument carriage, 3. Sediment scour section, 4. Guide rails for instrument carriage, 5. Float valve to ensure constant water depth during experiments, 6. Adjustable tailgate to control downstream water level, 7. Sediment trap, 8. Pipe)

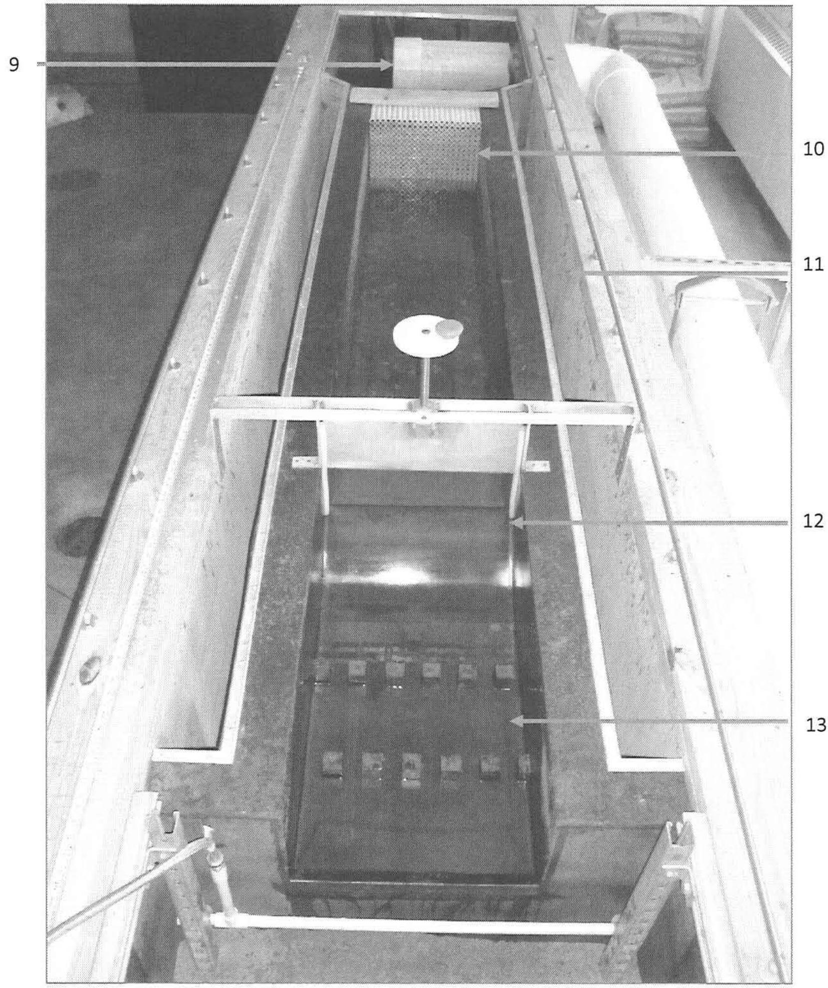

Figure 2. View of flume upstream section. (9. Inlet piping, 10. Flow straighteners, 11. Approach channel, 12. Gated spillway, 13. Stilling basin)

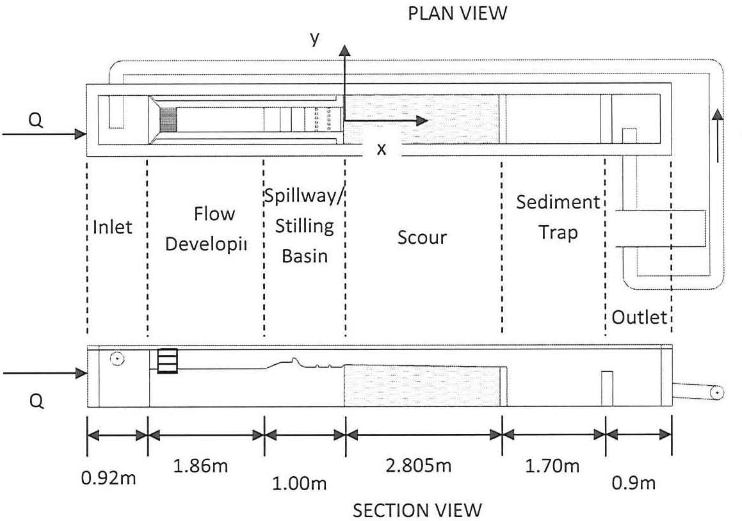

Figure 3. Scour flume with various sections and their dimensions

Since the water level can change during an experimental run due to evaporation or small leaks, the water level was kept constant by an adjustable float valve comprised of a buoyant bulb attached to an adjustable rod which triggers a valve connected to the inlet of the city water supply piping that fills the flume to shut off and on. This arrangement can maintain a constant water level of ±3mm. Surge protectors were installed to reduce the effects of water hammer from the sudden closing of the float valve.

The flow rate through the structure was controlled by a variable-speed electric controller/centrifugal pump and measured by a two-tube manometer/side contraction meter in the return piping. The rotation of the pump impellor is constant to within 0.005 Hz and the manometer has an accuracy of 0.79mm resulting in an accuracy of discharge of ±0.0060m^3/s (0.213 ft^3/s).

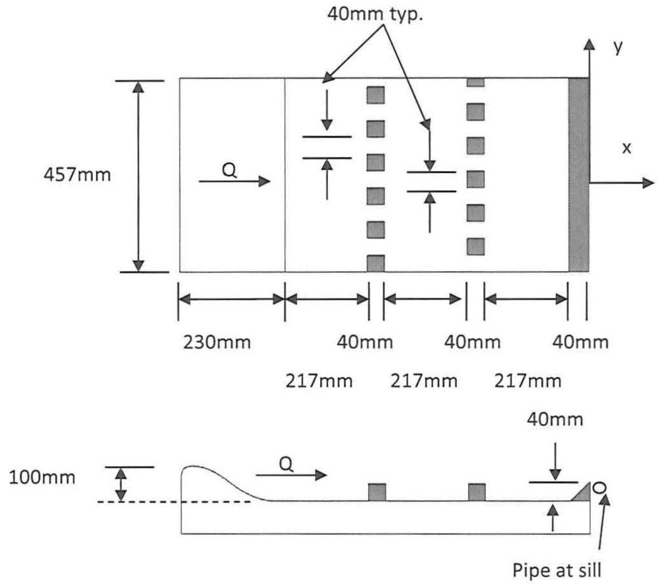

Figure 4. Spillway and stilling basin model

Water surface and bed profiles were measured by a point gage mounted on an instrument carriage that slides along rails installed on the top of the flume sidewalls.

Data Collection

The flow was then started and scour was measured periodically for the entire time to reach equilibrium using the depth function of the ADV at ten-hertz intervals. These data were then filtered by eliminating erroneous data identified visually and also by eliminating data which failed to satisfy minimum quality criteria. For ease of plotting and data analysis, the filtered data were then averaged in two-minute bins for presentation.

Flow was run for approximately 35 hours until sufficient time had elapsed for equilibrium scour conditions to occur, as determined by there being a change in scour depth over a 2-hr period of less than 0.5 percent. While measurements were taken at equilibrium-scour conditions, it is assumed that similar flow patterns were active throughout the experiment. After verifying equilibrium, the ADV was then used to begin collecting water velocity data. Velocity data was collected along the centerline of the flume using a grid resolution of 10 cm longitudinally and 2.5 cm vertically throughout the scour region of the channel. Data was collected at each point for 300 seconds at a frequency of 200-hertz utilizing a sample volume height of 7 mm.

The data was then processed through a series of filters to help identify erroneous velocity data. It was difficult to construct data filters that would remove erroneous data yet still capture intermittent vortex bursts in the flow. Trial and error revealed that a filter removing all data with acceleration greater than that of gravity proved most useful. After filtering, the average velocity was determined for each vector *u*, *v*, and *w*. This data was then aggregated to form a 2-D slice down the center of the channel. Plotting this data allowed the use of streamtraces to illustrate flow characteristics. Because the channel is symmetrical, transverse flow at the channel centerline is not expected and therefore *v* values are not included in this paper.

RESULTS

Uncontrolled free flow resulted in the greatest bed degradation with a scour hole of similar proportions to that observed at S65E control structure. In this flow scenario, flow through the structure is neither impeded by the sluice gate nor buffered by the tailwater before encountering the channel bed. Flow characteristics were determined by visual observation of both the flow and the ensuing scour patterns on the channel bed and velocity measurements collected. Behavior observed visually is the aerated nappe created by the flow exiting the stilling basin. Expectedly, flow in this area was organized with a high velocity. This flow split into two components as it approached the bed. A downward roller was formed with a near-bed component flowing upstream along with plunging region downstream of the separation point. The location of the separation point was several centimeters downstream from the bottom of the scour hole. Flow downstream from the scour hole formed a vertically contracting region due to the diminishing effects from the scour hole. This behavior is detailed with a vector plot in Figure 5, using streamtraces in Figure 6, and by dunes shown in Figure 7.

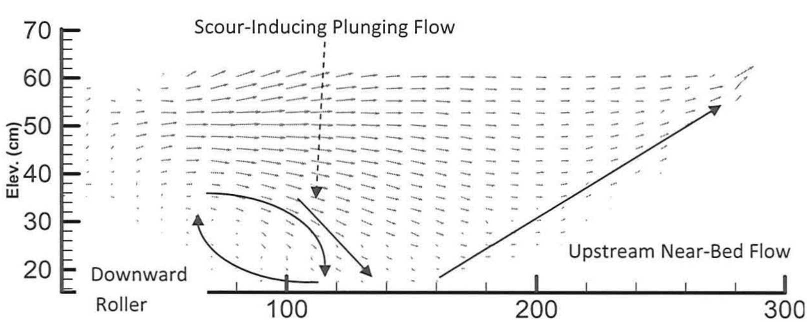

Figure 5. Vector plot at centerline of channel.

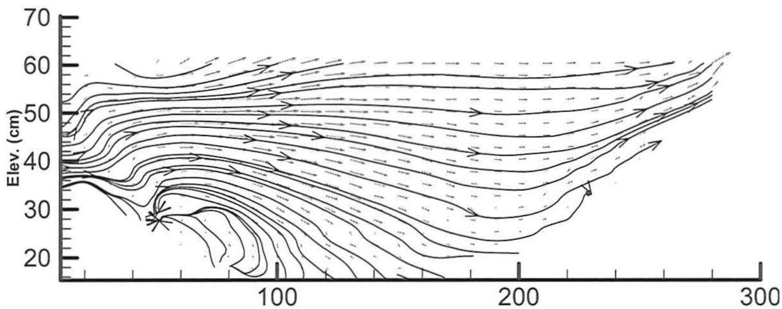

Figure 6. Streamtrace plot at centerline of channel.

Vertical vortices were found on both sides of the stilling basin due to the sudden expansion in channel width. This flow separation forms a downward roller upon contact with the channel side walls, which in turn travels down the channel sides where it splits upon contact with the bed. Flow then splits and forms two secondary vortices, one upstream and the other downstream, going along the corner formed by the channel wall and bed. This behavior was also confirmed while examining dune structure after ending the experiment (Figure 7).

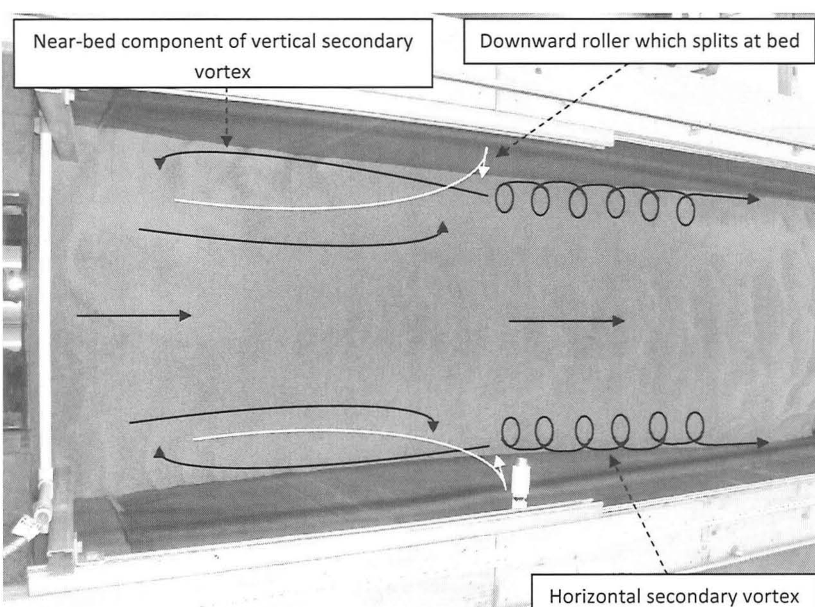

Figure 7. Dune structure (white is surface flow, black is near-bed flow).

CONCLUSION

The primary scour hole was formed due to concentrated flow exiting the stilling basin and impacting the channel bed. Scour geometry was affected by the primary downward roller in combination with the counter rotating vortices. To a lesser extent, numerous eddies caused by flow separation in the plan-view also contributed to the scour geometry. Future research will include the application of scour reduction mechanisms to the model structure in an effort to determine how their presence affect scour hole formation.

REFERENCES

Afifiy, A.M. and Urroz, M. (1993). "Plunge Pool Aeration Due to Inclined Jets." *Hydraulic Engineering,* Proc. of the 1993 Conference, San Francisco, CA, July 25-30, 1993, 851-855.

Canepa, S. and Hager, W.H. (2003). "Effect of Jet Air Content on Plunge Pool Scour." *Journal of Hydraulic Engineering*, 129 (5), 358–365.

Dey, S., Westrich, B. (2003). "Hydraulics of Submerged Jet Subject to Change in Cohesive Bed Geometry." *Journal of Hydraulic Engineering,* 129(1), 44–53.

Gonzalez-Castro, J.A. and Mohamed A. (2009). *Flow Ratings for Kissimmee River Pool A Revisited.* Technical Publication OC&HDM 2010-01. South Florida Water Management District, West Palm Beach, FL.

Rahmeyer, W. (1990). "The Effect of Aeration on Scour." *Hydraulic Engineering, Proc. of the 1990 National Conference,* Sponsored by the Hydraulics Division of the American Society of Civil Engineers, 1990, 530-536.

Schmocker, L.; Pfister, M; Hager, W.H.; and Minor, H-E. (2008). "Aeration Characteristics of Ski Jump Jets." *Journal of Hydraulic Engineering,* 134 (1), 90–97.

Xu, W.; Deng, J.; Qu, J.; Liu, S.; and Wang, W. (2004). "Experimental Investigation on Influence of Aeration on Plane Jet Scour." *Journal of Hydraulic Engineering*, 130 (2), 160–164.

Effect of Tailwater Depth on the Scour Downstream of Falling Jets

S. H. Musavi Jahromi[1] and H. Helalat Nasserian[2]

[1]Associ. Prof., Faculty of Water Science Engineering, Shahid Chamran University, Ahwaz, Iran, Ph. +98-611-3330635, email: habib@musavi.info
[2]M.Sc in hydraulic Engineering, M.A.P.T. Consulting Engineers Firm, Tehran, Iran, Ph. +98-916-3032706, email: honaserian@yahoo.com

ABSTRACT

In this paper the results of an experimental study about effect of tailwater depth on the characteristics of local scour at downstream of falling jets is presented. A flume with 5m length, 25cm height and 10cm width has been established. Jets with three shapes including; circular, square and rectangular are connected to the end of the flume. A Siliceous bed with d_{50}=1.27mm, three drop heights including; 35cm, 65cm and 95cm and three tailwater depth; 6cm, 12cm and 18cm have been applied downstream of the jet. Different analysis of the observed data showed that the characteristics of scour-hole depend on erosion parameter, $F_0/(H_c/R_H)$, and tailwater parameter, T_w/R_H. Also it is considered that increasing the tailwater depth from 6cm to 12cm and then to 18cm, at first causes increasing the depth, width and length of scour-hole and also the length of sediments mound on the average of 104, 42, 39 and 83%, respectively, then causes decreasing these characteristics on the average of 23, 24, 18 and 16%, respectively. In this case the height of sediments mound at downstream of scour-hole will increase on the average of 52%. Finally, an equation as the scour characteristics predictor is proposed.

INTRODUCTION

Jets of water that impinge on the free surface due to the flow from an outlet situated above the free water surface are referred to as plunging jets. The overflow through openings of dam, flow from ski jump spillways and pipe outlets are some of the practical examples of plunging jets. The scour downstream of these hydraulic structures is of frequent occurrence and constitutes an important field of research. Moreover local scour can cause dam failure and endanger the safety of the dam. Due to the complex nature of these flows and their interaction with sediment beds, research on the erosion by jets has been mainly empirical. Abida and Townsend (1991) accomplished a study that investigated the local scouring phenomenon in sand bed downstream of model box culvert outlets. Maximum depth of local scour was found to vary with the tailwater depth. But, in this experiment the lying culvert on the bed with no drop height was applied. Nasehi (1996) performed a study in order to consider local scour at downstream of vertical drops. On the basis of experimental results, scour depth has direct relation with discharge and vice versa relation with tailwater depth. Also mounds are forming at downstream of scour-hole which their height and location depend on tailwater depth and flow discharge. Najafi and Ghodsian (2004) have done an experimental study on downstream scour of pipe culverts. Experimental results showed that increasing tailwater depth causes decreasing depth and width of scour-hole, but it causes increasing the scour-hole length, sediments mound height and scour-hole start point. Sarathi et al. (2005) accomplished a study on local scour due to 3D wall jets in non-cohesive sand beds. The results indicated that the tailwater has an effect on the scour geometry at lower tailwater conditions, however, at higher tailwater conditions, the effect was found to be minimized. Ghodsian et al. (2006) performed experiments on the scour due to impinging rectangular jet in uniform cohesive bed material. The results indicated that the depth of scour initially increases by increasing the tailwater depth and then decreases. In this paper, using dimensional analysis, a few dimensionless parameters have been established. A flume with several experimental instruments has been set up in the hydraulic laboratory of Shahid Chamran University, Ahwaz, Iran. The characteristics of the downstream scour and sediment mound due to the tailwater depth changes have been studied.

MATERIALS AND PROCEDURES

A schematic sketch of the experimental facilities is shown in figure 1. A flume with 5m length, 25cm height and 10cm width has been established. Plexiglas jets with 30cm length and three shapes including; circular, square and rectangular are connected to the end of the flume. A sediment tank with 2m length, 1.5m width and 0.75m depth has been applied downstream of the jet. A slide gate is placed at the end of the sediment tank to regulate the tailwater depth. The height of the falling jets was set to be 35cm; 65cm and 95cm. Characteristics of the jets are presented in Table 1. In all tests, the silica with d_{50}=1.27mm and unit weight (γ) of 2.65 gr/cm^3 was used as the downstream bed materials. The grain size distribution curve of the materials is shown in Figure 2. For measuring the characteristics of the scour-hole and its downstream sediments mound, a point gauge with accuracy range of ±1mm was used. It was placed on the rails and can be moved manually in longitudinal and transversal directions. In all tests, it was tried to maintain the water level behind the jets constant and equal to 15.5cm. The characteristics of the scour-hole and its downstream mound were measured after 31, 100 and 316 minutes, separately.

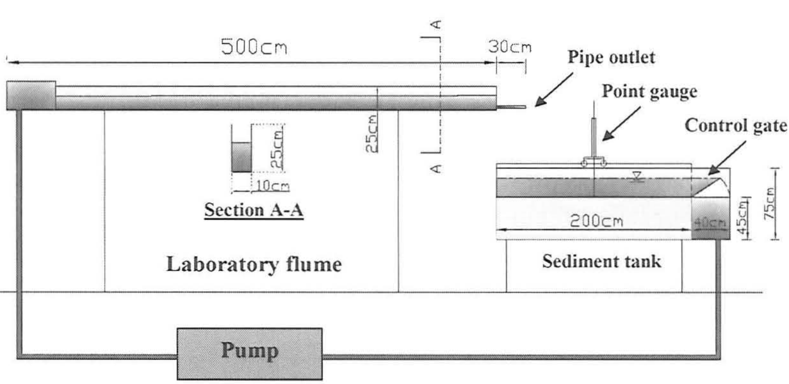

Figure 1. Longitudinal profile of laboratory flume and its attachments

Table 1. Characteristics of falling jet

Jet shape	Cross-sectional Area (m^2)	Hydraulic Radius (m)	Width (m)	Height (m)	Discharge (l/s)
Circular	0.0007	0.0075	0.03	0.03	1.02
Square	0.0009	0.0075	0.03	0.03	1.27
Rectangular	0.0012	0.00857	0.04	0.03	1.77

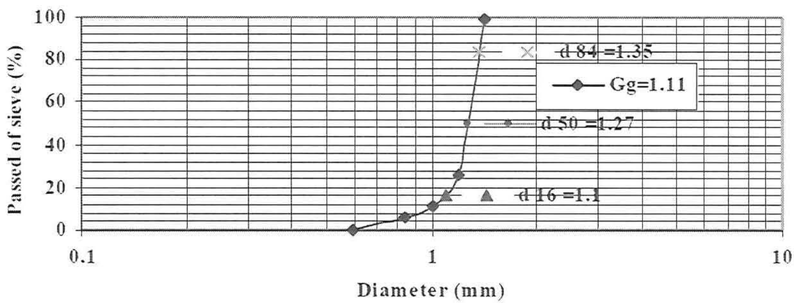

Figure 2. Grain size distribution curve

DIMENSIONAL ANALYSIS

Scour processes downstream of a jet outlet depend on many variables as follows:

1) The flow characteristics including discharge (Q), velocity at jet outlet (V), the tailwater depth (T_w), the water density (ρ), the dynamic viscosity of water (μ), the kinematic viscosity of water (υ), acceleration due to gravity (g) and the water level behind the jet (H).

2) The bed materials characteristic parameters: the effective particle size of the bed materials (D_s), the density of the bed materials (ρ_s), the geometric standard deviation of particle sizes (σ), the fall velocity of sediments (ω), the angle of repose (φ) and the shape factor (S_f).

3) The jet characteristics: the height of jet location to the bed level (H_c), the jet slope (S), the jet length (L), the jet roughness coefficient (n), the shape of jet section (hydraulic radius) (R_H), the jet section area (A), and the entrance loss coefficient (k). Finally time (t) and the sediment tank width (B) are two other parameters effecting the scour-hole conditions.

Thus, if Ψ represents any dimensions of scour-hole and its downstream sediments mound, then:

$$\psi = f(Q,V,T_w,\rho,\mu,\upsilon,g,H,D_s,\rho_s,\sigma,\omega,\varphi,S_f,H_c,S,L,n,R_H,A,k,t,B) \qquad (1)$$

However, for the purpose of this study some of these variables can be disregarded, and only the more significant ones are preserved. Q and A are eliminated since V=Q/A. μ and υ are eliminated since $\rho=\mu/\upsilon$. ω is eliminated since

$\omega=(\rho_s-\rho)gD_s^2/18\mu$. The same bed material with uniform gradation was used for all experiments and thus φ and S_f and σ were eliminated. H and B were considered to be constant in all experiments and therefore were disregarded. S=0 since the pipe outlet was horizontal. k was not included because the study is limited to on type of pipe entrance. L is eliminated since the model pipe length is too short to affect the flow. The same pipe material was used for all experiments and thus n was eliminated in the analysis. t was not included because we do not consider the scour-hole time changes in this study. Therefore, Eq. (1) can be simplified to:

$$\psi=f(V,T_w,\rho,g,d_{50},\Delta\rho,H_c,R_H) \tag{2}$$

Upon performing dimensional analysis on Eq.(2), the following dimensionless term is obtained:

$$\frac{\Psi}{R_H}=f\left(\frac{T_w}{R_H},\frac{d_{50}}{R_H},\frac{H_C}{R_H},\frac{V}{\sqrt{gR_H}},\frac{\Delta\rho}{\rho}\right) \tag{3}$$

By rearranging Eq. (3), Eq. (4) is obtained:

$$\frac{\Psi}{H_C}=f\left(\frac{T_W}{R_H},\frac{F_0}{H_c/R_H}\right) \tag{4}$$

In Eq. (4), F_0, is the densimetric Froude Number as follow:

$$F_0=\frac{V}{\sqrt{gd_{50}(\Delta\rho/\rho)}} \tag{5}$$

The scour characteristics measured in this experimental study were: the maximum scour-hole depth (d_s), the maximum scour-hole length (L_s), the maximum scour-hole width (W_s), the maximum sediments mound height at the downstream of score hole (h_m), the maximum sediments mound length at the downstream of score hole (L_r), the horizontal distance of start point of scour-hole from jet outlet end (L_{up}). Characteristics of scour-hole and its downstream sediments mound are shown in Figure 3.

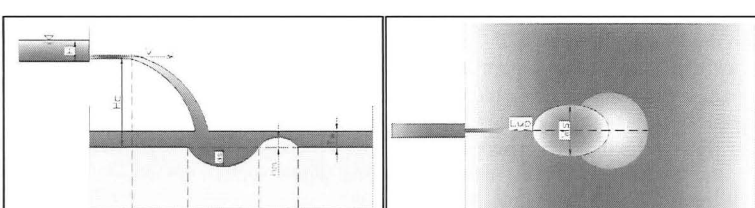

Figure 3. Schematic longitudinal profile and plan of the scour-hole

RESULTS AND DISCUSSION

A total of 27 experiments on 3 jet shapes with 3 fall heights and 3 different tailwater depths were conducted. Related data of scour-hole and its downstream sediments mound characteristics were measured after 316 minutes run of the physical model. From the curve of scour dimensions changes to time was observed that the scour dimensions will reach to asymptotic state almost after 316 minutes.

Observed Scour Profiles

Initially, longitudinal and lateral scour profiles, in the location of maximum scour depth due to the tailwater depth were considered. The Influence of the tailwater depth on scour process for rectangular jet shape and drop height of 35cm is shown in Figure 4. In this figure in the case of constant jet section and drop height, by increasing the tailwater depth from 6cm to 12cm and then 18cm, it is observed that:

1) The scour depth is increased from 10.5cm to 16.7cm and then will decrease to 13.2cm.
2) The distance of the location of maximum scour depth from jet end will increase from 43cm to 53cm and then to 57cm.
3) The scour width is increased from 45cm to 56cm and then will decrease to 45cm.
4) The scour length is increased from 48.5cm to 61.5cm and then will decrease to 53cm.
5) The sediments mound height will increase from 6cm to 11.7cm and then to 14cm.
6) The distance of the location of maximum sediments mound height from jet end is increased from 91cm to 110cm and then will decrease to 103cm.
7) The sediments mound length is increased from 30.5cm to 42cm and then will decrease to 41cm.
8) The distance of scour-hole start point from jet end remains approximately constant in 21cm, and then will increase to 26cm.

Similar figures obtained for other cases. Generally, by increasing the tailwater depth from 6cm to 12cm and then to 18cm, it is observed that:

1) Initially, the depth, width and length of scour-hole increase on the average of 104, 42 and 39%, respectively, and then will decrease 23, 24 and 18%, respectively.
2) The distance of the location of maximum scour-hole depth from jet end increases on the average of 7%.
3) The tailwater depth has noticeable influence on sediments mound height at the downstream of scour-hole. By tailwater depth increasing, the shape and form of settled sediments at the downstream of scour-hole is different. While the tailwater depth is low, sediments will settle in uniform state (with a constant height) at downstream of scour-hole approximately, but for high tailwater depths, the settled sediments form a climax which has steep slopes at upstream and downstream. Because in higher tailwater depths, the released sediments will be moved easily by water flow and will settle where the flow turbulence due to jet impinging on the bed decrease. So they lose their energy near the water surface and form a climax at downstream of the scour-hole. Generally, the increasing of tailwater depth causes increasing downstream sediments mound height on the average of 52%.

4) The distance of the location of the maximum sediments mound height increase on the average of 30% and then will decrease 12%.

5) The sediments mound length at the downstream of scour-hole initially increase on the average of 83%, and then will decrease 16%. Because in higher tailwater depths, climax formation will prevent the movement of released sediments to downstream. If these sediments have no enough energy to pass over the climax, they have to settle in the scour-hole. So that the sediments mound length will decrease.

6) Initially, the distance of scour-hole start point from jet end decrease on the average of 3% or remains constant and then will increase 20%.

7) At 12cm tailwater depth, maximum of scour characteristics are observed.

It also was observed that the movement manner and replacement of the released particles from the bed for various cases of the tailwater depth are different. In lower tailwater depths, released particles move vertically to the water surface, but after losing their kinetic energy a large amount of them will settle in the scour-hole again (ebullient manner). Whereas, in higher tailwater depths, impinging jet release particles and will move them to the downstream. So, no ebullient manner will be seen in the scour-hole.

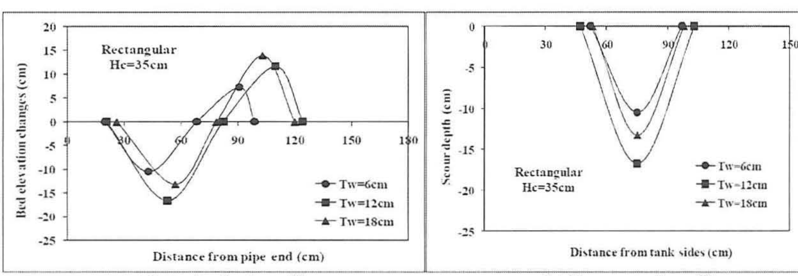

(a) Longitudinal profile (b) Transversal profile

Figure 4. Rectangular jet's scour profiles for different tailwater depths (Drop height=35cm)

Scour Characteristics Predictor

The dimensionless parameters as determined from the dimensional analysis were evaluated to assess their influence on scour characteristics. For this purpose a plot was developed that showed the relation between the Ψ/H_c and the erosion parameter, $F_0/(H_c/R_H)$, for three different sizes of tailwater parameter, T_w/R_H. In Figure 5, a plot of the scour-hole length dimensionless parameter with respect to the erosion parameter is shown. Similar plots were developed for other scour-hole and its downstream sediments mound characteristics. A regression line for the best fit is drawn for each tailwater ratio. The best equation form for each tailwater ratio was the power form as; $y=ax^b$, Where y is variable with Ψ/H_c and x is independent parameter of $F_0/(H_c/R_H)$, a and b are experimental constant parameters. Table 2 includes scour-hole length ratio for different tailwater ratios.

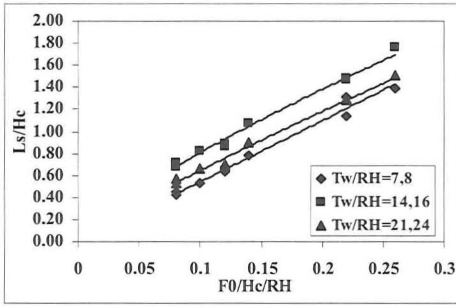

Figure 5. L_s/H_c versus $F_0/(H_c/R_H)$ for different tailwater ratios

Table 2. Equations coefficients for different tailwater ratios

Scour characteristics	T_w/R_H	a	b	R^2
	7,8	5.615	1.015	0.989
L_s/H_c	**14,16**	4.827	0.777	0.986
	21,24	4.817	0.874	0.982

It is observed that with increasing of $F_0/(H_c/R_H)$ for different ratios of T_w/R_H, the parameter of Ψ/H_c is increasing. Also it is found that for a constant value of $F_0/(H_c/R_H)$, the greatest values of d_s/H_c, L_s/H_c, W_s/H_c and L_r/H_c parameters occurred at T_w/R_H=14,16 and the greatest values of h_m/H_c and L_{up}/H_c parameters occurred at T_w/R_H=21,24. In order to present a united equation for all ratios of T_w/R_H, a general form of the equation is as follows:

$$\frac{\Psi}{H_c} = a\left(\frac{T_w}{R_H}\right)^b \left(\frac{F_0}{H_c/R_H}\right)^c \tag{6}$$

The coefficient of c can be a function of T_w/R_H. For evaluating the coefficient of c, four states of the function of T_w/R_H must be taken into consideration (Table 3). To determine the best form of the coefficient of c to be assigned to equation 6, the following equation can be used to minimize prediction error:

$$E = \frac{100}{N}\sum_{i=1}^{N}\left|\frac{Y_{observed} - Y_{computed}}{Y_{observed}}\right| \tag{7}$$

Where E is error term between observed and computed values, $Y_{observed}$ and $Y_{computed}$ are observed and computed values of considered parameter, respectively, and N is number of parameters. Optimum values of equation coefficients, for various forms of $F_0/(H_c/R_H)$ exponent, as an example for scour-hole length, is shown in table 3.

Table 3. Coefficients of equation (6) and rate of error percent for various forms of $F_0/(H_c/R_H)$ exponent (scour-hole length)

Exponent form	a	b	c	d	R^2	E%
c	3.981	0.098	0.892	-	0.913	11.404
$c(T_w/R_H)$	0.124	1.336	0.051	-	0.842	15.433
$(T_w/R_H)^c$	4.736	0.028	-0.046	-	0.915	12.304
$c(T_w/R_H)^d$	26.992	-0.626	3.015	-0.468	0.923	9.959

It is observed that when the exponent form is $c(T_w/R_H)^d$, the error term will be minimized. Similar tables were developed for other scour-hole and its downstream sediments mound characteristics. A general form of the scour characteristics prediction equation is as follows:

$$\frac{\Psi}{H_c} = a\left(\frac{T_w}{R_H}\right)^b \left(\frac{F_0}{H_c/R_H}\right)^{c(T_w/R_H)^d} \tag{8}$$

Optimum values of the equation coefficients for other scour characteristics, is shown in table 4. In figure 6, a plot of the observed scour-hole length with respect to the computed values is shown. Similar plots were developed for other scour-hole and its downstream sediments mound characteristics. It is observed that the computed values of scour-hole length have the least variance with observed values.

Table 4. Summery of coefficients and error percent of estimation equation of other scour characteristics

Scour characteristics	a	b	c	d	R^2	E%
d_s	154.261	-1.791	21.937	-1.254	0.931	11.044
W_s	103.816	-1.248	8.255	-0.929	0.902	11.233
h_m	2.992	-0.322	3.903	-0.508	0.962	6.863
L_r	113.849	-1.322	11.378	-1.016	0.905	10.8
L_{up}	0.501	0.358	0.278	0.211	0.856	7.996

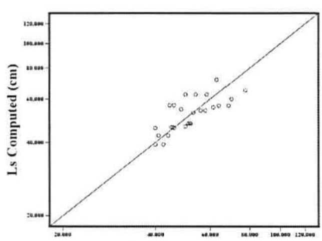

Figure 6. Comparison between observed and computed values of scour length

CONCLUSION

This experimental study investigated the effect of tailwater depth on the characteristics of local scour at downstream of falling jets. The following conclusions are derived:

1. The characteristics of scour-hole and its downstream sediments mound depend on erosion parameter, $F_0/(H_c/R_H)$, and tailwater parameter, T_w/R_H.
2. The tailwater depth has significant influence on sediments mound height. In lower tailwater depths, sediments will settle in uniform state (with a constant height) at downstream of scour-hole, but in higher tailwater depths, the settled sediments form a climax which has steep slopes at upstream and downstream.
3. The tailwater depth changes have double influences on scour characteristics. Increasing the tailwater depth from 6cm to 12cm causes increasing the depth, width and length of scour-hole and so the length of sediments mound on the average of 104, 42, 39 and 83%, respectively. But increasing the tailwater depth from 12cm to 18cm causes decreasing these characteristics on the average of 23, 24, 18 and 16%, respectively.
4. Generally, the increasing of tailwater depth from 6cm to 12cm and then to 18cm, causes increasing sediments mound height on the average of 52%.
5. A general form of the scour characteristics prediction equation for all tailwater ratios is as follows:

$$\frac{\Psi}{H_c} = a\left(\frac{T_w}{R_H}\right)^b \left(\frac{F_0}{H_c/R_H}\right)^{c(T_w/R_H)^d}$$

It is observed that the computed values by this equation have the least variance with observed values.

REFRENCES

Abida, H., Townsend, R. D., (1991). "Local scour downstream of box-culvert outlets", *Journal of irrigation and drainage Engineering*, Vol. 117, No. 3, P.P. 425-440

Ghodsian, M., Melville, B., Coleman, S., (2006). "Scour caused by rectangular impinging jet in cohesiveless beds", *Proc. Third International Conference on scour and erosion*, ICSE, Nov. 1-3, Amsterdam, The Netherlands

Najafi, j., Ghodsian, M., (2004). "Experimental Study of scour hole properties at downstream of pipe culvert", Technical faculty, Tehran University, Tehran, Iran, *Journal No. 84*, P.P. 329-338

Nasehi, M., (1996). "Scour profile at downstream of vertical drops", *Proceeding of the 4th international River engineering conference*, Shahid chamran University, Ahvaz, Iran, P.P. 474-488

Sarathi, P., Faruque, M.A.A., Balachandar, R., (2005). "Local scour by three-dimensional wall jets", *Proc. 17th Canadian Hydrotechnical Conference*, CSCE, August 17-19, P.P. 647-654, Edmonton, Alberta

Experimental Study on Interaction of Waves, Currents and Dynamic Morphology Changes

Siddique Mohsin[1], Saki Tomita[2] and Yoshimitsu Tajima[3]

[1]Coastal Engineering Laboratory, Department of Civil Engineering., The University of Tokyo, 7-3-1 Hongo Bunkyo-ku, Tokyo 113-8656, Japan;
email: yourmohsin@coastal.t.u-tokyo.ac.jp
[2]ditto; email: tomitasaki@coastal.t.u-tokyo.ac.jp
[3]ditto; email: yoshitaji@coastal.t.u-tokyo.ac.jp

ABSTRACT

Time-to-time interactive features among waves, currents and dynamic morphology changes are essential to quantitatively determine the beach erosion problems. This study puts special focus on the impact of dynamically changing beach profiles on the wave and current properties. We first developed a new set of image-capturing techniques that enabled us to obtain high-resolution quantitative data sets of waves, currents and bottom bed profiles both in time and space domains. In a 2D wave flume, multiple high-speed cameras and normal video cameras were installed beside the flume to capture the time-varying bottom bed profiles and spatial distributions of instantaneous current velocity and surface water fluctuations across the entire surf zone. Brightness of the obtained image was transferred to the instantaneous suspended sediment concentrations. The obtained data sets successfully describe the formation and onshore movement of the bars until they reach to the equilibrium state.

INRTODUCTION

As the wave shoals on the sloping beach in the surf zone, its profile dramatically changes. Initially, waves slow down in the surf zone and starts gaining height as they propagate on sloping beach until they reach to a breaking depth where waves are forced to break. At this height, wave crest deforms to forward-leaning profile and yields surface roller that collapses in front of the wave crest. This complicated nonlinear phenomenon of wave breaking generates turbulence which plays vital role in transferring wave energy, momentum, and mass fluxes into the water body in the surf zone (Huang et al., 2009). The generated turbulence reaches to the bottom and picks up bottom sediments in suspension. Suspended sediments are then transported by instantaneous and mean current velocity and cause morphology changes which, in turn, affect the nearshore hydrodynamics. This interactive process continues until the beach reaches to a state of equilibrium.

To predict the beach erosion and topography changes along beach with a greater accuracy, detailed knowledge of the flow parameters such as spatial-temporal surface water elevations, the corresponding internal flow dynamics and particularly their interactions with morphology are crucial. Other important parameters, such as time averaged currents, turbulence and sediment transport can readily be estimated based on obtained spatial instantaneous current velocities.

Our understandings of near-surf-physics are usually based on quantitative measurements carried out during several laboratory studies. However, most of these experimental studies are limited to wave breakings on uniformly sloping fixed bed beaches. Traditionally, two types of techniques have often been used to investigate changes in water surface profile of waves and its underwater dynamics. The first approach is to apply point measurement techniques such as Acoustic Doppler Velocimetry, (ADV) or Laser Doppler Velocimetery, (LDV) in combination with wave gauges (e.g., Elgar et al., 2005, Stive, 1980, Nadaoka et al., 1989, Ting and Kirby, 1996, Cox and Kobayashi, 2000, Shin and Cox, 2006 and Longo, 2009). Over equilibrium profile of natural sandy beaches, Hurther, et al. (2007) used ADV and optical back scatters (OBS) to study the turbulent energy production and dissipation under broken irregular waves. The second approach is full-field measurements by the use of the state of art Particle Image Velocimetry (PIV) technique. Recently, studies by Govender et. al., (2002), Govender et. al. (2004), Kimmoun and Branger (2007) demonstrated the skills of full-field PIV measurements over sloping fixed bed beaches in wave flumes. The results are overwhelming and present details about the fluctuating velocity components and various features of turbulence kinetic energy such as dissipation, production, advection, convection during various wave phases. In order to capture the interactive features of changing bed profiles and surrounding wave and current fields, it is essential to obtain synchronized high-resolution data sets of both current and bottom bed profiles.

Therefore, the present study aims to develop a new set of image-capturing techniques that enable us to obtain synchronized high-resolution quantitative data sets of waves, currents and movable bottom bed profiles both in the time and space domains across the entire surf zone. High speed video cameras (HSVCs) and normal video cameras are utilized to reveal the instantaneous current velocity, surface water fluctuation and bottom bed evolution by the use of Boundary Detection Technique (BDT) coupled with PIV technique. In our data sets we successfully captured the migration of ripples, formation of sand bars from the plane sloping bed and interaction of currents and topographic changes.

EXPERIMENTAL SETUPSAND PROCEDURES

The laboratory experiments were performed in a 30m long, 0.6m wide, and 0.8m deep 2D wave flume at the University of Tokyo. Progressive waves were generated by piston-type wave maker located at one end of the flume. A schematic diagram of wave flume and apparatus is shown in figure 1. Three HSVCs and two normal video cameras were mounted near the glass wall as shown in figure 1. HSVCs were used to determine spatial distributions of instantaneous current velocity field on a 1/10 sloping movable sandy bed of uniform sand grains (D_{50}=0.24mm), while normal video camera were mounted to obtain surface water elevations and bottom bed profile. HSVCs employed in experiments were Casio EX-FH20 that captures images with frame rates of 120 fps and resolutions of 640x480 pixels. A laser sheet was also introduced from the top to illuminate the suspended sand particles and no special seeding particles were utilized. Laser sheet was set 2 cm away and parallel to the glass wall to avoid the side wall effects if any.

The spatial size of field of views (FOVs) by each HSVCs was 190x150mm, whereas the spatial sizes of normal video camera 1 (outside of the surf zone) and video camera 2 (swash zone) were kept as 430x250mm and 230x130mm respectively. Spatial bench marks were also marked inside FOVs of each camera to rectify the image results during the analysis. FOVs recorded by 3 HSVCs, were later used to determine velocity field distribution over the entire surf zone while surface water elevations and bottom bed profile were computed from images of all five cameras based on BDT.

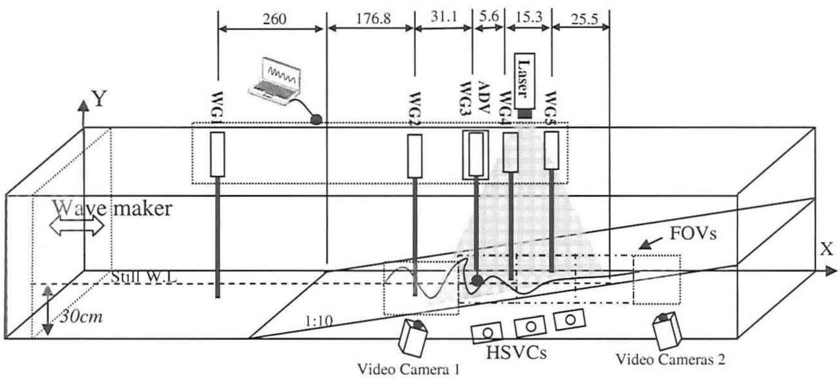

Figure 1: Schematic diagram of wave flume showing apparatus setup and connection details. (All dimensions are in *'cm'*)

Five wave gauges (one at offshore (WG1), one just outside the surf zone (WG2), two inside the surf zone (WG3 & WG4) and the other one in the swash zone (WG5) were installed for the purpose of validation of BDT. In addition, ADV was also installed outside the breaking point to calibrate the present PIV.

Monochromatic incident waves with heights of 3.31cm and period of 1sec were generated where the water depth was 30cm. The surf similarity parameter of the incident wave conditions correspond to a plunging type breaker. PIV-based measurements were carried out for about seven minutes and covered 0.57 meters around the breaking point where a bar was formed and moved onshore-ward. To synchronize image data in all these cameras, a high intensity flash was popped up at the end of recordings that was readily detected in each FOV.

DATA ANALYSIS

Calibration and Validation of PIV

Since accurate velocity estimation skills using PIV essentially rely on the determinations of window sizes, within which best-fit pixel patterns are searched based on correlations of two successive images, the optimum window size was first calibrated through the comparisons with measured velocities by ADV. Since the installation of ADV probe affected the images for PIV, we performed separate experiments respectively for measurements by PIV and ADV after the beach profiles reached to the equilibrium state. In these calibration experiments, both ADV and PIV recorded 20 waves exactly at the same location.

A PIV algorithm, based on enhanced Minimum Quadratic Different (MQD) method (Ahmed & Sato, 2001), was applied for various combinations of interrogation and searching window sizes. The best match conditions (interrogation window size of 69x69 pixels and searching window size of 49x49 pixels) were adopted and comparison of results after removal of high frequency noise based on Fast Fourier Transform (fft) are shown in figure 2. Figure 2 compares both horizontal and vertical velocity components measured and estimated by ADV and PIV, respectively.

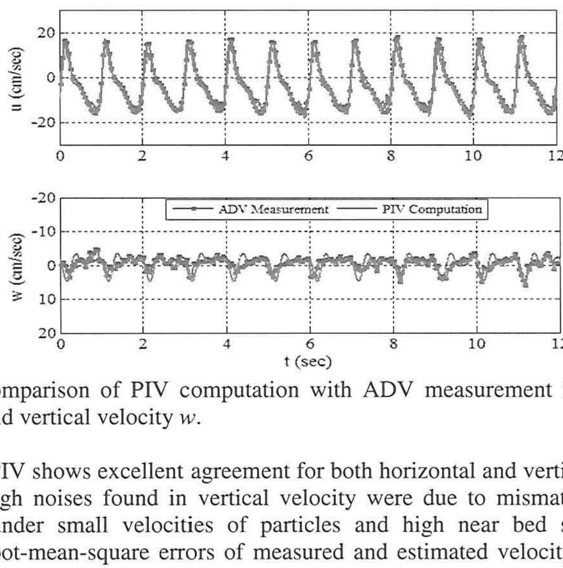

Figure 2: Comparison of PIV computation with ADV measurement for horizontal velocity *u*, and vertical velocity *w*.

The PIV shows excellent agreement for both horizontal and vertical velocities. Relatively high noises found in vertical velocity were due to mismatching of PIV correlation under small velocities of particles and high near bed suspension of sediment. Root-mean-square errors of measured and estimated velocity components in horizontal and vertical directions are 2.6 and 3.2 cm/sec respectively.

Boundary Detection Technique

This study also developed a Boundary Detection Technique (BDT), which captured the temporal and spatial high resolution data of surface water elevations and bottom bed profiles over the entire surf zone. In BDT, RGB information of each image is utilized to obtain threshold values at water-air and water-sand boundaries, respectively. The logic behind the detection of the boundary is to identify the position of pixel where the representative value (say C) equals the threshold value (C_{th}). The following figure 3(a) shows typical image recorded by HSVC, while 3(b) shows the detected boundaries of surface water and bed bottom in solid lines and the instantaneous velocity fields obtained by PIV in vectors.

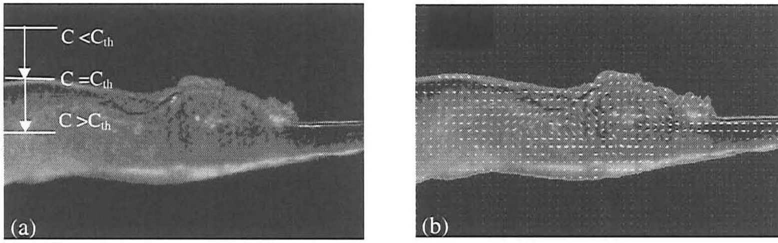

Figure 3: (a).Typical image recorded by HSVC. (b). Water-air and water-sand boundaries detected by BDT (in solid lines) and instantaneous velocity vectors estimated by PIV algorithm.

For validation of BDT, temporal data of surface water elevations from four wave gauges (WG2, WG3, WG4, and WG5) mounted at various positions are compared with BDT results (see figure 4).

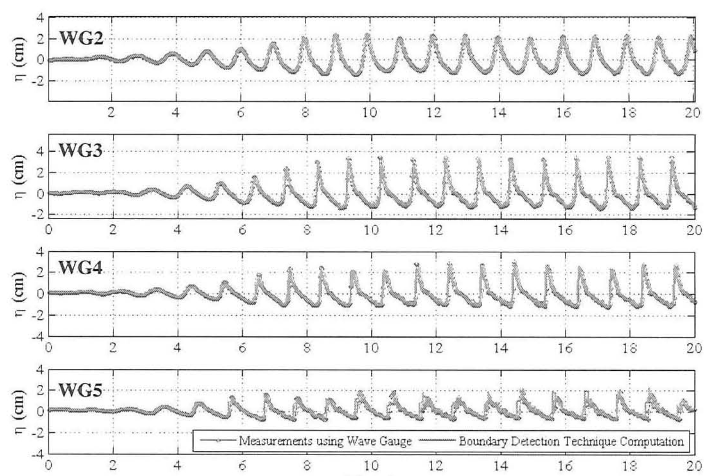

Figure 4: Comparison of water surface elevation, η extracted from images using BDT and those recorded by wave gauges at four different locations around the surf zone.

The comparison shows robustness of BDT for measurements of the surface water elevations compared with the one recorded by each wave gauges. Since BDT is sensitive to the local brightness of pixel, therefore air bubbles that develop at the water surface as a result of wave breaking may cause some fluctuations as observed in the comparison of WG5 data. Later, a similar procedure is readily adopted for detection of water-sand boundary and to extracted high resolution bottom bed profiles in temporal and spatial domains.

DYNAMIC CHANGES OF MEASURED BED PROFILES AND VELOCITIES

Developed image-capturing techniques were applied for the experimental case respectively at 1, 2, 3, 4, 5 and 6 minutes after the initiation of waves. During the first five minutes, bottom bed profiles and waves were dynamically changed and nearly reached to the equilibrium conditions. At each time (every minute), images of ten waves were used for estimations of detailed velocity components.

Dynamic Changes of Bottom Bed Profiles

To obtain the bottom bed profile, BDT was applied to the images captured by all the cameras. Based on the known spatial locations at bench marks inside FOVs, obtained boundaries in each image were combined to yield single lines of the bed profiles across the entire surf zone at every time. Figure 5 shows morphology change at 1, 2, 3, 4, 5 and 6 minutes after the initiation of the wave generation.

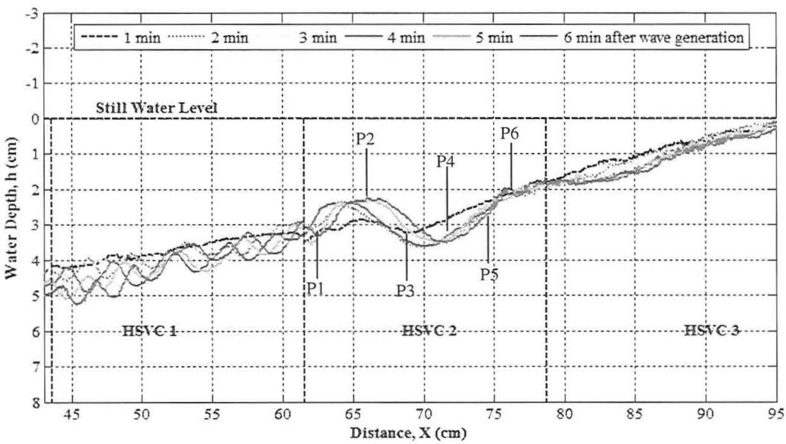

Figure 5: Spatial and temporal variation of bottom bed profile extracted using BDT from the image data recorded with three HSVCs.

As seen in figure 5, BDT successfully captured the bar formation and its onshore migration. It is interesting to observe that the bar was formed quickly within the first two minutes while the onshore movement of the bar was relatively slow but continued until six minutes after the initiation of the wave generation (see region recorded by HSVC 2). Meanwhile, ripples generated outside of the surf zone, seen in HSVC1, show continuous onshore migrations. Further, in the area observed in HSVC3, rapid erosion in near-shore region was observed during the first four minutes. After four minutes, bed profile in the area of HSVC 3 was stabilized while the bar in HSVC 2 still showed onshore migrations.

Characteristics of Current Velocities and Suspended Sediments over the Bar

In order to investigate the characteristics of the current and suspended sediment concentrations on the changing movable beds around the bar, six points, we applied PIV at P1, P2, P3, P4, P5 and P6, shown in figure 5, at times, 1 min, when the bar was being developed, 4min, when the bar was fully developed, and 5 & 6 min when the bar was moving shore-ward. The elevation of the observation point was kept constant at 30 pixels (1 cm) above the movable bed whose elevation changes at different time. At each point, horizontal current velocities, u and image brightness, C, which represents the suspended sediment concentrations, were extracted. According to Liu (2005), image brightness and the suspended sediment concentrations have nearly linear relationships under the uniform lighting conditions without the use of additional seeding particles except bottom sand grains for PIV. Figure 6 shows the averaged time profiles of u and C at different time and locations.

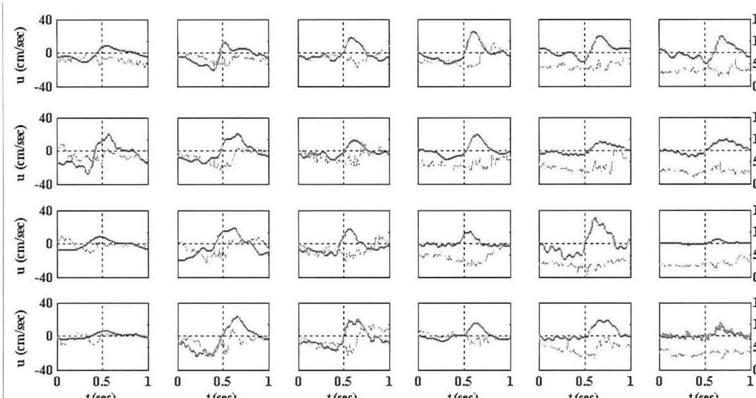

Figure 6: Averaged time profile of horizontal current velocity u (bold lines) and corresponding image brightness, C (dash lines) at P1, P2, P3, P4, P5 and P6 (placed horizontally from left to right) after 1, 4, 5 and 6 minutes (placed vertically from top to bottom).

When the absolute values of the horizontal velocity components are relatively small especially seen during the offshore flow, the present PIV appears to yield unreliable velocity estimations due to pixel resolutions of the present setups. However, the points across the sand bar i.e., from P1 to P3, yielded somewhat reliable velocity profiles. Figure 7 shows the estimated mean current velocity and mean suspended sediment concentrations at P1, P2 and P3.

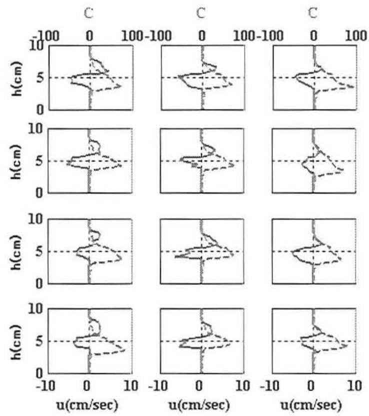

Figure 7: Time averaged undertow velocities (solid line) and suspended sediment concentration (dash line) in terms of brightness at P1, P2 and P3 (placed horizontally from left to right) after 1, 4, 5 and 6 minutes (placed vertically from top to bottom).

Suspended Sediment transport over the Bar

Net suspended sediment transport rate is quantified by time-averaging the depth-integrated product of u and C, i.e.,

$$q_s = \overline{\int_0^{h_t} uCdz} \tag{1}$$

with z, upward elevation from the bottom. Note that integration range was limited up to the wave trough level, h_t, under the assumption that there is nearly no suspended sediments above the trough level. The net q_s may then be decomposed into two parts,

$$\overline{\int_0^{h_t} uCdz} = \int_0^{h_t} \overline{u}\overline{C}dz + \int_0^{h_t} \overline{\tilde{u}\tilde{C}}dz = q_{s1} + q_{s2} \tag{2}$$

with $\overline{u}$ & $\overline{C}$, the time-averaged components of u and C, and $\tilde{u}$ & $\tilde{C}$, time-fluctuations of u and C around their time-averaged components, i.e., $u = \overline{u} + \tilde{u}$ and $C = \overline{C} + \tilde{C}$.

Figure 8 shows the estimated components of suspended sediment transport rates, q_s, q_{s1} and q_{s2} at different locations and times. The figure 8 also shows the changing local bottom slopes estimated from the extracted bed profiles. Here the bottom slope is expressed in positive value when the water depth is increasing in the shoreward and the horizontal distance used for estimation of the bottom slope was represented by the excursion amplitude of the bottom orbital velocity.

As seen in the figure 8, q_{s1}, i.e., the depth-integrated product of $\overline{u}$ & $\overline{C}$, dominate q_{s2}, the time-averaged product of $\tilde{u}$ & $\tilde{C}$ under all conditions. The net sediment transport, q_s, at all three points are shoreward and the magnitude of q_s at P2 was greater than the others, P1 and P3 from t=1 min to 2 min. As a result of this unbalance, bottom bed was eroded between P2 and P3 and accumulated between P1 and P2. After t=3min, in contrast, net transport at all three locations seems approximately uniform suggesting a temporary equilibrium similar to that observed during morphology changes of bottom bed at corresponding time. At t=4 min, furthermore, the higher offshore ward transport at P3 relative to P2 caused initiation of shoreward sand bar movement.

The depth-integrated product of mean components, q_{s1}, shows strong correlation with the location relative to the bar crest. At P2, for instance, the seaward q_{s1} dramatically increases as the sand bar moves shoreward and the relative location of P2 approached to the bar crest. While q_{s1} shows clear correlation with the relative location to the sand bar, q_{s2}, the component of fluctuating suspended sediment transport rates appear to show correlation with the local bottom slope especially during the first four minutes. Until four minutes, increase or decrease of qs2 surely correspond to the increase or decrease of the bottom slope. It is however interesting to point out that this correlation breaks after five minutes when the movement of the sand bar became predominant.

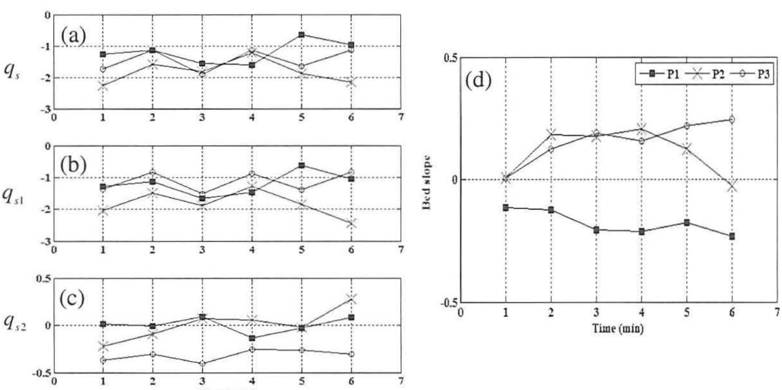

Figure 8: Temporal Variation of $\overline{uC}$ (fig.9a), $\overline{u}.\overline{C}$ (fig. 9b) and $\overline{u'C'}$ (fig9c) at P1 and P2 and P3. Fig.9d shows the corresponding local bed slope computed across horizontal excursion amplitude of water particle. (Note: A positive value of slope represents downwards slope and vice versa.)

CONCLUSION

This study developed a new set of image-capturing techniques that successfully obtained the high-resolution quantitative data sets of waves, currents and bottom bed profiles both in the time and space domains. Boundary Detection Technique successfully captured the phenomenon of bar formation and its onshore migration along with ripple migrations.

Change of the time-profiles of current velocity as well as suspended sediment concentrations were estimated and, based on these profiles, the time-averaged components of net suspended sediment transport rates were computed and compared. The total net suspended sediment transport rates reasonably explained the morphology change around the sand bar. The net suspended sediment transport rates were decomposed into two parts, mean-component, q_{s1}, and the fluctuation components, q_{s2}. The mean components dominantly determined the total net suspended sediment transport rates and their magnitudes show clear correlations with the relative locations to the sand bar crest. While the magnitude was relatively small, the fluctuating component showed clear correlations with the local bottom slopes especially before the shoreward movement of the developed sand bar. Further improvements of the image-capturing system and investigations of obtained high-resolution data sets of current, suspended sediments and corresponding bottom topography should be achieved in the future research.

ACKNOWLEDGMENT

This work was gratefully supported by Grant-in-Aid for Young Scientists (B), No. 20760322, from Japan Society for the Promotion of Science (JSPS).

REFERENCES

Ahmed, A. S. M., and Sato S. (2001). "Investigation of bottom boundary layer dynamics of movable bed by using enhanced PIV technique" *Coastal Engineering Journal*, Vol. 43, No. 4, pp. 239-258.

Cox, D.T., and Kobayashi, N., (2000). "Identification of intense, intermittent coherent motions under shoaling and breaking waves". *J. Geophysical Research. 105 (6)*, 223–236.

Cowen, E. A., Sou, I. M., Liu, L. F, and Raubenheimer, B. (2003). "Particle image velocimetry measurements within a laboratory-generated swash zone". *Journal of Engineering Mechanics* 1119-1129.

Elgar, S., Rauhenheimer, and B., Guza, R.T. (2005). "Quality control of acoustic doppler velocimeter data in the surf zone". *Meas. Sci. Technol. 16*, 1889-1893.

Govender, K., Mocke, G.P., and Alport, M.J. (2002). "Video-imaged surf zone wave and roller structures and flow fields" *J. of Geophysical Research*, Vol. 107, No. C7, 3072.

Govender, K., Mocke, G.P., and Alport, M.J. (2004). "Dissipation of isotropic turbulence and length scale measurements through the wave roller in the laboratory spilling waves" *J. of Geophysical Research*, Vol. 109 C08018.

Govender, K., Michallet, H., Alport, M.J., Pillay, U., Mocke, G.P., and Mory, M. (2009). "Video DCIV measurements of mass and momentum fluxes and kinetic energies in laboratory waves breaking over a bar". *Coastal Engineering (56)* 876-885.

Liu, H., (2005). "Laboratory experiments and numerical simulation on sheetflow sediment movement" *PhD Thesis*, Dept. of Civil Engineering, The University of Tokyo.

Longo, S., (2009). "Vorticity and intermittency within the pre-breaking region of spilling breakers." *Coastal. Engineering. 56 (3)*, 285–296.

Nadaoka, K., Hino, M., and Koyano, Y., (1989). "Structure of the turbulent flow field under breaking waves in the surf zone". *J. Fluid Mech. 204*, 359–387.

Kimmoun O., and Branger, H. (2007). "A particle image velocimetry investigation on laboratory surf-zone breaking waves over a sloping beach" *J. Fluid Mechanics.*, vol.588, 353-397.

Shin, S. and Cox. D.T., (2006). " Laboratory observations of inner surf and swash-zone hydrodynamics on a steep slope. *Continental Shelf Research 26*. 561-573.

Stive, M.J.F. (1984). "Energy dissipation in wave breaking on gentle slopes" *Coastal Engineering 8*, 99-127.

Ting, F.C.K., and Kirby, J.T., (1996). "Dynamics of surf-zone turbulence in a spilling breaker". *Coastal. Engineering. 27*, 131–160.

Huang, Z. C., Hsiao S. C., Hwung H. H., and Chang, K. A. (2009). "Turbulence and energy dissipation of surf-zoen spilling breakers", *Coastal Engineering (56)* 733-746.

Local Scour and Development of Sand Wave around T-type and L-type Groynes

A. Kadota[1] and K. Suzuki[1]

[1]Hydralic Engineering Laboratory, Department of Civil & Environmental Engineering, Faculty of Engineering, Ehime University, 3 Bunkyo-cho, Matsuyama, Ehime 790-8577, Japan; PH +81-89-927-8579; FAX +81-89-927-9831; email: akado@dpc.ehime-u.ac.jp

ABSTRACT

There are several types of groyne such as T-type and L-type groynes. These groynes have been empirically constructed worldwide according to several environments. Because the sand transported from the groynes largely affects on the formation of sand wave, the morphological phenomena should be considered systematically and in detail. In this study, the characteristics on changes of bed configuration due to T and L-type groynes are experimentally revealed comparing with the experimental results of I-type groynes.

Experiments were conducted in a straight flume with a sand box to make a movable bed. To cover a large measurement area at the downstream of groyne, a long-range laser displacement sensor was used. The bed configurations are accurately measured by the measuring system. Experimental results show that the maximum scour depth changes greatly with the groyne types. The difference of bed form downstream of the groyne is seen in development and sand waves.

INTRODUCTION

Groynes have been used for the stabilization of banks, creating a navigation channel by confining the cross-sectional area and improving habitat of flora and fauna, especially for large rivers worldwide. The most important phenomena are local flow and local scour around the groyne tip. Therefore, sediment transport and its related erosion (or scour) phenomena around the groynes have been studied experimentally and numerically in rivers and coastal regions (The earlier studies by Garde et al. 1961, Gill 1972, Kuhnle et al. 2002). The former studies focused mainly on local scour phenomena around strait (I-type) groynes. There are several types of groyne such as T-type and L-type groynes which have been empirically constructed worldwide according to several environments in rivers. However, a little information is obtained on changes of bed configuration as well as local scour around the different shaped groynes. Because the sand transported from the groynes largely affects on the formation of sand wave far downstream area, these phenomena should be also considered systematically and in detail.

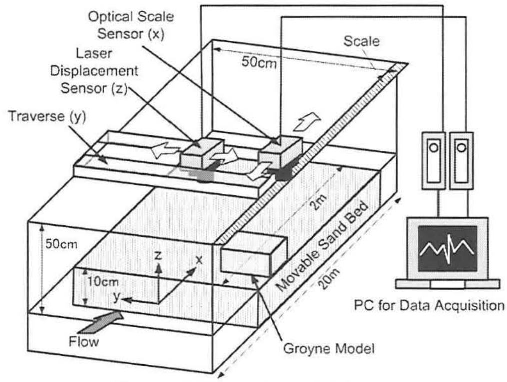

Figure 1 Experimental Setup

In this study, the characteristics on changes of bed configuration around the T or L-type groynes are experimentally revealed comparing with the experimental results of I-type groynes. Experiments were conducted in a straight flume with a sand box at middle of the flume to make a movable bed. To cover a large measurement area at the downstream of groyne, a long-range laser displacement sensor was used to measure the bed configuration and an optical scale sensor was used to measure the position of laser displacement sensor. The bed levels of downstream area are immediately and accurately measured by the measuring system.

Experimental results show that the maximum scour depth changes greatly with the groyne types and the scour depth for the L-type groyne becomes much smaller than that of I-type groyne. The difference of bed form downstream of the groyne is seen in development and length of sand waves is discussed below.

EXPERIMENTAL SETUP

Experiments were conducted in a 20m long, 50cm wide and 50cm deep straight flume as shown in Figure 1. In this flume, water discharge and flow depth are controlled by a V-notch weir and a movable gate at the end of flume, respectively. A sand box with a 2m long and 10cm height is installed at middle of the flume and small sand (mean diameter d_m=0.3mm) is filled up in the box to make a movable bed. A scale groyne models were installed on the sand bed. The sizes and shapes of scale model are indicated in Figure 2 and Table 1. All models were made from vinyl-chloride plate with 2cm thickness. There are two L-type groyne models. One is heading upstream (LU), and the other is heading downstream (LD). Stream-wise lengths (L_f) are 10cm for I-type and T-type groyne models, 6cm and 10cm for L-type groyne models. Span-wise lengths (L_g) are 10cm for all cases.

To cover a large measurement area at the downstream of groyne, a long-range laser displacement sensor (KEYENCE LB-300) was used to measure the bed configuration and an optical scale sensor (KEYENCE VP-90) was used to measure

Table 1. Experimental Conditions

Case	I	T	LU6	LU10	LD6	LD10
Type of Groyne Shape	I-type	T-type	LU-type	LU-type	LD-type	LD-type
Stream-wise Length of groyne model L_f (cm)	-	10	6	10	6	10
Bulk Mean Velocity v_o (cm/sec)	21.0					
Flow Depth (cm)	10.0					
Flow Condition	Emerged					

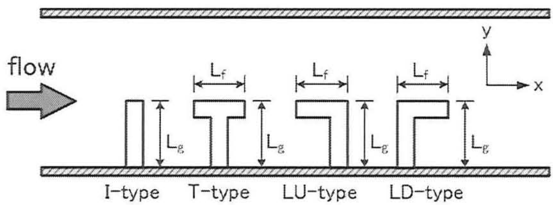

Figure 2 Shapes of Groyne Model

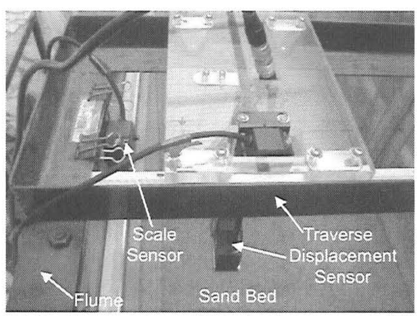

Figure 3. Displacement and Scale Sensors with Traverse

the position (x, y) of laser displacement sensor as shown in Figure 3. The bed levels of downstream area are immediately and accurately measured by means of this measuring system.

The hydraulic conditions are shown in Table 1. All experimental cases are under non-submerged condition and the water depth (h) is 10cm. As seen in Table 1, each case is called such as T-type (T), L-type heading upstream with 10cm length (LU10), L-type heading downstream with 6cm length (LD6) and so on. A constant bulk mean (inflow) velocity is applied as v=21cm/sec for all experimental cases. These experiments are conducted under clear water scour condition without any sand supply from inlet at upstream end. The experiments start from flat bed condition and bed configuration was measured after 60min because the scour depth around the tip of I-type groyne becomes stable condition after 60min as shown in Figure 4.

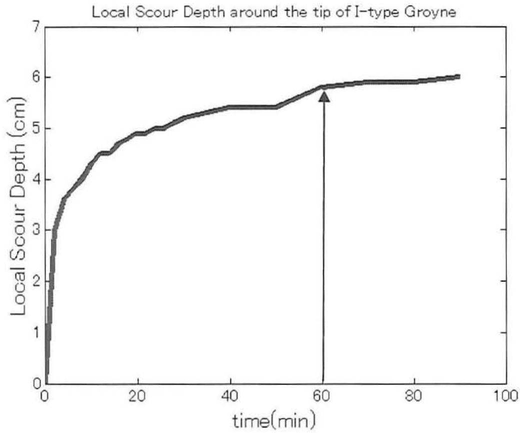

Figure 4. Time variation of local scour depth around the tip of I-type groyne

RESULTS AND DISCUSSION

Local scour process around groyne tip. Local scouring obviously occurs at the upstream of groyne tip due to vertically-downstream flow. Figure 5 shows the bed configurations after 60min around the all types of groyne. In addition, Figure 6 shows the relationship between maximum scour depth and groyne shape.

Comparing with scour depths of all cases, the maximum scour depth is the smallest around L-type groyne heading upstream with 10cm stream-wise length (case LU10). On the other hand, the maximum scour depths for the other cases become larger than that of I-type groyne. It can be considered that the maximum depth becomes smaller in proportion to area of dead zone at upstream side of groyne. These phenomena seem to be related with vertically-downstream flow at upstream side of groyne which is smaller than that of I-type groyne. In other words, it means the shear stresses between the two zones become smaller in LU10 case._As a result, amount of suspended sediment from the dead zones decreases.

On the other hand, the scour depths of cases (T, LD6 and LD10) are showing the almost same level whereas the scour depth around L-type groyne is smaller in longer case (LU10) as seen in Figure 6. It can be seen from Figure 5 that area of scour hole is related with scour depth and expand forming concentric circle.

Morphological changes downstream side of groyne. In the downstream area behind groynes, suspended sediment is transport from scouring hole and then local deposition area is formed. Afterward, local scouring is formed behind the local

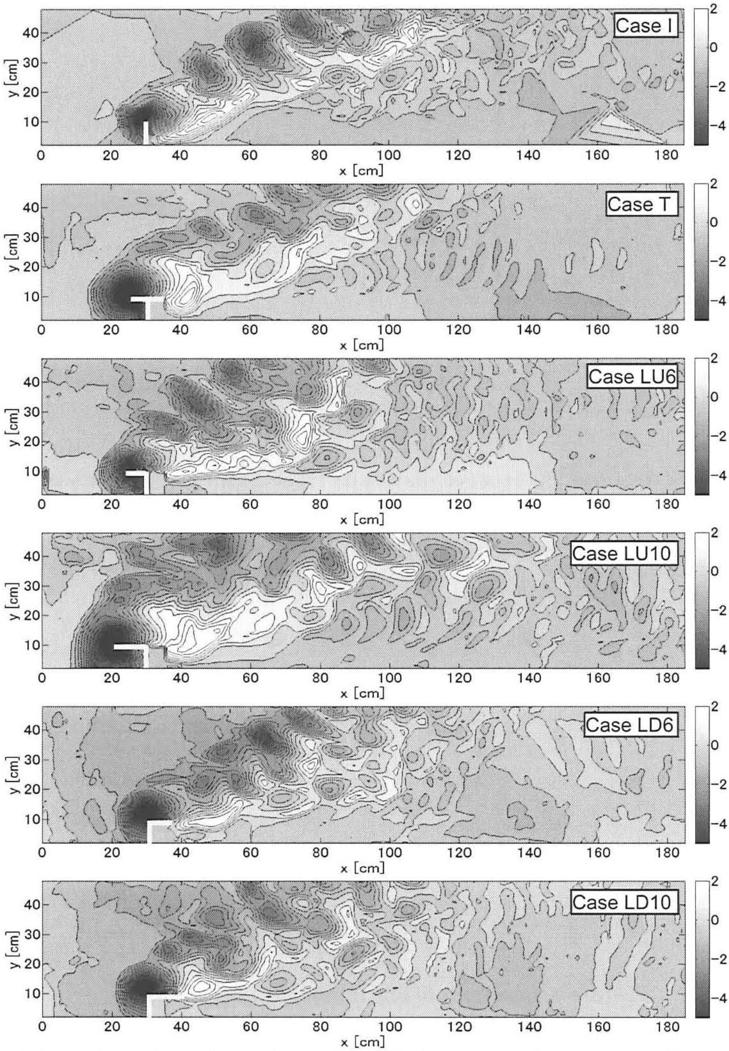

Figure 5. Bed configurations after 60min around the all types of groyne

deposition area successively then a sand wave is formed. Figure 7 shows the locations of maximum local deposition estimated from each sand waves as seen in Figure 5.

Comparing with T and L groyne-type cases (T, LU6, LU10, LD6 and LD10), the maximum local deposition of case LD6 is located with some distance downstream from the groyne whereas it located near the groyne tip for the other cases. In addition,

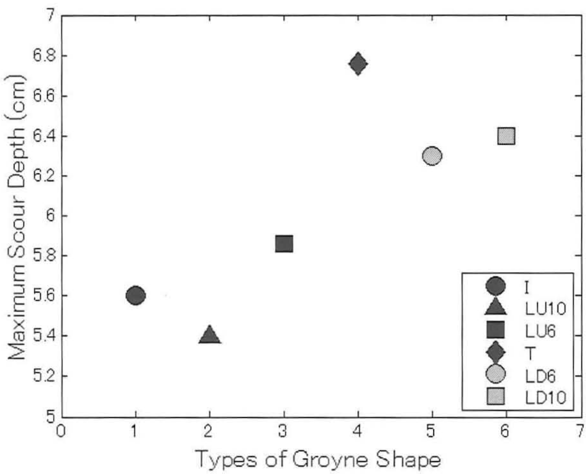

Figure 6. Relationship between maximum scour depth and groyne shape

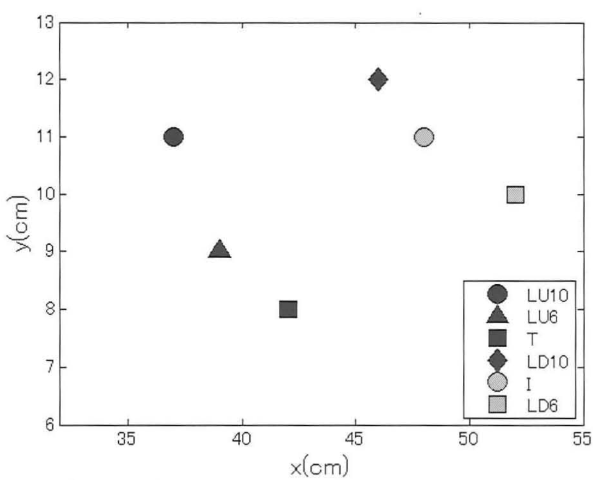

Figure 7. Locations of maximum local deposition

the bed configuration in this case is similar to that of I-type groyne. As for the case LD10, the maximum deposition occurs at the downstream end of the groyne and distributed with belt-shaped deposition. In the cases of T, LU6 and LU10, significant deposition is seen in cross-wise direction and is distributed surrounding scour hole.

Figure 8 shows average wave length (L_e) and average wave height (H_e) for all cases. According to results from Ashida & Michiue (1972) for criterion of sand wave configuration, the wave length and height of present cases are estimated as $10.62 < L_e < 14.70$, $1.51 < H_e < 2.79$. As the result, the bed configurations of Figure 5 belong to

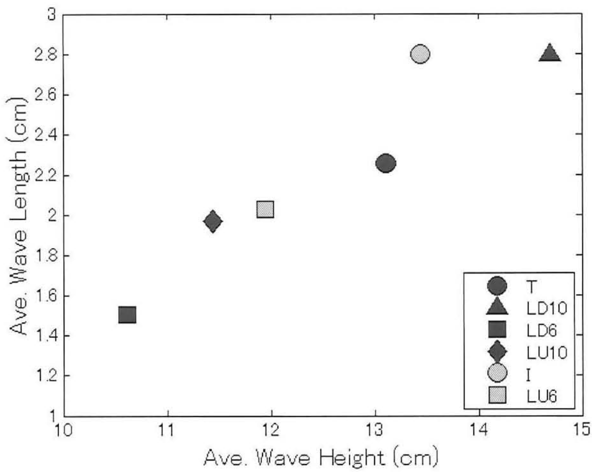

Figure 8. Average wave length (L_e) and average wave height (H_e)

lower flow regime and are ripples or dunes. Figure 9 shows the direction of development of sand wave. The sand wave of case T, LU6 and LU10 develop to the opposite wall side whereas the sand wave of case I and LD6 develop to the same direction.

As the result, the location of local deposition is affected by the location of local scour. In case that the local scour occurs at upstream-side of groyne, the deposition forms surrounding the scouring area. On the other hand, in case that local scour occurs at downstream side of groyne, the deposition forms with some distance from the groyne. As seen in Figures 6 and 8, wave length and wave height become smaller as the maximum scour depth is larger, and the opposite property is also seen. It is considered that such tendency is related with location of local deposition. Because the deposition located at downstream in case I, LD6 and LD10, suspended sediment is floating for a long time and deposits on far area from groyne then the wave length and wave height become larger. Also, the direction of sand-wave development shows similar relation. In case that deposition area located at upstream side such as case T, LU6 and LU10, sand-wave develops to direction to the opposite wall side comparing with case I.

CONCLUSION

In the present study, the characteristics of local scour and bed configuration downstream of several types of groyne are experimentally discussed. As a result, the scour depth becomes large for L-type groyne heading downstream and local deposition occurs with some distance from the groyne. In case of L-type groyne heading upstream, the local scour becomes smaller. However, wave length and wave height becomes larger and sand wave develops to opposite wall side.

REFERENCES

Garde, R.J., Subramanya, K. and Namburdripad, K.D. (1961): Study of scour around spur dikes, "*Journal of Hydraulic Division*", ASCE 87(HY6), 23-37.

Gill, M.A. (1972): Erosion of sand beds around spur-dikes, "*Journal of Hydraulic Division*", ASCE 98(HY9), 1587-1602.

Kuhnle, R.A., Alonso, C.V., Shields, F.D. (2002): Local scour associated with angled spur dikes, "*Journal of Hydraulic. Engineering*", ASCE 128(12), 1087-1093.